

Ingvild Vallestad

Type AISI 316 Stainless Steel in Chloride Containing Environment – Effect of Mo Content on the Corrosion Properties and a Pit Propagation Study

Master's thesis in Materials Science and Engineering

Supervisor: Roy Johnsen, MTP

June 2019

Ingvild Vallestad

Type AISI 316 Stainless Steel in Chloride Containing Environment – Effect of Mo Content on the Corrosion Properties and a Pit Propagation Study

Master's thesis in Materials Science and Engineering
Supervisor: Roy Johnsen, MTP
June 2019

Norwegian University of Science and Technology
Faculty of Engineering
Department of Mechanical and Industrial Engineering



Norwegian University of
Science and Technology

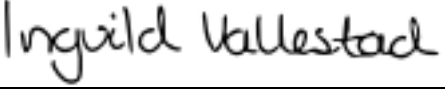
Preface

This master thesis was written at the Norwegian University of Science and Technology (NTNU), Faculty of Engineering, Department of Mechanical and Industrial Engineering, in the spring 2019. The project has been a collaboration between NTNU and Aker BP ASA, with Professor Roy Johnsen as the main supervisor.

I would like to thank my supervisor Professor Roy Johnsen for excellent guidance, encouragement and support during my master thesis. His helpfulness and availability have been highly appreciated. I would also like to thank Cristian Torres for assistance and technical help with my experimental work whenever needed. Finally, I would like to thank my co-supervisor Stian Strømstad for his enthusiasm during my master thesis.

I hereby declare that this work has been performed independently and in accordance with rules and regulations at NTNU.

Trondheim, June 11, 2019



Ingvild Vallestad

Abstract

This report focuses on corrosion challenges with using the austenitic stainless steel AISI 316L (UNS S31603) in marine atmosphere. AISI 316L has been frequently used in marine atmosphere for several decades due to the corrosion resistance, however over the recent years pitting and crevice corrosion attacks has been observed. The aim of this study is to investigate the effect of small changes (0.5 wt%) in molybdenum content on the corrosion properties, and to study pit propagation with focus on repassivation and the effect of cathode area. The effect of chloride concentration and temperature are included when evaluating the effect of molybdenum content.

In this study, the effect of molybdenum content was investigated by conducting experiments with AISI 316L and alloys with similar composition. Anodic cyclic potentiodynamic polarisation curves were recorded with 3 and 5 wt% sodium chloride solution at both room temperature and $35 \pm 2^\circ\text{C}$. Open circuit potential measurements and exposure in a salt spray chamber were conducted by using 5 wt% sodium chloride at $35 \pm 2^\circ\text{C}$. To study propagation of a single pit a method to obtain the potential at the pit opening and the galvanic current from a single pit were developed and conducted with different set ups regarding the cathode area.

The result from the anodic cyclic potentiodynamic polarisation implied that differences in alloying content affects the pitting potential where the temperature has a slightly greater effect than chloride concentration, while the repassivation potential is not significantly affected. Considering the obtained results from the experiments, 3 wt% molybdenum increases the corrosion resistance. For alloys containing below 2.5 wt% molybdenum small changes do not significantly affect the corrosion resistance if the nitrogen content increases sufficient. Increased nitrogen content appeared to retain the corrosion properties as the molybdenum content decreases.

The result from the artificial pit experiments indicated that the pits propagated continuously and did not repassivate in 6wt% FeCl_3 when connected to an external cathode area. Both the cathode area and electrolyte composition were established to considerably affect propagation of a single pit. The pit size increases with cathode area in 6 wt% FeCl_3 , and the cathode efficiency decreases significantly in 5 wt% NaCl compared to 6 wt% FeCl_3 .

Sammendrag

Denne rapporten fokuserer på korrosjonsutfordringer med det austenittiske rustfrie stålet AISI 316L (UNS S31603) i marin atmosfære. AISI 316L har vært et utbredt materialvalg i marin atmosfære i flere tiår på grunn av korrosjonsmotstanden, men over de siste årene har spalt- og gropkorrosjon vært en utfordring. Hensikten med denne oppgaven er å undersøke om små endringer (0.5 vekt%) i molybdeninnhold påvirker korrosjonsegenskapene, samt studere hvordan en grop vokser med fokus på repassivering og effekten av katodeareal. Effekten av temperatur og kloridkonsentrasjon er inkludert i vurderingen av effekt av molybdeninnhold.

I denne studien har det blitt utført eksperimenter med AISI 316L og lignende legeringer med ulikt molybdeninnhold for å undersøke effekten av molybden. Syklisk anodisk potentiodynamisk polarisasjonskurver ble tatt opp ved rom temperatur og $35 \pm 2^\circ\text{C}$ i både 3 og 5 vekt% natriumklorid. Målinger av åpen krets potensiale og eksponering i salttåkekammer med 5 vekt% natriumklorid ved $35 \pm 2^\circ\text{C}$ ble også utført. For å studere utviklingen av en grop ble det utviklet en metode for å måle galvanisk strøm og potensialet ved grop åpningen ved ulik størrelse på katodearealet.

Resultatene fra de sykliske anodiske potentiodynamiske polarisasjonskurvene viser at ulikheter i legeringsinnhold påvirker potensialet for initiering av gropkorrosjon, mens potensialet for repassivering blir ikke påvirket i stor grad. Temperatur viste seg å ha en større effekt på potensialet for initiering av gropkorrosjon enn kloridkonsentrasjon. Resultatene fra de utførte eksperimenter i denne studien tyder på økt korrosjonsmotstand ved 3 vekt% molybden. For legeringer med under 2.5 vekt% virker små endringer å ikke påvirke korrosjonsmotstanden i stor grad siden nitrogeninnholdet endres. Ved redusert molybdeninnhold tyder resultatene på at korrosjonsegenskapene blir bevart dersom nitrogeninnholdet øker.

Resultatet fra studien angående utviklingen av en grop viste at gropen vokste kontinuerlig og repassiverte ikke i 6 vekt% FeCl_3 når den var koblet til en ekstern katode. Både katodearealet og sammensetningen på elektrolytten viste seg å betydelig påvirke vekst av en grop. Størrelsen på gropen øker med katodeareal i 6 vekt% FeCl_3 , og den katodiske effektiviteten reduseres signifikant i 5 vekt% NaCl sammenlignet med 6 vekt% FeCl_3 .

Table of contents

Preface	i
Abstract	iii
Sammendrag	v
Table of contents	vii
List of figures	xi
List of tables	xvii
Abbreviations	xix
Nomenclature	xxi
1 Introduction	1
1.1 Background and motivation	1
1.2 Objective	2
1.3 Limitations	2
1.4 Approach	2
2 Theoretical background	3
2.1 Austenitic stainless steels	3
2.2 Passive films	4
2.3 Corrosion mechanisms	5
2.3.1 Crevice corrosion	6
2.3.2 Pitting corrosion	8
2.3.3 Galvanic corrosion	10
2.4 Pit propagation	10
2.4.1 Pit stability	11
2.4.2 Cathode limitations	13
2.4.3 Pit size calculation	14
2.5 Factors affecting pitting and crevice corrosion	14
2.5.1 Temperature	14
2.5.2 Chloride concentration	15
2.6 Cyclic potentiodynamic polarisation curves	16
2.6.1 Determining features from the curves	17
2.7 Ranking of pitting corrosion susceptibility for different alloys	19
3 State of the art	21
3.1 The role of molybdenum	21
3.2 Effect of molybdenum content	22
3.2.1 Synergy between molybdenum and nitrogen	25
3.3 Pit propagation	28
4 Experimental work	31
4.1 Test materials and preparation	32

4.2	Anodic cyclic potentiodynamic polarisation	34
4.2.1	Experimental procedure	35
4.3	Open circuit potential measurements	36
4.3.1	Experimental procedure	37
4.4	Salt spray test	38
4.4.1	Sample preparation	39
4.4.2	Experimental procedure	40
4.5	Artificial pit experiments	42
4.5.1	Sample preparation	44
4.5.2	Experimental procedure	45
4.5.3	Cathodic potentiodynamic polarisation	47
4.6	Surface characterisation	48
5	Results	51
5.1	Anodic cyclic potentiodynamic polarisation	51
5.1.1	Surface characterisation	55
5.2	Open circuit potential measurements	57
5.2.1	Surface characterisation	59
5.3	Salt spray test	64
5.3.1	Anodic cyclic potentiodynamic polarisation curves of coated samples	68
5.4	Artificial pit experiments	69
5.4.1	Potential and galvanic current measurements	70
5.4.2	Anodic cyclic and cathodic potentiodynamic polarisation curves	76
5.4.3	Surface characterisation	76
6	Discussion	81
6.1	Anodic cyclic potentiodynamic polarisation	81
6.1.1	Surface characterisation	85
6.2	Open circuit measurements	87
6.2.1	Surface characterisation	89
6.3	Salt spray test	91
6.4	The effect of molybdenum content – general discussion	93
6.5	Artificial pit experiments	95
6.5.1	Anodic cyclic and cathodic potentiodynamic polarisation curves	98
6.5.2	Surface characterisation	99
6.5.3	Pit propagation – general discussion	101
7	Conclusion	105
8	Further work	106
	Reference list	107
	Appendix A	112
	Appendix B	114
	Material certificate UNS S31600/S31603	114
	Material certificate UNS S31700/S31703	118

Material certificate UNS S31655	121
Chemical composition UNS S31603	122
Material certificate UNS S31254	123

List of figures

Fig. 2.1: The passive film thickness for AISI 316L and 304 formed under wet dry cyclic conditions at 60°C with 0.1M NaCl[14].	5
Fig. 2.2: Different cross-sectional pit shapes[17].	5
Fig. 2.3: The chemistry that develops within an active crevice during crevice corrosion[21].	6
Fig. 2.4: Schematic illustration of the pitting corrosion mechanism under a thin electrolyte layer where the pit initiates at an MnS inclusion[30].	8
Fig. 2.5: The difference in mass transport between a) immersed conditions and b) atmospheric conditions[33]. The quality is poor due to the original source.	9
Fig. 2.6: Illustration of the galvanic coupling during atmospheric pitting corrosion[40].	11
Fig. 2.7: Illustration of the pit stability product principle[48].	12
Fig. 2.8: The effect on E_{pit} of a) increased chloride concentration at different pH and b) increased temperature at different chloride concentrations[56].	15
Fig. 2.9: Illustration of a typical cyclic potentiodynamic polarisation curve for a material exhibiting protection potential[58].	16
Fig. 2.10: Determining E_P (E_{pit}) from cyclic potentiodynamic polarisation curves[65].	18
Fig. 2.11: Determining E_{RP} (E_{rep}) from cyclic potentiodynamic polarisation curves[65].	18
Fig. 3.1: E_{pit} obtained in 0.1-1.0 M de-aerated NaCl for AISI 316 and 302 with different chloride concentrations at room temperature[36].	23
Fig. 3.2: Anodic potentiodynamic polarisation curves for AISI 304LN, 316LN and 317LN in 0.01M FeCl ₃ at 25°C with a scan rate of 10 mV/min[70].	24
Fig. 3.3: Anodic potentiodynamic polarisation curves of a) AISI 316 with different N content and b) AISI 316 and 304. The curves are obtained at room temperature in a de-aerated 0.5 M NaCl and 0.5 M H ₂ SO ₄ solution [76].	26
Fig. 3.4: E_{pit} obtained from potentiodynamic polarisation curves in 3.5 wt% NaCl at 25°C with 1 mV/s scan rate for austenitic stainless steels with different Mo and N content as a function of pH[6].	27
Fig. 3.5: a) Recorded current and b) mean pit depth and radius for AISI 316L as a function of time. The experiments were conducted at $0V_{MSE}$ in 0.5M H ₂ SO ₄ with locally supply of chloride ions at the pit by using 3M NaCl and 0.5M H ₂ SO ₄ [78].	28
Fig. 3.6: Pit depth and radius of single pits on 316L obtained at different potentials in the passive domain with a 0.5M H ₂ SO ₄ solution while simultaneously injecting 3M NaCl + 0.5M H ₂ SO ₄ solution at 20°C for one hour[43].	29

Fig. 3.7: The current with time generated from a single pit on AISI 316L in 0.5M H ₂ SO ₄ while simultaneously injecting a 2M NaCl + 0.5M H ₂ SO ₄ , and a SEM photograph of the pit after three hours propagation[79].	30
Fig. 4.1: The different sample types provided for the experimental work.	33
Fig. 4.2: Schematic illustration of the test cell used to record anodic CPP curves.	35
Fig. 4.3: The experimental set up used to record anodic CPP curves.	36
Fig. 4.4: Schematic illustration of the test set up used to conduct OCP measurements.	37
Fig. 4.5: The experimental set up used to conduct OCP measurements.	38
Fig. 4.6: The samples prepared prior to the salt spray exposure and anodic CPP.	39
Fig. 4.7: The samples placed in the salt spray chamber.	40
Fig. 4.8: The samples after 27 days in the salt spray chamber. Mineral wool was placed on selected samples and A-316L showed corrosion attack.	41
Fig. 4.9: The samples prepared prior to the artificial pit experiments.	44
Fig. 4.10: Schematic illustration of the test set up where a A-316L sample with an artificial pit is connected to the 6Mo external cathode.	46
Fig. 4.11: The experimental set up for the beaker containing the artificial pit sample connected to 6Mo with a surface area of 36.8 cm ² and the freely exposed artificial pit sample.	46
Fig. 4.12: The experimental set up used to conduct cathodic potentiodynamic polarisation for the 6Mo sample in 5 wt% NaCl and 6 wt% FeCl ₃ .	47
Fig. 4.13: Example of a pit depth (z) measurement obtained by IFM.	48
Fig. 4.14: Example of a pit diameter (delta I) measurement obtained by IFM.	48
Fig. 5.1 Anodic CPP curves for A-316L, B-316L, 317L and 316 Plus obtained in 3 wt% NaCl at RT.	52
Fig. 5.2: Anodic CPP curves for A-316L, B-316L, 317L and 316 Plus obtained in 3 wt% NaCl at 35°C.	52
Fig. 5.3: Anodic CPP curves for A-316L, B-316L, 317L and 316 Plus obtained in 5 wt% NaCl at RT.	53
Fig. 5.4: Anodic CPP curves for A-316L, B-316L, 317L and 316 Plus obtained in 5 wt% NaCl at 35°C.	53
Fig. 5.5: The A-316L surface after anodic CPP in 5 wt% NaCl at 35°C.	56
Fig. 5.6: The B-316L surface after anodic CPP in 5 wt% NaCl at 35°C.	56
Fig. 5.7: The 317L surface after anodic CPP in 5 wt% NaCl at 35°C.	56

Fig. 5.8: The 316 Plus surface after anodic CPP in 5 wt% NaCl at 35°C.	56
Fig. 5.9: OCP measurement for A-316L in 5 wt% NaCl at 35°C (day 0-14) and at RT (day 14-16).....	57
Fig. 5.10: OCP measurement for B-316 L in 5 wt% NaCl at 35°C (day 0-14) and at RT (day 14-16).....	58
Fig. 5.11: OCP measurement for 317L in 5 wt% NaCl at 35°C (day 0-14) and at RT (day 14-16).	58
Fig. 5.12: OCP measurement for 316 Plus in 5 wt% NaCl at 35°C (day 0-14) and RT (day 14-16).	59
Fig. 5.13: 3D photograph of the pitted area on the lateral edge of A-316L after the OCP measurement in 5 wt% NaCl at 35 °C for 14 days and at RT for two days.	60
Fig. 5.14: Pits on B-316L surrounded by a brown and blue colour after the OCP measurement in 5 wt% NaCl at 35 °C for 14 days and at RT for two days. a) Several pits obtained with 5X magnification and b) the characteristics of these pits obtained with 50X magnification.	60
Fig. 5.15: The amount of Fe (wt%) at the spots and bulk surface for B-316L.....	61
Fig. 5.16: The amount of Cr (wt%) at the spots and bulk surface for B-316L.....	61
Fig. 5.17: The amount of Mo (wt%) at the spots and bulk surface for B-316L.	62
Fig. 5.18: Shallow dish shaped pits on 316 Plus after the OCP measurement in 5 wt% NaCl at 35 °C for 14 days and at RT for two days.....	62
Fig. 5.19: Pit on 316 Plus after the OCP measurement in 5 wt% NaCl at 35 °C for 14 days and at RT for two days.....	63
Fig. 5.20: Indications of a pit that repassivated shortly after initiation on 316 Plus after the OCP measurement in 5 wt% NaCl at 35 °C for 14 days and at RT for two days.	63
Fig. 5.21: The samples after 67 days in the salt spray chamber at 35 ± 2 °C with a 5 wt% NaCl salt spray solution. Crevice corrosion was observed on A-316L, B-316L and 316 Plus. 64	64
Fig. 5.22: Weight loss per unit area of A-316L, 317L, 316 Plus and B-316L after exposure in the salt spray chamber kept at 35± 2 °C with a 5 wt% NaCl salt spray solution. The samples are divided into groups depending on the different experimental variables during the exposure.	66
Fig. 5.23: Crevice corrosion attack on A-316L after exposure in the salt spray chamber at 35 ± 2°C with a 5 wt% NaCl salt spray solution.....	67
Fig. 5.24: Crevice corrosion attack on B-316L after exposure in the salt spray chamber at 35 ± 2°C with a 5 wt% NaCl salt spray solution.....	67

Fig. 5.25: Crevice corrosion attack on 316 Plus after exposure in the salt spray chamber at $35 \pm 2^\circ\text{C}$ with a 5 wt% NaCl salt spray solution.	67
Fig. 5.26: A-316L after exposure in the salt spray chamber at $35 \pm 2^\circ\text{C}$ with a 5 wt% NaCl salt spray solution and mineral wool placed on the surface. Small and insignificant pitting corrosion attacks are marked with red circles.....	67
Fig. 5.27: Anodic CPP curves obtained in 5 wt% NaCl at $35^\circ\text{C} \pm 2$ for the samples with coating that simulated a crevice.....	68
Fig. 5.28: Potential development for sample 1 during the entire exposure period, where the electrolyte was changed from 6 wt% FeCl_3 to 5 wt% NaCl after 26 days.	70
Fig. 5.29: Potential development during the entire exposure period for sample 2 in 6 wt% FeCl_3	71
Fig. 5.30: Potential development the first 10 hours for sample 2 in 6 wt% FeCl_3	71
Fig. 5.31: Potential development during the entire exposure period for sample 3, which was freely exposed in 6 wt% FeCl_3 . The electrolyte was changed to 5 wt% NaCl after 26 days.	72
Fig. 5.32: Galvanic current development for sample 1, which was connected to 6Mo sample with a surface area of 36.8 cm^2 in 6 wt% FeCl_3 and in 5 wt% NaCl at the end of the test.	73
Fig. 5.33: Galvanic current development for sample 2, which was connected to a 6Mo sample with a surface area of 6.3 cm^2 in 6 wt% FeCl_3	73
Fig. 5.34: Accumulated volume loss (cm^3) as a function of time (days) for sample 1 and 2 in 6 wt% FeCl_3 with the corresponding trendlines (stippled lines) and functions.....	75
Fig. 5.35: Accumulated volume loss (cm^3) as a function of time (days) for sample 1 in 5 wt% NaCl with the corresponding trendline (stippled line) and function.....	75
Fig. 5.36: Cathodic potentiodynamic polarisation curves for 6Mo conducted in 6 wt% FeCl_3 and 5 wt% NaCl, and the anodic CPP curve for A-316L conducted in 6 wt% FeCl_3	76
Fig. 5.37: The samples after the artificial pit experiment before cleaning and removing the coating. a) Sample 1 connected to an external cathode area of 36.8 cm^2 and the freely exposed sample 3, and b) sample 2 connected to an external cathode area of 6.30 cm^2 . Corrosion products in varying amount can be observed from the pits.	77
Fig. 5.38: The samples surfaces after the artificial pit experiment when the coating was removed.....	77
Fig. 5.39: Topography of sample 1 that was connected to an external cathode area of 36.8 cm^2 with the scale bar presenting the depth (mm) corresponding to the colours.	79
Fig. 5.40: Topography of sample 2 that was connected to an external cathode area of 6.30 cm^2 with the scale bar presenting the depth (mm) corresponding to the colours.	79

Fig. 5.41: Topography of sample 3 that was freely exposed with the scale bar presenting the depth (mm) corresponding to the colours. 80

Fig. 5.42: The A-316L surface after anodic CPP in 6 wt% FeCl₃ at RT. 80

Fig. 6.1: E_{pit} obtained from the anodic CPP curves at each test condition as a function of Mo content. 82

Fig. 6.2: E_{rep} obtained from the anodic CPP curves at each test condition as a function of Mo content. 84

List of tables

Table 2.1: The alloying elements (wt%) for AISI 316L[5].	3
Table 3.1: PREN, Mo content and E_{pit} obtained in 0.5M NaCl at $23\pm 2^{\circ}\text{C}$ for different AISI 316Ti grades[75].	25
Table 4.1: Chemical composition (wt%) of the test materials used in the experimental work.	32
Table 4.2: Calculated PREN for each test material.	32
Table 4.3: The different test conditions used to record anodic CPP curves.	34
Table 4.4: The weight (g) of the coated samples prior to the salt spray test.	40
Table 4.5: The experimental set ups for the artificial pit experiments.	45
Table 5.1: Parameters obtained from the anodic CPP curves recorded in 3 wt% NaCl at RT. 54	54
Table 5.2: Parameters obtained from the anodic CPP curves recorded in 3 wt% NaCl at 35°C	54
Table 5.3: Parameters obtained from the anodic CPP curves recorded in 5 wt% NaCl at RT. 54	54
Table 5.4: Parameters obtained from the anodic CPP curves recorded in 5 wt% NaCl at 35°C	54
Table 5.5: The potential (V) where metastable pitting starts at the different test conditions. . 54	54
Table 5.6: Average pit depth and diameter, number of pits and pit rating according to ASTM G46 for each sample after recording anodic CPP curves in 5 wt% NaCl at 35°C	55
Table 5.7: Weight loss per unit area and visual observation of the samples after exposure in the salt spray chamber with a 5 wt% NaCl salt spray solution at 35°C . The visual observation was divided into crevice corrosion (cc) underneath the coating, pitting corrosion (pc) and no corrosion (nc).	65
Table 5.8: Parameters obtained from the anodic CPP curves of the coated samples conducted in 5 wt% NaCl at $35^{\circ}\text{C} \pm 2$	68
Table 5.9: The measured pH of the 6 wt% FeCl_3 and 5 wt% NaCl solutions before and after the artificial pit experiments, and the temperature the pH was measured at.	69
Table 5.10: Actual volume loss and geometrical parameters of the pit on the samples after the artificial pit experiments.	78

Abbreviations

Ag/AgCl	Silver/Silver Chloride
AISI	American Iron and Steel Institute
ASTM	American Society for Testing and Materials
C	Carbon
CCT	Critical Crevice Temperature
CE	Counter Electrode
Cr	Chromium
CPP	Cyclic Potentiodynamic Polarisation
CPT	Critical Pitting Temperature
Cu	Copper
EDS	Energy Dispersive Spectroscopy
Fe	Iron
FeCl ₃	Ferric Chloride
IFM	Infinite Focus Microscope
Mo	Molybdenum
MSE	Mercury-mercurous Sulfate Electrode
N	Nitrogen
NaCl	Sodium Chloride
Ni	Nickel
Mn	Manganese
MnS	Manganese Sulphide
RE	Reference Electrode
PSF	Pitting Susceptibility Factor
RT	Room Temperature
SCE	Standard Calomel Electrode
SEM	Scanning Electron Microscopy
Ti	Titanium
UNS	Unified Numbering System
WE	Working Electrode
XPS	X-ray Photoelectron Spectroscopy

Nomenclature

Symbol	Explanation	Unit
A	Area	cm ²
OCP (E_{corr})	Open Circuit Potential	V
E_{crev}	Crevice potential	V
E_{pit}	Pitting potential	V
E_{rep}	Repassivation potential	V
F	Faradays constant	As/mol
I	Current	A
i	Current density	A/cm ²
i_{crit}	Critical current density	A/cm ²
i_{pass}	Passive current density	A/cm ²
k	Material and pH constant	A/cm
M	Molar mass	g/mol
n	Oxidation number	1/mol
t	Time	s
ρ	Density	g/cm ³
wt%	Weight percentage	
x	Diffusion distance	cm

1 Introduction

1.1 Background and motivation

Stainless steels are used on oil and gas platforms for different process systems located topside in marine atmosphere. In this service environment, the stainless steels are inevitable in contact with humidity and chloride ions leading to the possibility of corrosion. The austenitic stainless steel AISI 316L (UNS S31603) has been used for piping and equipment in many decades due to the wide availability, low cost and corrosion resistance. According to NORSOK M-001[1], the maximum operating temperature for uncoated AISI 316L in marine atmosphere is 60°C. However, the corrosion resistance has proven to be insufficient in marine atmosphere even at ambient temperature the past decade.

The alloying composition is one of the most important factors affecting corrosion resistance. Along with a growing demand, more cost effective solutions are searched for by the manufactures, which can be obtained by reducing the content of costly alloying elements within the requirement according to standards. Particularly reduced molybdenum content to the lower limit allowed by standards has been suspected to cause a reduction in corrosion properties of AISI 316L. It is well known that molybdenum improves the corrosion resistance, but the effect of small changes (0.5 wt%) is still an undefined issue.

The main corrosion challenges with AISI 316L in marine atmosphere are pitting and crevice corrosion[2]. Since high costs are associated with replacing existing AISI 316L piping and equipment on oil and gas platforms with higher alloyed stainless steels, the severity of the corrosion attacks is of interest regarding the integrity. Pitting and crevice corrosion attacks penetrating deep into the wall thickness of piping and equipment can cause leakages as a consequence. Few leaks compared to the amount of attacks have been observed, which causes the suspicion that pitting and crevice corrosion attacks reach a limited pit size. Accordingly, insight into the long-term pit propagation is necessary to obtain cost efficient solutions for AISI 316L piping and equipment subjected to pitting and crevice corrosion attacks in the future.

1.2 Objective

The main objective of this study is to investigate the effect of small changes in molybdenum content on the corrosion properties for AISI 316L and to study propagation of a single pit through a literature survey and experimental work. In the experimental work, the effect of chloride concentration and temperature on the corrosion properties of AISI 316L and similar alloys containing different molybdenum content is included in the objective. The objective of the pit propagation study is to develop and conduct a method to study propagation of a single pit, where the main focus is to investigate if the pit reaches a limited size due to repassivation and the effect of the cathode area.

1.3 Limitations

This study is limited to external corrosion of uncoated and not insulated AISI 316L and similar grades in marine atmosphere. Since the time to execute this master thesis was restricted, some other limitations were made as well. AISI 316 and 316L are treated as AISI 316L since these steels are similar except for the carbon content. Carbon content is important regarding chromium carbide formation that can cause intergranular corrosion, which is not in the objective of this thesis. The temperature for the experimental work is limited to 35°C since AISI 316L is normally not used above this temperature. Furthermore, surface finish can affect the chemical composition of the passive film, but in order to meet the time frame this topic are only slightly studied.

1.4 Approach

A literature survey is performed to obtain previous research carried out on the related topics for the experimental work in this thesis. To investigate the effect of small changes in molybdenum content several experiments were conducted and evaluated before comparing the results to obtain a reliable result. Simultaneously, the experiments were compared to the obtained results from the literature survey. The method for examining propagation of pits was developed by manufacturing artificial pits and simulating the environment developing inside a propagating pit. This method was conducted in three different manners to investigate the effect of cathode area and propagation of a single pit.

2 Theoretical background

2.1 Austenitic stainless steels

Stainless steels generally contain iron (Fe) and chromium (Cr), and the addition of austenite stabilising elements such as nickel (Ni) and manganese (Mn) in sufficient quantities transform the structure to austenite. To obtain austenite structure at room temperature iron alloys requires about 17 wt% Cr and 11 wt% Ni or Ni equivalents (Mn, N, C)[3]. Suitable alloying increases the corrosion resistance since the alloy composition affects the passive film composition and properties[4]. The alloying elements for AISI 316L according to ASTM A 312/A 312M are presented Table 2.1[5]. Only the elements that affects pitting and crevice corrosion resistance will be further discussed.

Table 2.1: The alloying elements (wt%) for AISI 316L[5].

C	Mn	P	S	Si	Cr	Ni	Mo
0.035	2.00	0.045	0.030	1.00	16.00-	10.00-	2.00-
					18.00	14.00	3.00

The most important alloying element is Cr since it determines the ability to form a passive film on the steel surface[6]. In particularly chloride containing environments, molybdenum (Mo) is added to increase the pitting corrosion resistance[7]. As the Cr or Mo content increase, Ni equivalents must be added in matching amounts[8]. Furthermore, the Ni content in austenitic stainless steel can be partly replaced by Mn and Nitrogen (N) in order to obtain cheaper alloys[7]. The elements Ni, N and Mn all contribute to passivity[9]. Mn is added at low levels around 1.5 wt% as a deoxidant to remove dissolved oxygen and sulphur (S) during steel refining and as a substitute for some Ni. Mn is a strong sulphur former that ties up sulphur, which causes manganese sulphide (MnS) to precipitate as an inclusion[10]. MnS inclusions are the main corrosion initiation site for austenitic stainless steels, and thus an undesirable element regarding the corrosion resistance[11].

Some of the AISI 316L qualities that will be presented later in the report are additionally alloyed with N, copper (Cu) and titanium (Ti). Alloying with N is limited by the solubility[3], and 0.2-0.7 wt% is commonly added to stabilise and strengthen the austenite phase[9]. Additions of N in Mo containing austenitic stainless steel have a strong synergistic positive effect. The combined effect of N and Mo on pitting corrosion resistance is improved compared to the

individual effects[6, 9], which will be further discussed later in the report. Ti is added to reduce the risk of sensitisation, however this is not an issue for austenitic stainless steel containing less than 0.03 wt% C[7]. Cu stabilises the austenite phase, which permit lower Ni content to be used[12], and Cu may enhance the corrosion resistance[4, 12].

2.2 Passive films

The corrosion resistance of stainless steel arises due to a thin oxide film in the order of 1-3 nm thickness on the metal surface, which causes the reaction rate between the stainless steel and environment to be reduced several magnitudes[4]. Growth of passive films are time dependent, and when stainless steels are exposed to a specific environment the passive film grows until a steady state is reached[13]. The structure of passive films formed under atmospheric conditions are essentially similar to that in aqueous solutions, but the composition may differ[14].

The passive film on austenitic stainless steel consists of an inner oxide barrier and an outer deposit film containing salts or hydroxides of the alloy constituent metals. The inner oxide film is less hydrated and thicker than the outer film. Even though austenite stabilising elements improve the chemical stability, the passive film does not always contain each of the alloying elements. Especially in the inner barrier layer, mainly Cr and Mo contribute to passivity since Fe and Ni are likely to dissolve[9].

Bastidas et al.[15] investigated the passive film on AISI 316L in 5 wt% NaCl at RT. The X-ray photoelectron spectroscopy (XPS) spectra showed that the passive film polarised to -0.01 V vs SCE (passive region) and 0.07 V vs SCE (close to E_{pit}) consisted of an inner layer with a mixture of Cr and iron oxides, and a Cr hydroxide outer layer. The Mo content in the passive film was deficient. However, some MoO_2 and chloride were additionally detected at 0.07 V vs SCE. Since no sodium signal was detected, it indicates that complexes of Mo and chloride were formed. The thickness of the oxide film was 1.5 nm[15].

Jung et al.[14] studied the passive film on AISI 316L and 304 formed under wet-dry cyclic conditions at 60°C with 0.1M NaCl solution. Since the XPS spectra of Mo and Ni were weak, they were not included in the analysis. The chloride content in the thin water film affected the composition especially in the hydroxide layer, but not the thickness. The passive film thickness during the wet dry cycles is presented in Fig. 2.1[14]. The Cr content in the hydroxide layer

was similar to the bulk composition of AISI 316L, while the Cr content was higher in the oxide layer. As the passive film forms under wet-dry cyclic conditions or constant humid conditions, iron selectively dissolves into the thin water layer causing Cr enrichment in the passive film with time. Alloys containing Mo attain a more compact passive film since Mo suppresses dissolution of Fe[14].

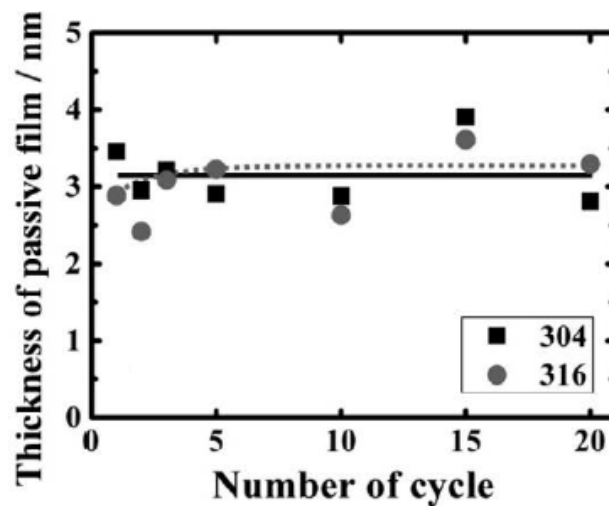


Fig. 2.1: The passive film thickness for AISI 316L and 304 formed under wet dry cyclic conditions at 60 °C with 0.1M NaCl[14].

2.3 Corrosion mechanisms

Pitting and crevice corrosion of stainless steels are similar. Localised corrosion attacks initiated at an open surface are named pitting corrosion, while attacks initiated at an occluded region are named crevice corrosion[16]. Pitting corrosion causes different cross-sectional pit shapes to be formed on the surface as presented in Fig. 2.2[17], while crevice corrosion attacks may appear as uniform corrosion or pits[18].

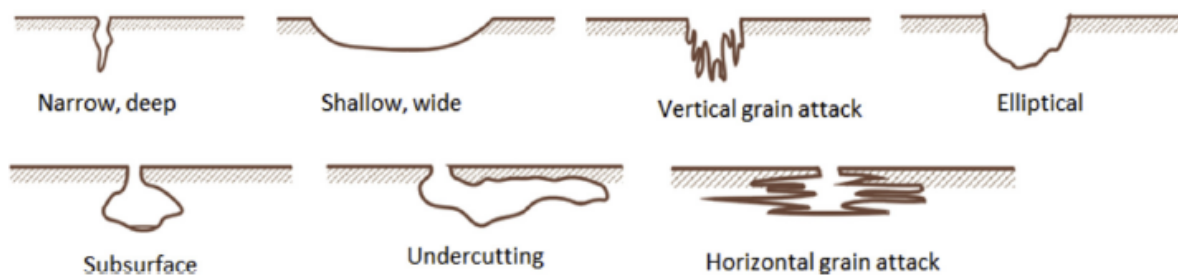


Fig. 2.2: Different cross-sectional pit shapes[17].

Both pitting and crevice corrosion are affected by pH, temperature and bulk chloride concentration in similar ways. However, the conditions necessary for initiation are less severe for crevice corrosion[19]. The main difference between these corrosion mechanisms are the initiation process, while the chemistry developing inside a pit or crevice is similar. In this chapter an introduction to these corrosion mechanisms are presented, while propagation of pitting and crevice corrosion will be further presented in chapter 2.4. A short introduction to galvanic corrosion is additionally provided in this chapter since this mechanism affects the pit propagation study in the experimental work.

2.3.1 Crevice corrosion

The local acidification model is a commonly accepted model for crevice corrosion initiation. This model and other proposed models failed to explain all aspects of crevice corrosion in a review[20]. Another investigation[19] suggested that the mechanisms were either local acidification or metastable pitting stabilised by the crevice depending on temperature. However, to give an introduction to crevice corrosion the local acidification will be described since it is the most widespread mechanism.

The chemistry that develops within an active crevice is illustrated in Fig. 2.3[21], where the gap between the crevice former and metal surface is typically between 0.1 to 100 μm [18]. Metal dissolution and oxygen reduction occurs within and outside the crevice at first as presented in Eq. 2.1 and 2.2, respectively[19], where metal M is assumed to be Fe, Cr, Ni and Mo for AISI 316L[19].

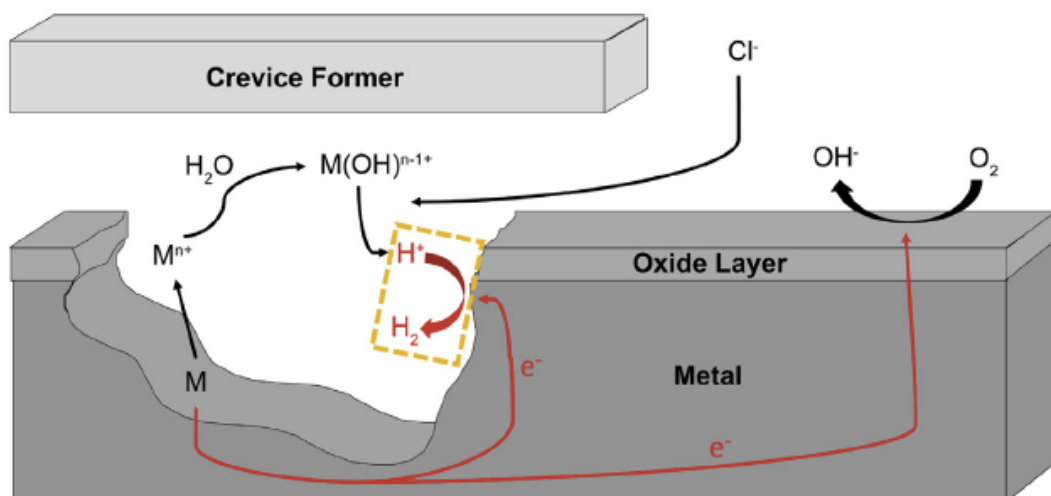


Fig. 2.3: The chemistry that develops within an active crevice during crevice corrosion[21].

Other species than oxygen may contribute to the net cathodic current, however oxygen is the most prevalent for steels exposed to electrolytes in air, and with respect to total cathodic current capacity the amount of other species are insignificant[22]. As the reactions proceed, oxygen inside the crevice is consumed and the crevice becomes a local anode, which is balanced by oxygen reduction on the passive surface surrounding the crevice[20]. Since hydroxide (OH^-) is not produced inside the crevice, chloride ions migrate into the crevice to sustain charge neutrality[23]. Simultaneously, hydrolysis of metal cations inside the pit according to Eq.2.3 occurs[24].

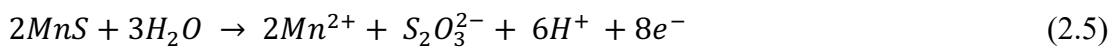


These processes cause an aggressive electrolyte to develop inside the crevice, which accelerates metal dissolution and the subsequent chloride ion migration and metal cation hydrolysis. Once the electrolyte is sufficient aggressive to cause passive film breakdown, crevice corrosion is initiated[19]. As the corrosion process proceeds, the anodic dissolution inside the crevice is balanced by the cathodic current consumed at the free surface surrounding the crevice former. Thus, the available cathodic current and a higher corrosion potential is obtained in the crevice at a larger free surface and higher conductivity of the bulk solution[25]. Hydrogen evolution according to Eq.2.4[23] may act as supplementary cathode during growth due to decreased pH and thereby a sufficient amount of H^+ generated[23]. Precipitation of the corresponding chloride salt for the Fe, Cr, Ni and Mo cations limits the cation amount inside a pit or crevice, which can limit the minimum pH achieved[26].

Ions produced by the anodic reaction move through the solution under the influence of the forces potential gradients due and concentration gradients[27]. Due to restricted geometry that limits mass transport, large potential and concentration gradients can develop between the crevice and surrounding cathode area[18]. The potential drop and diffusion of fluxes between the anode and cathode are controlled by the same restricted transport path. Consequently, the potential drop is larger the more limited diffusion transport[25]. At atmospheric conditions restricted diffusion of Fe ions causes an acidic ferric chloride solution to develop inside the crevice, which accelerates the dissolution[28].

2.3.2 Pitting corrosion

Pitting corrosion can be divided into the three steps initiation, metastable propagation and stable propagation[29]. A schematic illustration of the pitting corrosion mechanism under thin electrolyte layers is presented in Fig. 2.4[30]. Initiation involves local passive film dissolution at inclusions or surface defects[29] such as grain boundaries[23]. In marine atmosphere, initiation on AISI 316L is often associated with dissolution of MnS inclusions that can be described as in Eq. 2.5, which causes the pH to decrease locally and dissolution of the alloying elements Fe, Cr, Ni and Mo[31]. This condition creates a metastable pit where repassivation can easily occur[29].



Depending on material composition, mass transport, potential in the pit bottom and the electrolyte, metastable pits can become stable propagating pits. If the open circuit potential (OCP) exceeds the pitting potential (E_{pit}) stable pitting can occur[17]. The possibility of metastable pits growing into stable pits increases if the potential at which metastable pits are formed increases[32]. Once a pit starts to propagate, further pit propagation is promoted due to the local aggressive conditions caused by diffusion of chloride ions to sustain charge neutrality and hydrolysis of metal cations. Furthermore, the pH is higher at the cathode area represented by the humid surface surrounding the pit[16].

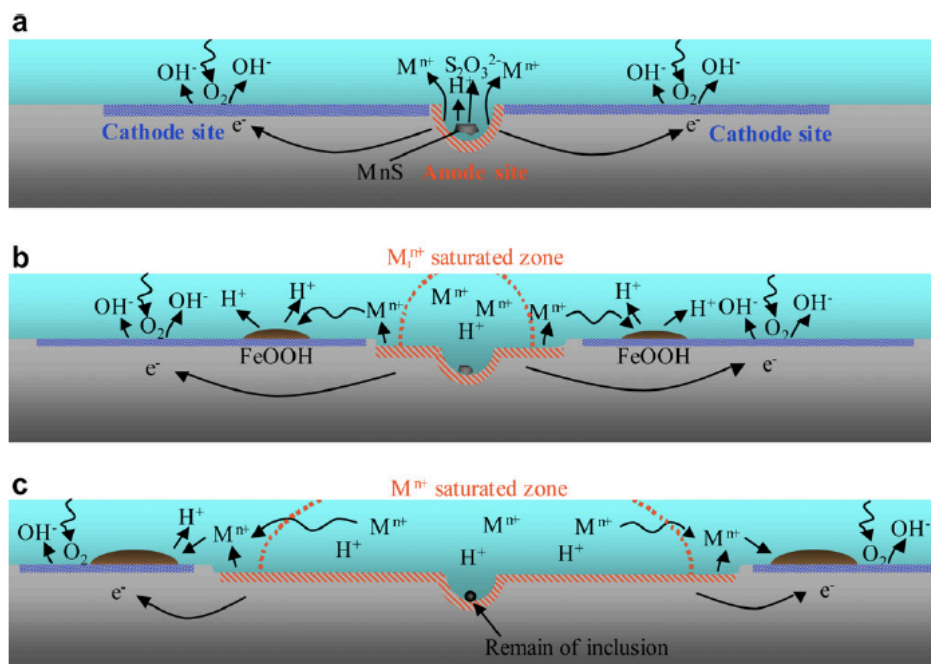


Fig. 2.4: Schematic illustration of the pitting corrosion mechanism under a thin electrolyte layer where the pit initiates at an MnS inclusion[30].

The difference between mass transport during pitting corrosion at immersed conditions and atmospheric conditions are presented Fig. 2.5[33]. Due to the electrolyte geometry under atmospheric conditions, mass transport is limited mainly to the lateral area, which causes increased concentration of corrosion products and decreased pH in the electrolyte surrounding the pit. This condition encourages pit propagation and generation of pits in the adjacent area of the existing pit[33]. The dissolved Fe ions diffuse towards the pit mouth and oxidises to iron oxide, and as the pit deepens the iron chloride concentration increases as for crevice corrosion[28].

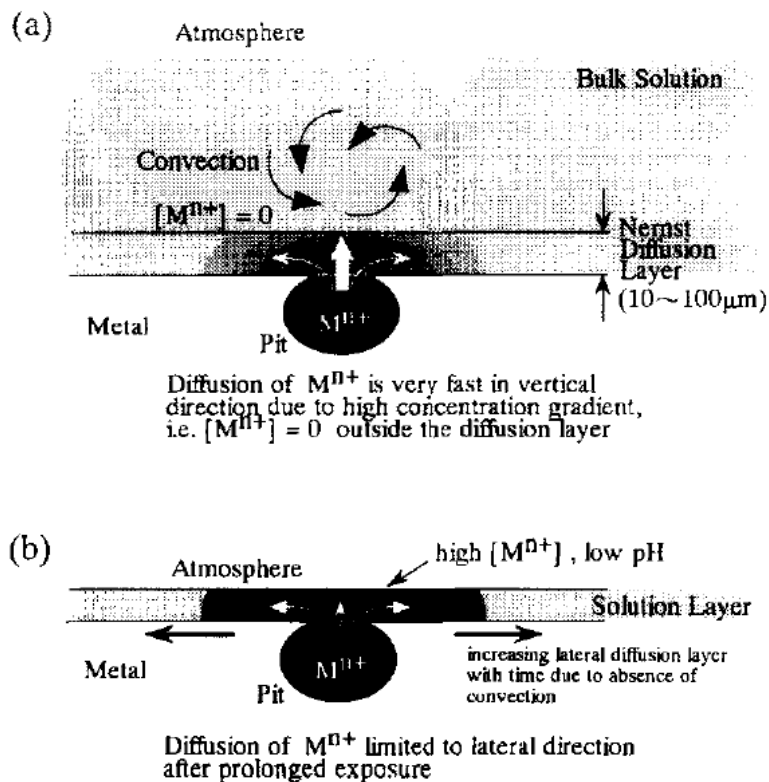


Fig. 2.5: The difference in mass transport between a) immersed conditions and b) atmospheric conditions[33]. The quality is poor due to the original source.

As corrosion products is formed at the pit site, the long-term corrosion behaviour can be affected. Lv et al.[31] investigated the corrosion products formed on AISI 316L by a wet-dry cyclic accelerated test, which is characteristic for a metal surface in marine atmosphere. At 35°C with a 5 wt% NaCl salt spray solution the corrosion products consisted of Fe, Cr and Ni oxides and hydroxides. Since corrosion products serves as a physical barrier and the ratio $[\text{Cr}]/([\text{Cr}]+[\text{Fe}])$ in the corrosion products increased with time, the protective ability of the corrosion products was concluded to increase with time[31].

The aggressiveness of the electrolyte inside the pits can be characterised by metal cation concentration since the pH and chloride concentration are fixed through hydrolysis and charge balance, respectively[32]. The chloride concentration may reach 12M, while the pH can approach zero[34]. Furthermore, during pit initiation and growth the anodic currents densities can be as high as 0.1-10 A/cm²[35]. The local low pH and potential conditions causes hydrogen evolution to occur inside pits even at high anodic potentials. However, cathodic reactions inside pits may only support around 5% of the anodic current[36]. In addition to electrolyte composition and local pH changes, the potential drop within the electrolyte are important for stable pit propagation[37].

2.3.3 Galvanic corrosion

When dissimilar metals are electrically coupled (galvanic coupling) in a common solution the potential difference between the metals causes electron flow between them. The surface of the less corrosion resistant metal becomes the anode, while the surface of the more corrosion resistant metals becomes the cathode. This causes the corrosion rate to increase for the less corrosion resistant material[38]. The current flow in a galvanic coupling results in a potential shift due to polarisation since the potential on each metal tend to approach each other, where the magnitude depends on the initial potential and the environment. Hence, the developed potential between the metals is the driving force for the galvanic current flow. The resulting polarisation is affected by the cathode to anode ratio, where a large cathode area compared to anode area results in a higher corrosion rate[38].

2.4 Pit propagation

During pit propagation in marine atmospheric conditions the effective cathode area surrounding the pit is small since the electrolyte is a thin water film or droplet[39]. This influences pit propagation since the effective cathode area is small compared to immersed conditions[22]. The main parameter determining if pits initiates and propagates are the geometry, chemistry and conductivity of the electrolyte layer formed on the steel surface[39].

As the pit propagates the cathode area and the dissolving anodic pit can be thought of as a galvanic coupling as illustrated in Fig. 2.6[40]. The oxidation reactions at the pit site generates electrons, which is consumed by the cathodic reactions at the pit site or at a distance away from the pit[22]. The potential on the cathode increases from the pit mouth until it reaches E_{corr}

(OCP), simultaneously the current decreases. E_{rep} at the pit mouth represents the least noble potential at which the pit can continue to propagate[40]. If a crevice former is present, the crevice is in an active state at E_{rep} or at more noble potentials[41]. At atmospheric conditions limitations in pit size can occur due to ohmic drop between the pit mouth and cathode or limitations in generated anodic current or cathodic current[42]. The limitations in generated anodic current can be explained by pit stability, while cathode limitations can be explained in terms of factors affecting cathode capacity (total cathodic current) such as cathode area size.

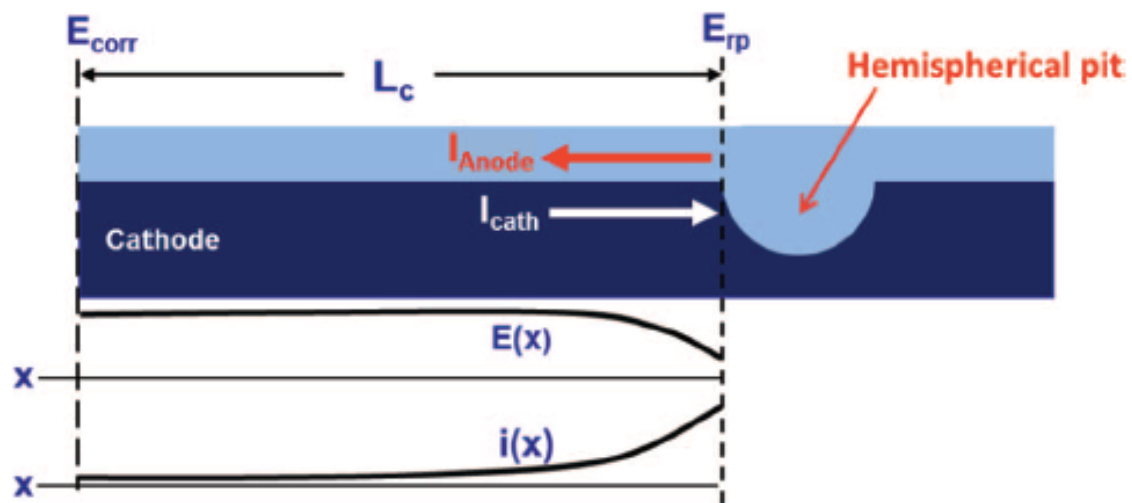


Fig. 2.6: Illustration of the galvanic coupling during atmospheric pitting corrosion[40].

2.4.1 Pit stability

Stable pit propagation on stainless steels are under diffusion control at the pit bottom[43-45], and the diffusion barrier against transport of ionic species is provided by the pit depth. During stable pit propagation the diffusion barrier is sufficient to maintain the aggressive electrolyte necessary for metal dissolution. On the contrary, at the metastable stage the pit depth is an insufficient barrier to diffusion and the barrier is provided by a pit cover that is a remnant of the passive film[44]. The diffusion process can be described by a pit stability product, which was developed by Galvele[46]. The pit stability product is a criterion that was later defined by Pistorius and Burstein[32], which states that the product of the current density and pit depth must exceed a minimum value to sustain stable pit propagation. Initially the pit stability product described the pit initiation conditions, and later it has been extended to pit propagation[47].

The pit stability product principle is illustrated in Fig. 2.7[48], where x represents the pit depth. Anodic dissolution occurs only at the pit bottom with subsequent metal cation hydrolysis, which lowers the pH and increases the chloride concentration due to migration of chloride ions[40].

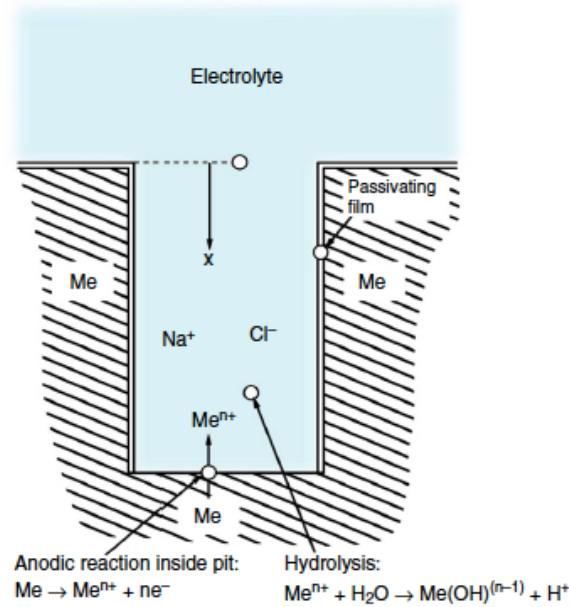


Fig. 2.7: Illustration of the pit stability product principle[48].

Diffusion of aggressive species out of the pit causes dilution of the aggressive chemistry developing inside the pit, which can result in repassivation. When the dissolution rate and resulting hydrolysis of metal cations exceeds the diffusion rate out of the pit, stable pit propagation is obtained[40]. Thus, the pH in the bottom of the pit is sufficient low to maintain active dissolution at values above the pit stability product[36]. The minimum critical current density necessary for pit propagation is hence related to a characteristic depth of the pit, and due to diffusion of metal cations to the outside of the pit the critical current is dependent on pit depth. The mathematical expression for the pit stability product is presented in Eq.2.6[26].

$$x \cdot i_{crit} = k \quad (2.6)$$

Where i_{crit} (A/cm²) is the minimum critical current density, which is a function of the diffusion distance x (cm), and k (A/cm) is a constant that is a function of pH and the material[26]. The illustration in Fig. 2.7 may seem like an oversimplification. However, since x represents the diffusion path, the pit stability product can be modified via geometry[48]. During pit propagation the pit stability product fluctuates around an approximately constant value[32].

2.4.2 Cathode limitations

The two primary factors that determine the cathode capacity to sustain localised corrosion are the oxygen reaction kinetics and the electrolyte properties[49]. Conservation of charge requires that electrons generated during oxidation reactions must be consumed locally or at another area on the metal by a reduction reaction. Thus, electrons generated at the anode must be balanced with electrons consumed at cathodic sites and the anodic reaction rate cannot be greater than the cathodic reaction rate. Cathode limitations can control the dissolution rate of the metal, however the anodic current distribution determines the penetration rate[22].

As the pit propagates the electrolyte at the cathode area surrounding the pit becomes increasingly alkaline due to production of OH^- from the oxygen reduction. Accumulation of OH^- causes the driving force to decrease since the reduction potential shifts towards the cathodic direction. Hence, the cathode capacity to sustain pit propagation decreases with time as the pH at the cathode increases[22].

The ratio of cathode area to anode area is important since it affects the anodic current density[38]. At atmospheric conditions the cathode area contributing to the corrosion process is limited due to ohmic drop in the electrolyte and the humid surface area outside the pit. As the distance from the pit increases the interfacial potential increases due to ohmic drop until it reaches E_{corr} . At all distances beyond this point the local cathode current only supports the local passive current. The ohmic drop in the electrolyte increases as the conductivity decreases, which limits the cathode current that supports pit growth[42]. Ohmic drop in the electrolyte is affected by the thickness and length of the electrolyte, and the presence of particulates or dust which partially moisturises the cathode area[49]. Hence, increased cathode area increases the cathode capacity, however due to the electrolyte conductivity the cathode capacity saturates at a finite cathode size at atmospheric conditions[22].

Since the cathodic current is equal to the anodic current, repassivation is prevented as long as the cathodic current is able to consume the anodic current corresponding to the minimum required current to maintain the critical solution inside the pit[42]. However, in the absence of other limitations repassivation can occur since some level of anodic overpotential are necessary for stable pitting. To consume the produced anodic current by a growing pit, the cathode surface must be increasingly polarised. When the cathode area is polarised below E_{rep} , stable pits repassivate[42].

2.4.3 Pit size calculation

Pit size can be calculated by using Faradays second law as presented in Eq.2.7[34], which is modified to obtain volume loss (cm³).

$$\text{Volume loss} = \frac{M}{nF\rho} \int I \cdot dt \quad (2.7)$$

For numerical applications the parameters for AISI 316L are 2.2 for the mean oxidation number n , $M=56.1$ g/mol and the density ρ is 8 g/cm³, while the Faradays constant $F = 96485$ As/mol[43]. The current I (A) can be measured experimentally for a single pit.

2.5 Factors affecting pitting and crevice corrosion

Pitting and crevice corrosion at marine atmospheric environment are influenced by both temperature and the presence of chloride ions[50]. At marine atmospheric conditions accumulation of chlorides or evaporation of water can cause a high chloride concentration in the thin water layer covering the steel[51]. Furthermore, the temperature on the external steel surface depends on the practical operating temperature for the AISI 316L component. Hence, both the temperature and chloride concentration can vary at marine atmospheric conditions.

2.5.1 Temperature

Temperature is a critical factor for pitting and crevice corrosion since most materials exhibits these corrosion attacks above a certain value, critical pitting temperature (CPT) or critical crevice temperature (CCT)[16], where CCT is generally lower than CPT[19]. CPT and CCT can be determined by using the procedures described in ASTM G48[52] and G150[53]. The result may vary depending on standard and method used, however authors[50, 54] have suggested CPT and CCT for AISI 316L to be respectively 16°C and -2°C, and below.

Increased temperature is expected to influence the corrosion process in several ways. The rate of chemical reactions, including metal dissolution and pit growth, increases with temperature. In addition, faster diffusion of species and increased porosity of the passive film is enhanced[55]. The effect of temperature on the corrosion resistance can be observed by electrochemical measurements. Several authors[56, 57] have demonstrated that increased temperature causes E_{pit} for AISI 316L in NaCl solutions to shift towards lower potentials.

2.5.2 Chloride concentration

The chloride concentration is a critical factor since pitting and crevice corrosion is initiated when the chloride concentration reaches a critical value[33]. Chloride ions present in the electrolyte decreases the stability of the passive film[58]. The ability of chloride ions to produce pitting can be explained by the formation of a chloride complex with cations and hydroxide, increased hydrogen ion activity in the pit and formation of a chloride salt layer in the bottom of the pit[59]. Increased hydrogen activity during pit growth enhances the corrosion rate, and the chloride salt layer prevents repassivation without entirely suppressing metal dissolution[60].

Park et al.[61] investigated the influence of both chloride concentration and temperature on the pitting corrosion behaviour of AISI 304. Chloride concentrations between 0.01-10 M and temperatures in the range room temperature to 90°C were included in the investigation. The temperature was suggested to influence E_{pit} more significantly than the chloride concentration[61].

Ramana et al.[56] studied the effect of chloride concentration and temperature on E_{pit} for AISI 316L. The results are presented in Fig. 2.8[56]. For chloride concentration between 17625 to 70900 ppm at any particular combination of pH and temperature E_{pit} decreased with 40 to 60 mV. Increased temperature caused E_{pit} to decrease with an average of 1.59 mV/°C at different chloride concentrations and pH[56].

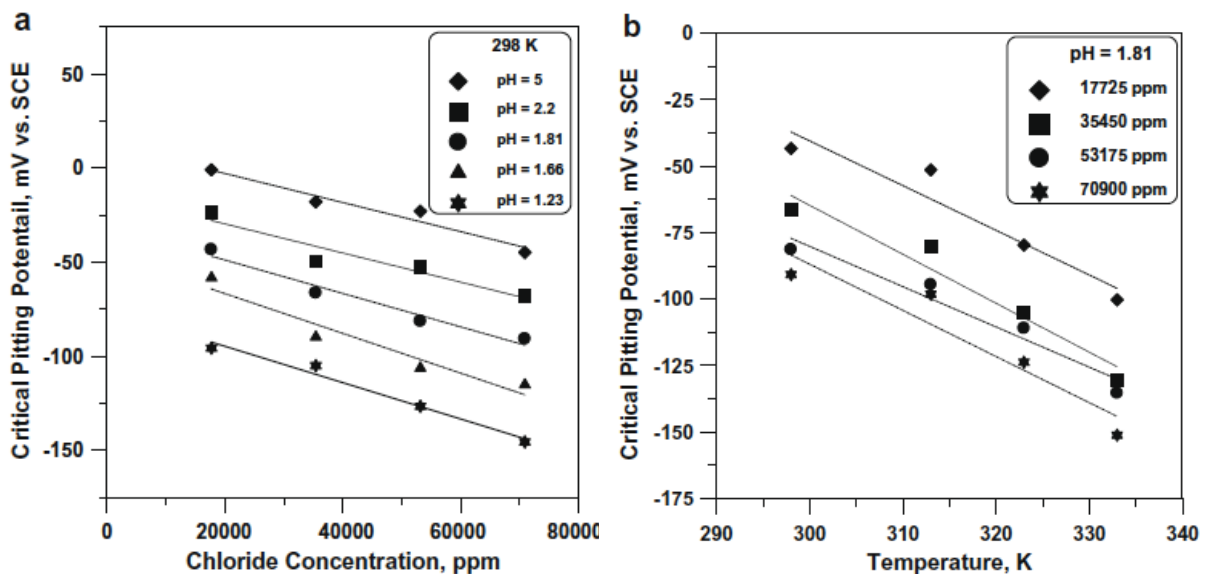


Fig. 2.8: The effect on E_{pit} of a) increased chloride concentration at different pH and b) increased temperature at different chloride concentrations[56].

2.6 Cyclic potentiodynamic polarisation curves

The susceptibility to pitting and crevice corrosion can be evaluated by using cyclic potentiodynamic polarisation technique as described in ASTM G61[62]. The shape of anodic polarisation curves obtained by this technique depends on the corrosion resistance of the material at specific test conditions. However, since the studied materials in this master thesis are expected to exhibit pitting corrosion at the chosen test conditions, a brief introduction to curves obtained from these materials is presented.

A typical curve obtained by using this method for a material exhibiting protection potential is illustrated in Fig. 2.9[58]. The technique involves increasing applied voltage in the anodic direction before reversing the scan direction at a chosen current or voltage[63], as indicated by arrows in Fig. 2.9[58]. Increasing applied voltage causes passive film breakdown, and stable pits start to grow at E_{pit} where the current rises sharply. In the reversed scan the material repassivates at E_{rep} where the current decreases to values representative for passive dissolution[16]. The current density in the passive region is the passive current density (i_{pass})[58]. E_{pit} can be referred to as the crevice potential (E_{crev}) if creviced samples are used[16].

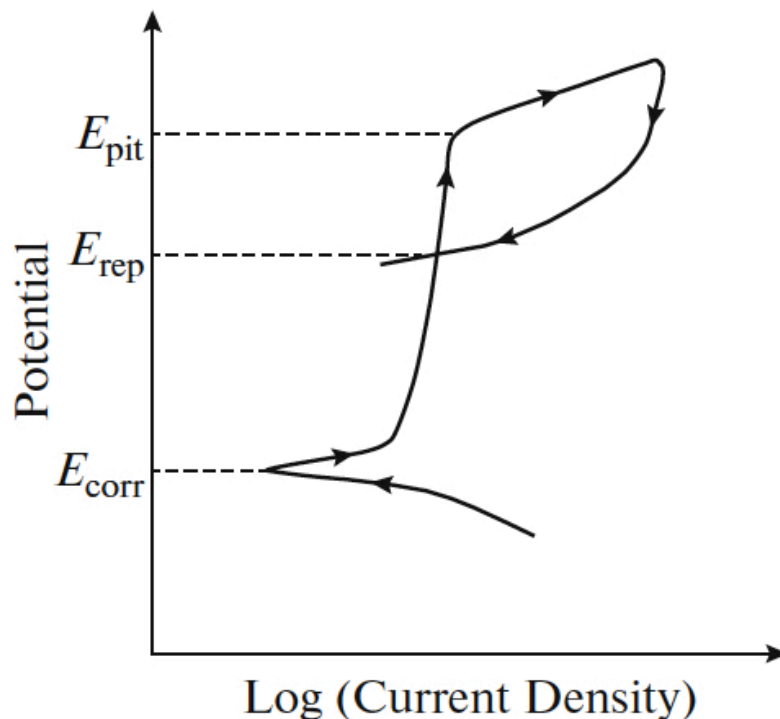


Fig. 2.9: Illustration of a typical cyclic potentiodynamic polarisation curve for a material exhibiting protection potential[58].

The current density difference between the forward and reversed scan creates a hysteresis loop which arises from disruption of the passive film[63]. The size of the hysteresis loop is determined by the current density difference between the forward and reversed scan at the same potential. A greater size means more passive film disruption and more difficulty for restoring the damaged film[58].

In general, at a fixed voltage scan rate the metal is less susceptible to pitting and crevice corrosion the more noble E_{pit} is, and propagation of localised corrosion is less likely the more noble E_{rep} is.[64]. In the region between these potentials metastable pitting may occur, which are pits of micron size with a lifetime of a second or less. Metastable pitting events are characterised as current transients under applied anodic potential or current transients in the active direction at open circuit potential (OCP)[16].

Scan rate and point of scan reversal are parameters that requires to be properly chosen and considered when performing cyclic potentiodynamic polarisation[63]. The scan rate employed affects E_{pit} and E_{rep} [64]. If the scan rate it not sufficient slow the polarisation scan can become incorrect since the current generated does not only reflect the current from the corrosion process[63]. Point of reversal influences E_{rep} since the amount of pit propagation before reversal affects the pit chemistry necessary for repassivation[64]. Accordingly, when comparing different alloys in a constant environment or when investigating an alloy in different environments the reversal point should be constant[63].

2.6.1 Determining features from the curves

Several methods can be used to determine E_{pit} and E_{rep} . In this thesis E_{pit} is determined at the inflection point as illustrated in Fig. 2.10[65]. E_{rep} is determined at the cross-over potential where the hysteresis loop closes as presented in Fig. 2.11[65]. However, since the surface can be subjected to changes due to pitting corrosion, i_{pass} in the reverse scan may be reached before the hysteresis loop closes. In such cases E_{pit} is determined by extrapolating the curve in this thesis.

The i_{pass} can be determined by calculating the average or at the midpoint of the passive current density part of the curve. If the passive current density slope is not steep, defined as an expansion of more than a decade in this thesis, i_{pass} can be stated as an interval.

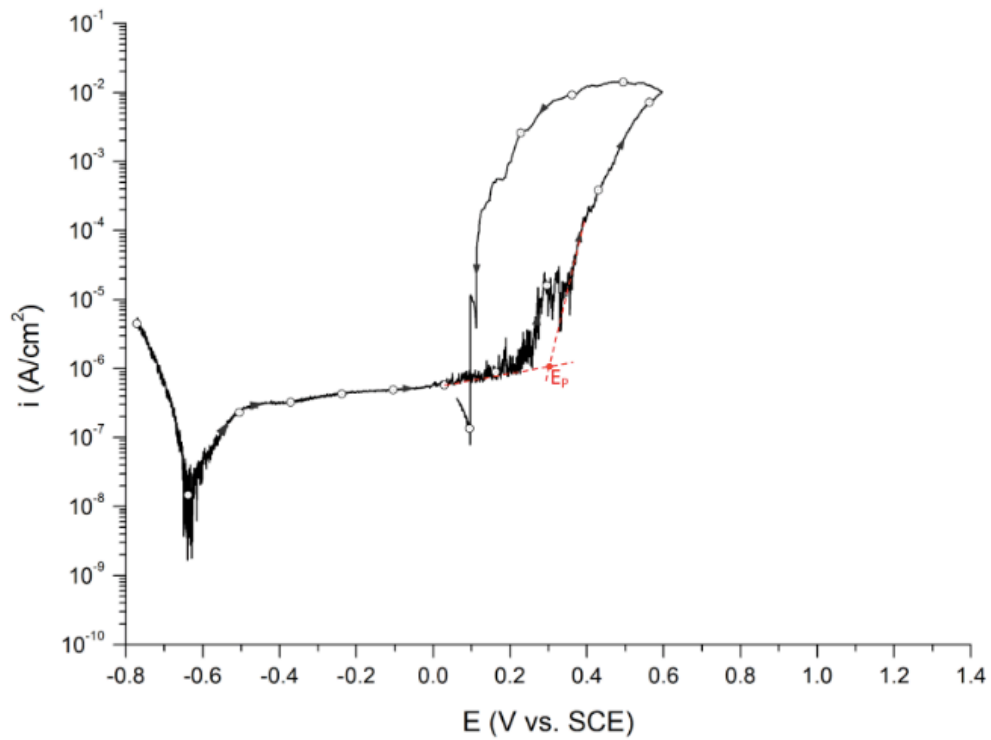


Fig. 2.10: Determining E_P (E_{pit}) from cyclic potentiodynamic polarisation curves[65].

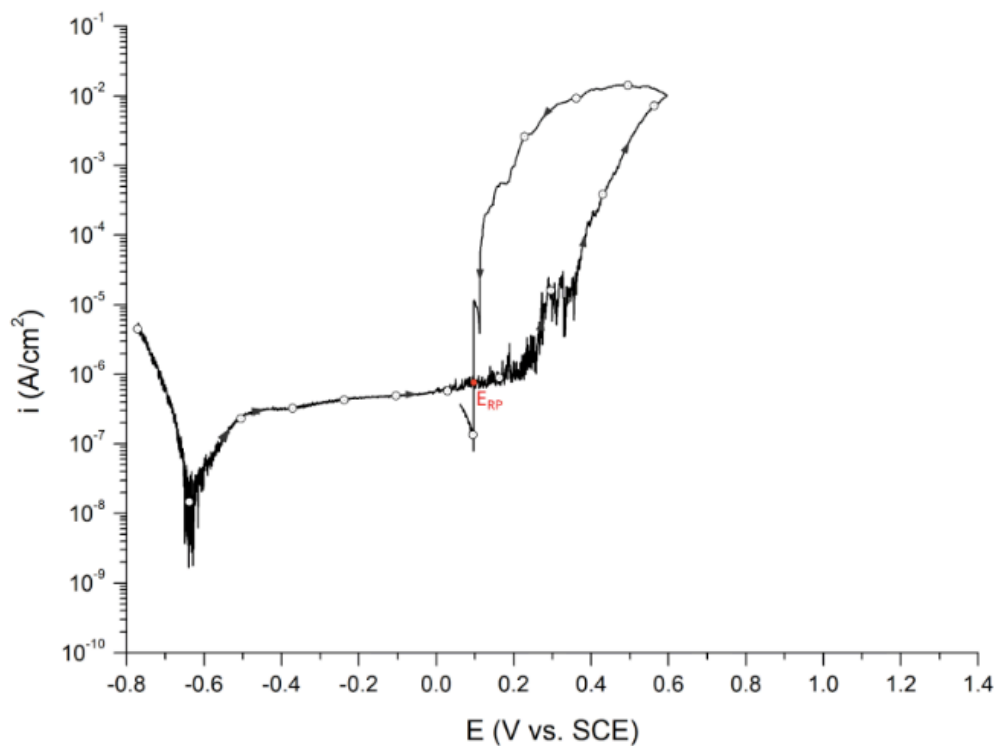


Fig. 2.11: Determining E_{RP} (E_{rep}) from cyclic potentiodynamic polarisation curves[65].

2.7 Ranking of pitting corrosion susceptibility for different alloys

Pitting corrosion resistance is generally ranked by measuring CPT or by calculating the pitting resistance equivalent number (PREN) based on alloying element content[66]. The content in percent mass fraction of the alloying elements Cr, Mo, W and N are used to calculate PREN as presented in Eq.2.8[67]. Since the PREN gives a quantitatively estimate of the resistance to localised corrosion, care should be used when applying PREN.

$$PREN = w_{Cr} + 3.3(w_{Mo} + 0.5w_W) + 16w_N \quad (2.8)$$

The pitting susceptibility factor (PSF) can be used to quantify the pitting corrosion resistance of different alloys if the tested alloy remains passive and exhibits a repassivation potential in the reversed scan[66]. The PSF is determined from parameters obtained from cyclic potentiodynamic polarisation curves and OCP measurements, and can be calculated according to Eq.2.9[66].

$$PSF = \frac{E_{pit} - E_{rep}}{E_{pit} - OCP} \quad (2.9)$$

The PSF is typically in the range 0 to 5, and values above or equal to 1 indicate susceptibility to pitting corrosion. The OCP value from measurement can be replaced by E_{corr} (OCP) from anodic CPP curves since these should correlate well[66].

Pitting corrosion can additionally be evaluated by using standard charts as described in ASTM G46[68], where a quantitative expression indicating the significance is obtained. By using a standard chart, the surface is rated in terms of pit density, size and depth.

3 State of the art

It is well known that Mo enhances the corrosion resistance, however the exact mechanism seems unclear and several theories exist. In this chapter, previous research on the role of Mo and studies conducted to investigate the effect of Mo content for AISI 316L and similar austenitic stainless steels are presented. Few studies on propagation of a single pit on AISI 316L appear to have been conducted, and the previous studies obtained during this master thesis are presented in this chapter as well.

3.1 The role of molybdenum

Mo improves the stability of the passive film, especially in the presence of chlorides. Mo can exist in a number of oxidation states. For austenitic stainless steel Mo^{4+} and Mo^{6+} have been reported to exist in the passive film[9], where Mo^{4+} is preferentially present in the native oxide film and after repassivation Mo^{6+} is preferentially present[69]. The hexavalent states of Mo are MoO_3 and MoO_4^{2-} [4].

Generally MoO_3 exists at the metal/film interface, while MoO_4^{2-} is observed at the film/solution interface[70]. However, the transpassive reaction of Mo depends on the pH of the solution. At pH below approximately 3.5 Mo retains in the passive film as a Mo^{6+} oxide, while at higher pH Mo dissolves into the solution as MoO_4^{2-} [71]. The amount of Mo in the passive film is at a few atomic percent level and the influence on passive film thickness is not significant[69]. Higher Mo content in the alloy causes higher Mo content in the passive film, thus i_{pass} can decrease as a result[70].

Pure Mo may contribute to passivity before it exhibits transpassive dissolution in the passive region of austenitic stainless steel[9, 71]. Cr has been suggested to suppresses the transpassive dissolution of Mo since the Mo^{6+} oxide is fixed in the state solid solution with Cr oxides and hydroxides in the passive film. Since the stability of Mo^{6+} oxide is high in chloride containing solutions, the resistance to pitting corrosion increases[71].

The passive film contains chlorides in environments where chlorides are present. Chloride ions are proposed to substitute for oxygen in the passive film causing the passive film stability to decrease since the number of cation-oxygen bonds declines. Passive films on Mo containing

alloys are suggested to contain less chlorides due to the formation of stable Mo complexes during the passivation process, which lowers the chloride ion content[9].

Ilevbare and Burstein[72] suggested that Mo reduces the incidence of both nucleation and metastable pits on stainless steels. Mo can reduce the number of active inclusions due to formation of Mo sulphides, which are more difficult to dissolve. Moreover, insoluble Mo sulphides can reduce the number of nucleation sites since inclusions are constrained from dissolving and exposing bare metal to chloride ions. As dissolution occur, a smaller portion of the metal is in contact with chloride ions since dissolution is minimised. This causes the transition from nucleation to metastable pitting to be more difficult since the number and size of nucleations are less[72].

Newman[73] observed that Mo reduces the dissolution rate in the active region and has a small effect on E_{rep} (provided that passivation is possible) in acidic solutions. The inhibiting effect of Mo was more pronounced in mildly acidic solutions than acidic solutions. Based on thermodynamics and kinetics, the inhibiting agent of Mo are elemental Mo in acidic solution due to the slower reaction rate of Mo to Mo^{6+} compared to iron dissolution. In less acidic solutions or at more oxidising potentials, MoO_2 may form at sufficient rate. Thus, Mo accumulate on the active surface and inhibits active dissolution in a partly oxidised or elemental form[73].

Mo can promote repassivation through forming an insoluble chloride salt layer in the pit bottom[15]. Formation of Mo complexes with chloride ions causes the pH to raise since the concentration of soluble chloride salts decreases and thereby promotes repassivation[9] due to the rise in interfacial potential[70].

3.2 Effect of molybdenum content

Kopliku and Mendez[2] investigated corrosion attacks on AISI 316L (2.00 wt% Mo) and 317LMN (4.25 wt% Mo, 0.13 wt% N) with and without crevice through a laboratory test and field exposures. The laboratory test was performed in a cyclic salt fog environment according to ASTM D5894[74], while the field exposures were in the Gulf of Mexico and Trinidad on offshore platforms. The exact chemical composition is presented in Appendix A Table A1[2].

In the fog chamber 42 g of synthetic seawater per litre was used to produce the salt spray solution and temperature was kept at 25°C. The temperature was increased to 40°C after 22 days since no corrosion comparable to that observed on AISI 316L in service occurred. After 25 days the temperature was increased once more to 45°C for 22 days, resulting in 69 days of exposure. The pit density on AISI 316L and 317LMN was similar in the laboratory exposure, however 317LMN had shallower attacks both in the laboratory and exposure tests. Furthermore, the difference in corrosion resistance was less on the platform in Trinidad compared to in the Gulf of Mexico[2].

Laycock and Newman[36] studied the influence of Mo content and chloride concentration on E_{pit} at room temperature for AISI 316 and 302. The composition of AISI 316 and 302 is nominally identical except for the addition of 2.5 wt% Mo in AISI 316. The experiment was executed by polarising the samples in the anodic direction from -500 mV vs SCE with a scan rate of 1 mV/s until the anodic current exceeded 1 mA/cm². A 0.1-1.0 M de-aerated NaCl solution was used and three measurements were conducted for each test condition. As presented in Fig. 3.1[36], the E_{pit} difference is in the range 70-100 mV at all tested chloride concentrations for these alloys.

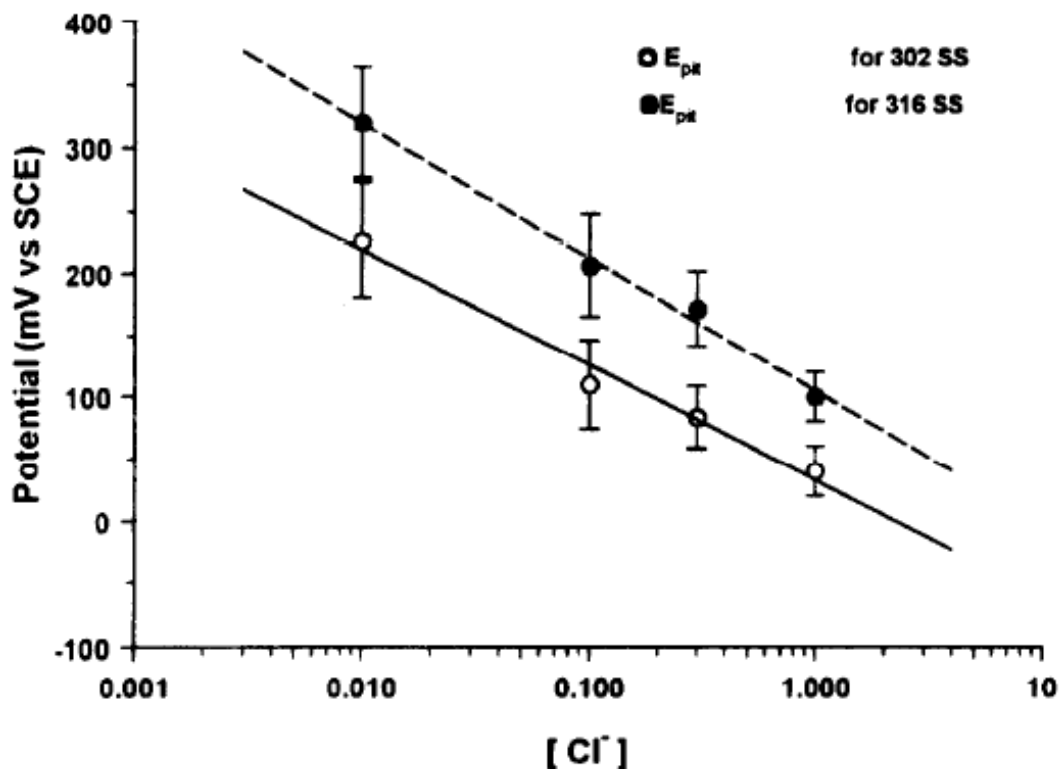


Fig. 3.1: E_{pit} obtained in 0.1-1.0 M de-aerated NaCl for AISI 316 and 302 with different chloride concentrations at room temperature[36].

Upadhyay et al.[70] evaluated the effect of Mo content on pitting corrosion resistance by comparing AISI 316LN, 317LN and 304LN. The chemical composition is presented in Appendix A Table A2. The alloys were subjected to anodic potentiodynamic polarisation in air-saturated 0.01 M FeCl₃ solution at 25°C with a scan rate of 10 mV/min. As seen from Fig. 3.2[70], E_{pit} increases with Mo content. E_{pit} for 304LN, 316LN and 317LN SS is respectively 0.17V, 0.38V and 1.1V vs SCE. A significant increase in E_{pit} with increased Mo content indicate that increased Mo content enhances pitting corrosion resistance and facilitates repassivation of metastable pits[70]. In addition, analysis of current transients was performed to investigate the Mo effect on metastable pitting. The number of current transients and the current transients amplitude decreased with higher Mo content in the alloy. Based on this, the authors suggested that 317LN exhibit improved pitting corrosion resistance compared to 316LN[70].

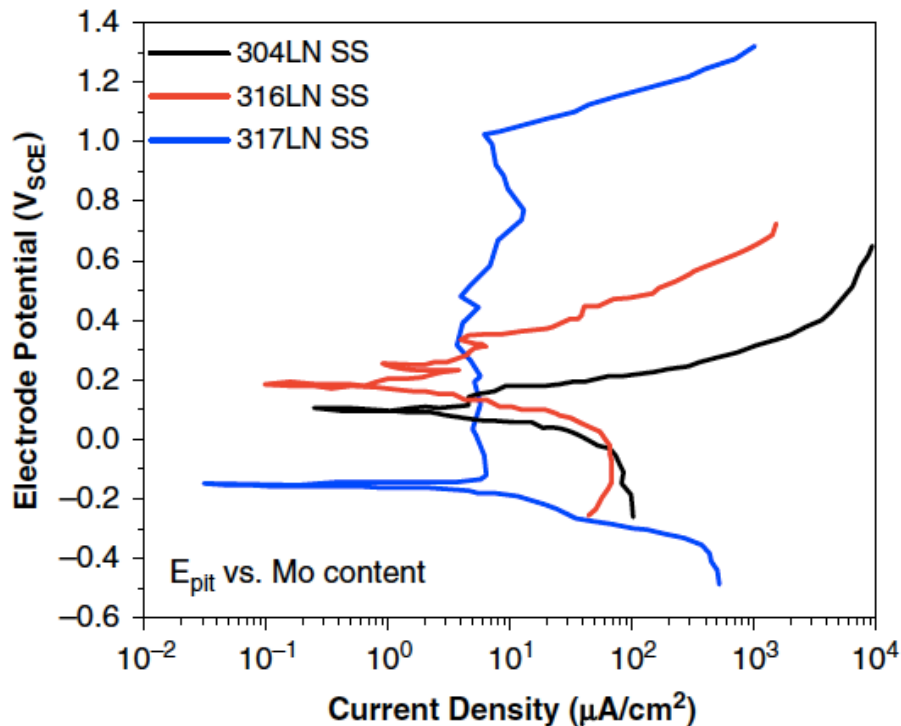


Fig. 3.2: Anodic potentiodynamic polarisation curves for AISI 304LN, 316LN and 317LN in 0.01M FeCl₃ at 25°C with a scan rate of 10 mV/min[70].

Liptakova and Zatkalikova[75] investigated the effect of Mo content by using several AISI 316Ti alloys with Mo content ranging from 2.04-2.88 wt%. The chemical composition is presented in Appendix A Table A3. The electrochemical experiment was conducted in 0.5M NaCl at 23 ± 2°C with scan rate 5 mV/s. Generally PREN and E_{pit} increased with Mo content

as can be seen from Table 3.1[75]. The reference electrode used in the experiment was not specified, but it is most likely SCE due to the E_{pit} values.

Table 3.1: PREN, Mo content and E_{pit} obtained in 0.5M NaCl at $23\pm 2^\circ\text{C}$ for different AISI 316Ti grades[75].

Material	PREN	wt% Mo	E_{pit} (mV vs SCE)
AISI 316Ti A1	23.7	2.12	601
AISI 316Ti A2	23.4	2.04	660
AISI 316Ti A3	24.1	2.23	790
AISI 316Ti A4	26.2	2.88	1173
AISI 316Ti A5	25.6	2.82	863

3.2.1 Synergy between molybdenum and nitrogen

Austenitic stainless steels used for investigating the effect of Mo content can contain small additions of N. Hence, results indicating improved corrosion resistance obtained from these steels may not entirely be due to Mo, but is probably also affected by the N content according to the PREN.

Kamachi and Dayal[76] studied the influence of N addition on the crevice corrosion resistance for AISI 304, 316 and 317 by potentiodynamic anodic polarisation. The experiment was performed at room temperature in a de-aerated 0.5 M NaCl and 0.5 M H_2SO_4 solution. Several AISI 316 and 317 grades with different Mo and N contents were tested in addition to one AISI 304 grade, where the chemical composition is presented in Appendix A Table A4. The potentiodynamic polarisation curves for AISI 316 with different N contents and a comparison of AISI 304 and 316 are presented in Fig. 3.3[76]. As seen from the figure, the passive current density decreases and crevice potential (E_{crev}) increases at higher N content. The E_{crev} for AISI 316 (0.053 wt% N) and 304 (0.086 wt% N) was equivalent as it can be seen from the figure, which indicate that N surpasses the effect of Mo. For AISI 317, E_{crev} appeared to be independent of Mo and N content. Moreover, optical micrographs showed severe and well developed crevice corrosion attacks on AISI 304 and 316, while the attacks on AISI 317 were mild and developed insignificantly[76].

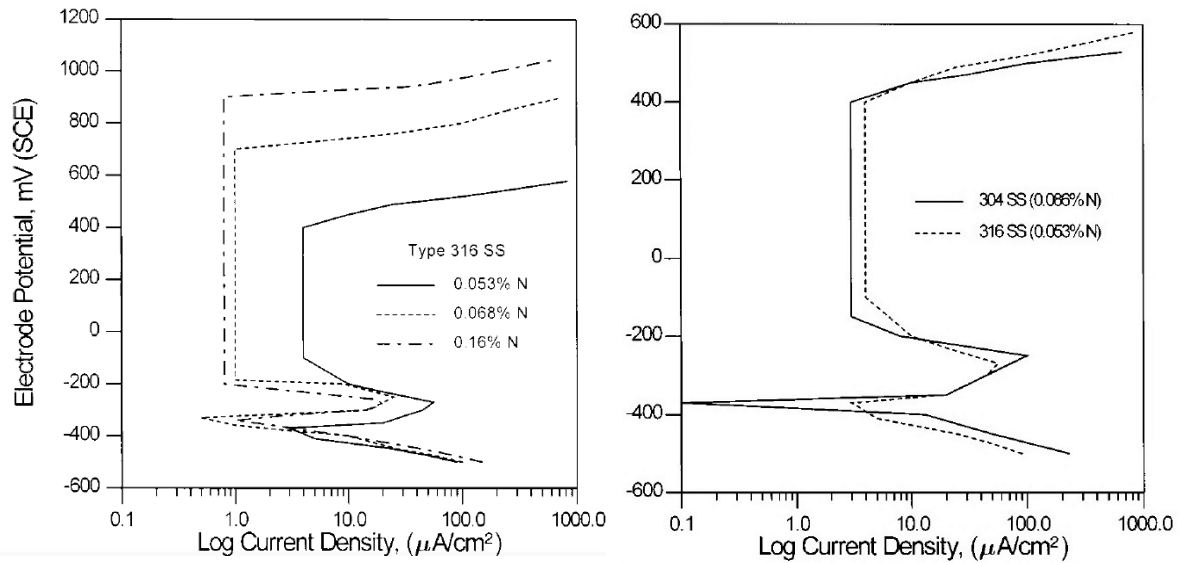


Fig. 3.3: Anodic potentiodynamic polarisation curves of a) AISI 316 with different N content and b) AISI 316 and 304. The curves are obtained at room temperature in a de-aerated 0.5 M NaCl and 0.5 M H₂SO₄ solution [76].

Loable et al.[6] studied the synergetic effect of Mo and N additions by conducting potentiodynamic polarisation and electrochemical impedance spectroscopy (EIS) on four austenitic stainless steels. The austenitic stainless steels tested were the laboratory grades 18Cr-12Ni, 18Cr-12Ni-0.1N, 18Cr-12Ni-3Mo and 18Cr-12Ni-3Mo-0.1N. The exact chemical composition is presented in Appendix A Table A5. Potentiodynamic polarisation was performed in aerated 3.5 wt% NaCl solution at 25°C with different pH by using a scan rate of 1 mV/s, while EIS was conducted at anodic potentials in 3.5 wt% NaCl solution at pH 3.4 and 9.1. In addition, the passive film composition in acidic chloride solutions was characterised by XPS[6].

Among the tested austenitic stainless steels, the main difference in the polarisation curves was E_{pit} , while OCP and the corrosion current density were similar. As presented in Fig. 3.4[6], the effect on E_{pit} was most significant for the alloy containing both Mo and N, and the individual effect of Mo appeared to be larger than N. Furthermore, E_{pit} appeared to be independent of pH except for the Mo and N containing stainless steel[6]. The XPS study of 18Cr-12Ni-3Mo-0.1N showed that the passive film consisted of NH₃ in addition to Cr and Mo oxides, and a small amount of Ni oxides. Through EIS and XPS, Mo was concluded to affect initiation and propagation, while N assist the repassivation process. This was accompanied by a thicker passive film for the Mo and N containing steel that was observed with EIS and XPS[6].

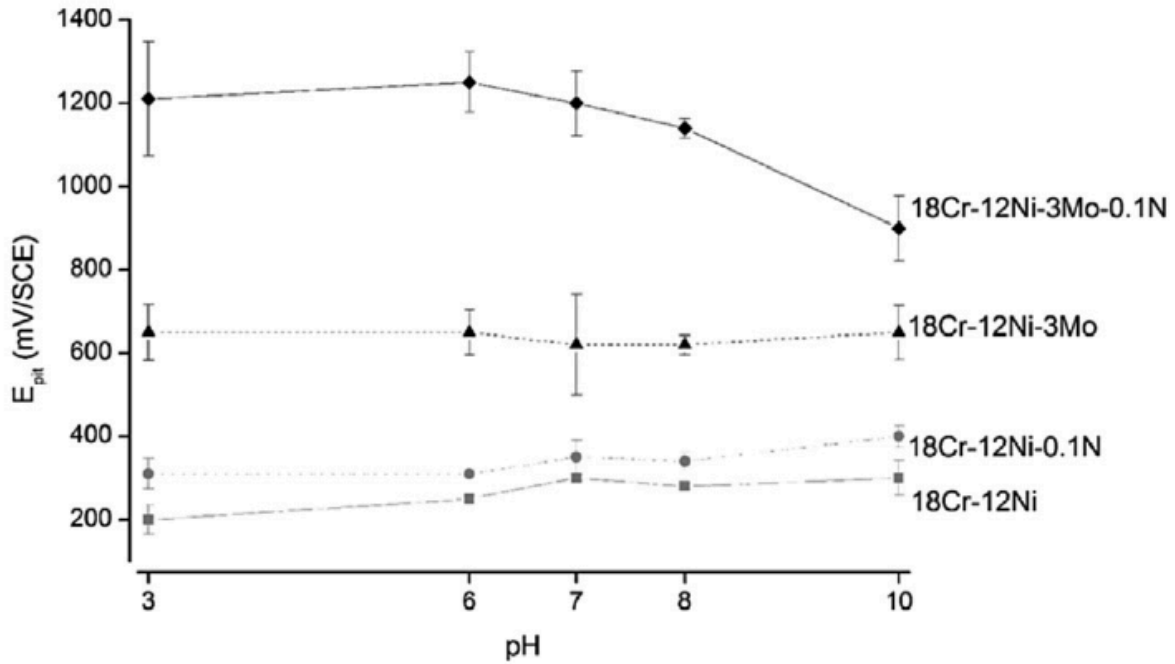


Fig. 3.4: E_{pit} obtained from potentiodynamic polarisation curves in 3.5 wt% NaCl at 25°C with 1 mV/s scan rate for austenitic stainless steels with different Mo and N content as a function of pH[6].

Newman and Shahrabi[77] investigated the effect of N addition in high purity stainless steels based on the AISI 316L composition, which contained 0.02 and 0.22 wt% N. The samples were polarised from -700 mV vs SCE in 1-6M HCl with a scan rate of 1, 8 and 40 mV/s at 21±1°C. For concentrations around 3-4 M, 0.22 wt% N was concluded to significantly affect the anodic dissolution kinetics through surface enrichment of N at high anodic current densities. This is explained by the cathodic dissolution of N to ammonium ions on active surfaces. At sufficient positive potentials the dissolution becomes too slow compared to the increasing rate of alloy dissolution causing N to enrich at the surface and blocking anodic dissolution[77].

3.3 Pit propagation

Heurtault et al.[78] studied the propagation of a single pit on AISI 316L by using a local probe technique. The electrochemical cell consisted of an AISI 316L disc acting as working electrode, a platinum grid as counter electrode and a mercury saturated sulphate electrode (MSE) as reference electrode. To create a pit a glass microcapillary was used to locally supply chloride ions on the steel surface. The experiments were performed in a 0.5M H₂SO₄ solution at 0 V vs MSE (E vs SCE = 650 V vs NHE). Chloride ions were supplied at a constant flow rate of 5.4 μL/h using a 3M NaCl and 0.5M H₂SO₄ solution. A total of 30 experiments at 11 propagation times varying from 45 minutes to 10 hours were performed. The current with time, mean pit depth and radius with time are presented in Fig. 3.5. At the end of each experiment the ratio of pit depth to radius was 0.4. Thus, dish shaped pits were generated. The pit bottom dissolution rate was suggested to be diffusion controlled since the pit depth increased as a function of the square root of time, which is characteristic for a diffusion controlled process[78].

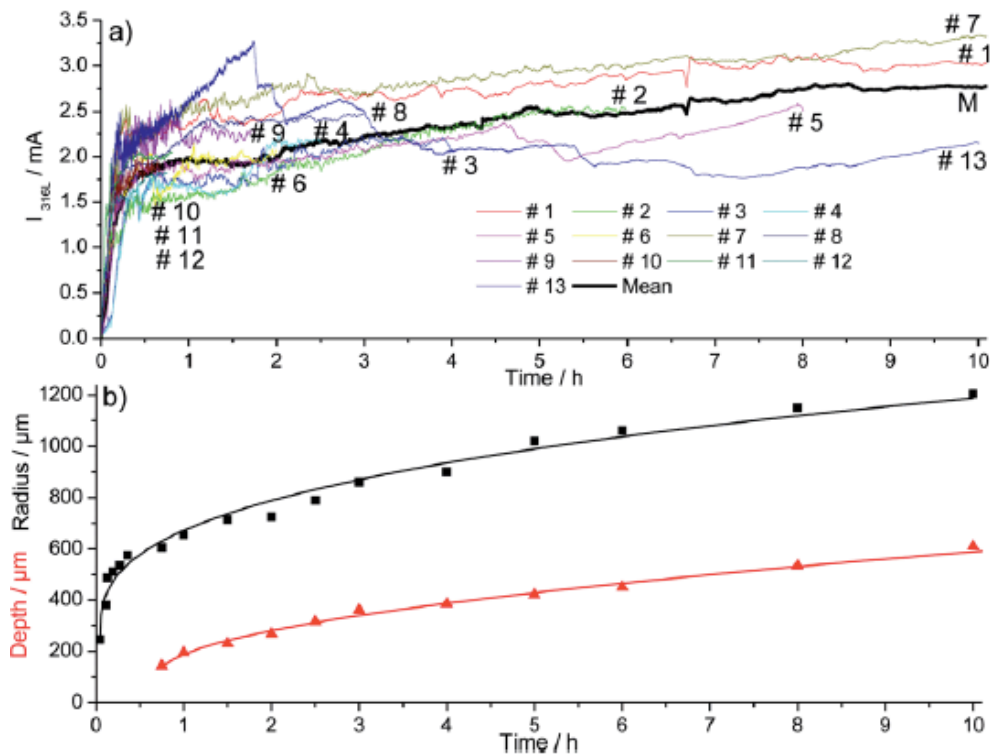


Fig. 3.5: a) Recorded current and b) mean pit depth and radius for AISI 316L as a function of time. The experiments were conducted at 0V_{MSE} in 0.5M H₂SO₄ with locally supply of chloride ions at the pit by using 3M NaCl and 0.5M H₂SO₄[78].

Later Heurtault et al.[43] characterised pit propagation of single pits on AISI 316L at different applied potentials. A similar experimental set up as the authors used in the previous described experiment was used. Several experiments were performed at different applied potentials for one hour in the passive domain ranging from -0.4 to 0.5 V vs MSE. The experiments were conducted at 20°C in 0.5M H₂SO₄ solution while simultaneously injecting 3M NaCl + 0.5M H₂SO₄ solution with the glass microcapillary at a constant flow rate of 5.4 μL/h. The depth remained approximately constant, while the radius increased as a function of applied voltage as presented in Fig. 3.6[43].

Additionally, the pit propagation mechanism was investigated by performing experiments at different constant potentials and at a potential change during pit propagation. For diffusion controlled processes the current density is independent of potential changes, while for ohmic controlled processes the current density varies with potential. The pit depth as a function of time did not significantly depend on applied potential and a potential change during pit propagation, and pit propagation was concluded to be diffusion controlled[43].

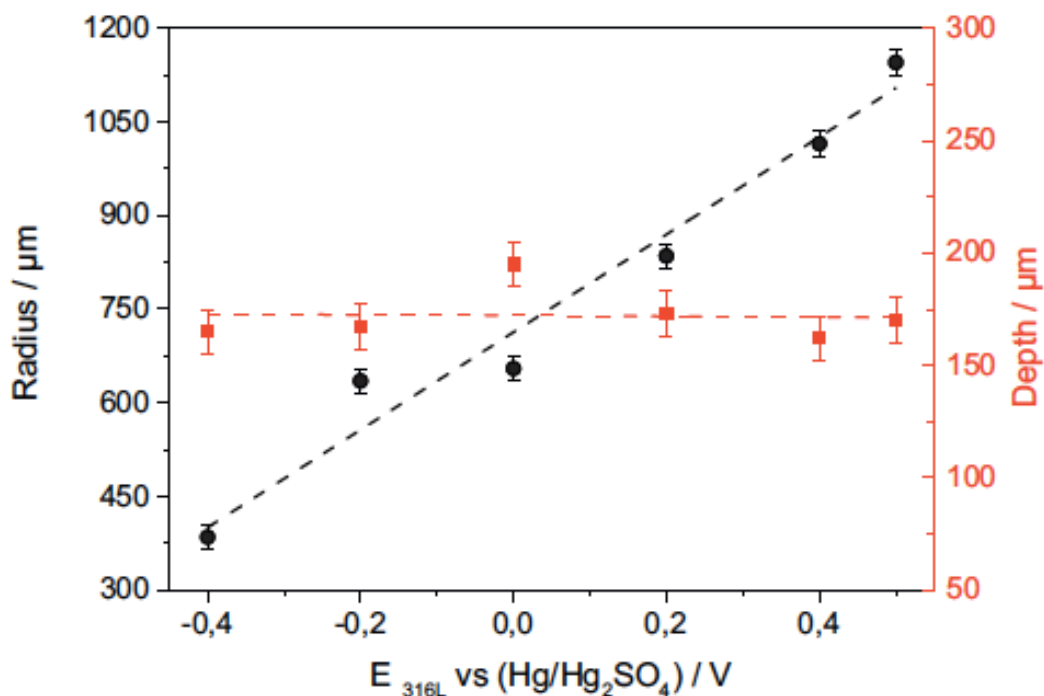


Fig. 3.6: Pit depth and radius of single pits on 316L obtained at different potentials in the passive domain with a 0.5M H₂SO₄ solution while simultaneously injecting 3M NaCl + 0.5M H₂SO₄ solution at 20 °C for one hour[43].

Aouina et al.[79] studied pit propagation on AISI 316L in 0.5M H₂SO₄ solution by using a glass microcapillary to locally inject an aggressive solution. Chloride ions were injected with a 2M NaCl + 0.5M H₂SO₄ solution at a release rate of 10 μL/h at 0 V vs MSE. The current evolution with time generated from the single pit and a SEM image of the pit after three hours propagation is presented in Fig. 3.7[79]. The induction time corresponds to the time from the chloride ion release to the onset of pitting corrosion where chloride ions penetrate the passive film and reach the metal surface. During initiation the current increases progressively for 45 minutes until reaching a threshold value where stable propagation starts.

The pit grew under a cover and a nearly hemispherical shape appeared when the cover was removed as can be seen from Fig. 3.7[79]. The diameter and depth of the pit were 1.4 mm and 405 μm, respectively[79]. Heurtault et al.[43] observed that pits grow under covers for low chloride concentrations (1.2M), while open pits form at high chloride concentrations (3M).

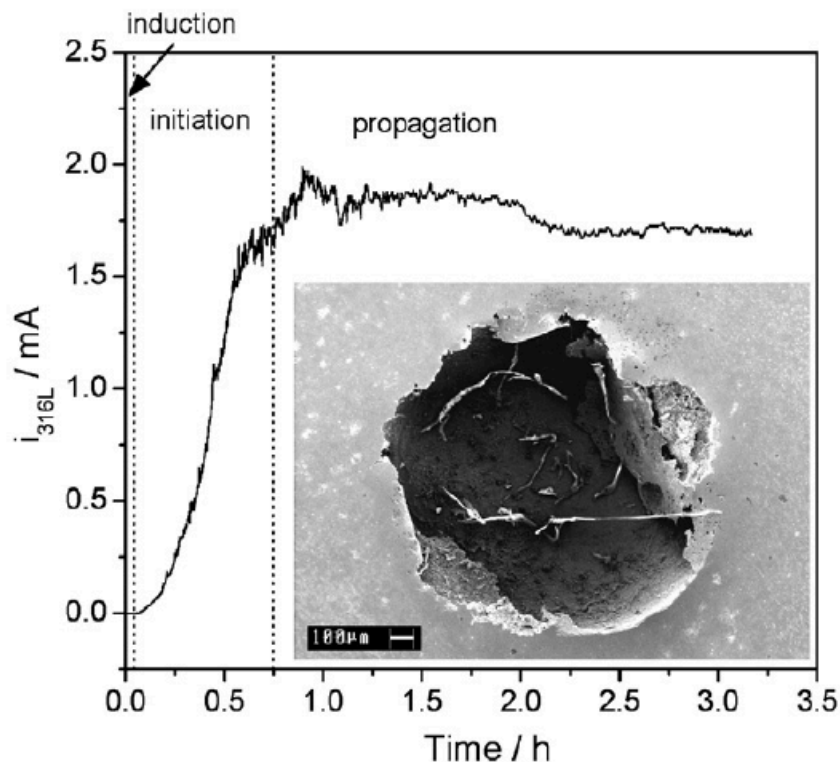


Fig. 3.7: The current with time generated from a single pit on AISI 316L in 0.5M H₂SO₄ while simultaneously injecting a 2M NaCl + 0.5M H₂SO₄, and a SEM photograph of the pit after three hours propagation[79].

4 Experimental work

In the experimental work the objective was to investigate the effect of small changes in Mo content on the corrosion resistance of AISI 316L (UNS S31603), and to study propagation of a single pit with focus on the effect of cathode area and if the pit reaches a limited size due to repassivation.

In the first chapters, the experiments on the effect of Mo content are presented. Several experiments were conducted to obtain a reliable result since the chemical composition of the test materials are similar. The chosen methods to obtain relative corrosion resistance information were anodic cyclic potentiodynamic polarisation (CPP), OCP measurements and exposure in a salt spray chamber. Anodic CPP curves were recorded according to ASTM G61[62] at different test conditions and OCP measurements were conducted at one selected test condition. The exposure in the salt spray chamber was performed according to ASTM B117[80], and anodic CPP of the samples used in this test were performed. The Mo content for AISI 316L is 2.00-3.00 wt% according to ASTM A 312/ A 312M as presented in Table 2.1. Hence, test materials with the lowest accessible differences in Mo content within this range were included in this test program. Additionally, a test material with low Mo content was included.

Propagation of a single pit was studied by an artificial pit experiment developed during this master thesis with different set ups regarding the cathode area. Furthermore, anodic CPP according to ASTM G61[62] and cathodic potentiodynamic polarisation were performed on the stainless steels used in this experiment. These experiments are presented next. After each experiment the sample surfaces were investigated. The approach and different methods used to analyse the surfaces after each experiment are presented in the end.

For the experimental work regarding the effect of Mo content UNS S31603 qualities with different Mo content were used. In this report these are named A-316L and B-316L. In addition, UNS S31703 and UNS S31655 were tested and named 317L and 316 Plus. For the artificial pit experiments, A-316L was used since the chemical composition of this alloy is similar to the UNS S31603 used in the industry. The experiments were performed in the corrosion laboratory at NTNU MTP Gløshaugen.

4.1 Test materials and preparation

The chemical composition of A-316L and the similar grades included in the test program are presented in Table 4.1, and the PREN for each material calculated according to Eq.2.8 are presented in Table 4.2. Material certificates for A-316L, 317L and 316 Plus and the chemical analysis of B-316L delivered with the steel are provided in Appendix B.

Table 4.1: Chemical composition (wt%) of the test materials used in the experimental work.

Material (UNS designation)	C	Mn	P	S	Si	Cr	Ni	Mo	Other
A-316L (UNS S31603)	0.022	1.42	0.031	<0.001	0.32	16.25	10.11	2.03	N:0.07 Cu:0.40 Co:0.38
B-316L (UNS S31603)	0.021	1.573	0.0304	0.0085	0.536	17.322	12.744	2.548	N:0.034 Ti:0.005
317L (UNS S31703)	0.016	1.60	0.026	<0.001	0.32	18.39	14.11	3.06	N:0.06
316 Plus (UNS S31655)	0.020	1.78	0.027	0.001	0.34	20.4	8.4	0.56	N:0.176 Cu:0.29

Table 4.2: Calculated PREN for each test material.

A-316L	B-316L	317L	316 Plus
24.1	26.3	29.4	25.1

A-316L, 317L and pickled 316 Plus were delivered as plates from the manufacturers, while B-316L was delivered as a bolt. The workshop at NTNU prepared two different types of samples by using water jet cutting. Rectangular 316 Plus samples with the size 35x35x3 mm and circular A-316L, 317L and B-316L samples were provided from the workshop as presented in Fig. 4.1. The diameter of the circular samples was 30 mm with 8 mm thickness for A-316L and 317L, and 4 mm thickness for B-316L. Each sample contained a drilled hole, which was necessary for connecting the samples to the circuit with a platinum wire when conducting electrochemical

experiments. The platinum wire was used to connect the samples to the circuit at all electrochemical experiments unless other specified. The drilled hole was either 3 mm or 2 mm for the circular samples, and 3 mm for the rectangular samples. In addition, circular A-316L and 317L samples without a drilled hole were provided for the salt spray chamber experiment.

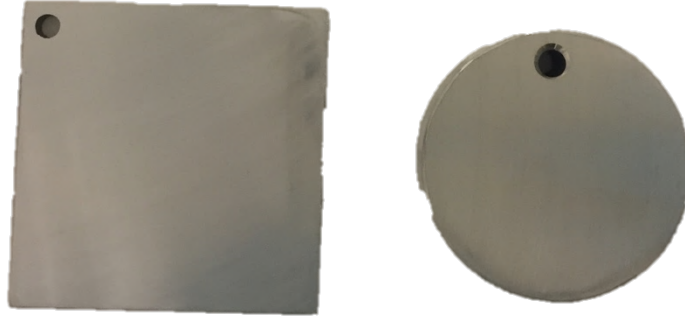


Fig. 4.1: The different sample types provided for the experimental work.

A similar sample preparation procedure was conducted prior to all experiments to obtain similar passive film properties (thickness, crystallization and nature) for each experiment. The samples were prepared by wet grinding with increasingly fine SiC paper, starting at 80-grit and ending at 500-grit. Changing to finer SiC paper was done when all the surface grinding lines were aligned in the same direction and the surface was sufficient smooth. Between each SiC paper used, the samples were cleaned with distilled water to avoid contamination of grinding particles when proceeding grinding. The grinding machine Rotpol-2 was used. As grinding was completed, the samples were cleaned with distilled water and stored in air one night before use to make sure the passive film was restored. Before use the samples were ultrasonically degreased for 5 min, thoroughly rinsed with acetone and distilled water before drying.

To obtain the current density the area of the circular and rectangular samples was calculated prior to conducting the experiments according to Eq.4.1. and Eq.4.2, respectively.

$$A_{\text{circular sample}} = 2\pi r_1(r_1 + h) - 2\pi r_2^2 \quad (4.1)$$

$$A_{\text{rectangular sample}} = 2wl + 2lh + 2wh - 2\pi r_2^2 \quad (4.2)$$

Where r_1 is the sample radius, h is the height and r_2 is the radius of the drilled hole, and w and l for the rectangular samples are the width and length.

4.2 Anodic cyclic potentiodynamic polarisation

The effect of molybdenum content on the relative difference in corrosion properties was investigated by recording anodic CPP curves according to ASTM G61[62] to obtain the parameters OCP, E_{pit} , E_{rep} and i_{pass} . These parameters can be used to compare the corrosion properties of the test materials. The anodic CPP curves were recorded at different test conditions to analyse the effect of temperature and chloride concentration, and to determine if differences in the corrosion properties among the test materials are dependent on these parameters.

Electrolytes of 3 and 5 wt% NaCl at both $20\pm 2^\circ\text{C}$ (RT) and $35\pm 2^\circ\text{C}$ were selected as test conditions as presented in Table 4.3. These electrolytes were selected since 3 wt% NaCl is approximately the chloride concentration in seawater, while 5 wt% represents accumulation of chlorides which can occur at marine atmospheric conditions. To obtain 3 and 5 wt% NaCl solutions respectively 30 and 50 g NaCl were dissolved in 1 L distilled water by stirring at ambient temperature.

Table 4.3: The different test conditions used to record anodic CPP curves.

Test condition	NaCl concentration	Temperature
1	3 wt%	RT
2	3 wt%	$35 \pm 2^\circ\text{C}$
3	5 wt%	RT
4	5 wt%	$35 \pm 2^\circ\text{C}$

To record the curves a Gamry Interface 1000 potentiostat was used. Before use the potentiostat was calibrated by the use of an EIS Dummy Cell since the instrument was supposed to be calibrated every six months or after longer periods without using it.

4.2.1 Experimental procedure

The test cell used for anodic CPP is schematic illustrated in Fig. 4.2. The test materials served as working electrode (WE), a platinum mesh served as counter electrode (CE) and an Ag/AgCl electrode saturated with KCl was used as reference electrode (RE). The reference electrode was connected to the bulk solution by a salt bridge, which permits the reference electrode to remain at room temperature for the tests at $35\pm 2^\circ\text{C}$. Oxygen was removed from the electrolyte by purging with high purity nitrogen gas (N_2) through a house. For the tests at $35\pm 2^\circ\text{C}$ a heating plate with a power regulator that controls the temperature was used.

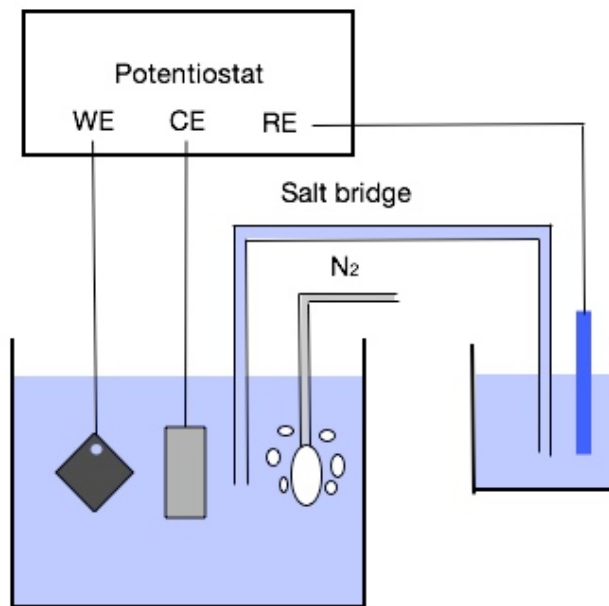


Fig. 4.2: Schematic illustration of the test cell used to record anodic CPP curves.

The test cell was assembled with the specimen kept above solution level and all openings were covered to avoid oxygen ingress. The solution was then purged with nitrogen gas minimum one hour while simultaneously heating the solution for the tests at $35\pm 2^\circ\text{C}$. After one hour the specimen was immersed and OCP recorded minimum one hour until stabilised before the potential scan started. Purging with nitrogen gas continued throughout the test to secure minimal amount of dissolved oxygen in the electrolyte.

The potential scan started at -150 mV vs OCP and was scanned in the anodic direction until the current reached 5 mA where the scan was reversed. A constant scan rate of 0.1667 mV/s was employed, and the reversed scan was continued until the hysteresis loop closed or OCP was reached. Correspondingly, the OCP, E_{pit} , E_{rep} and i_{pass} were obtained from the curves. At first

two scans at each test condition for each material were executed, however since the curves appeared to be essentially similar one scan for each test condition was performed.

The experimental set up during recording anodic CPP in 3 wt% NaCl at 35°C for A-316L is presented in Fig. 4.3. As can be seen from the figure, a green corrosion product is present in the beaker. The green corrosion product was observed for all test materials at each test condition.

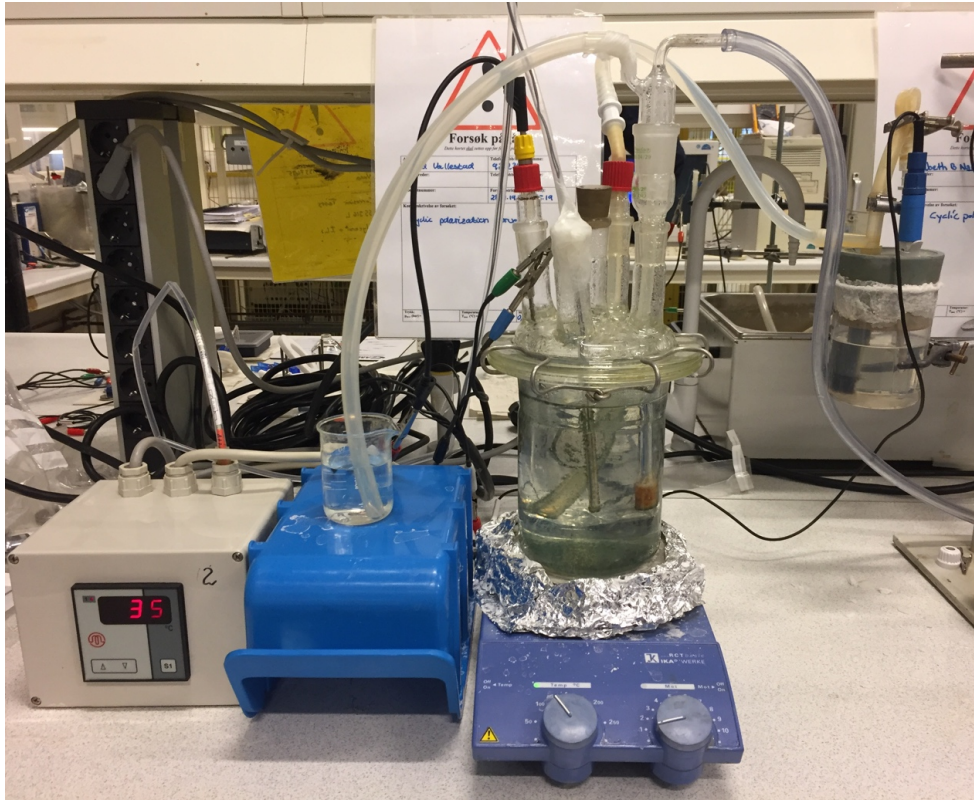


Fig. 4.3: The experimental set up used to record anodic CPP curves.

4.3 Open circuit potential measurements

The purpose of conducting OCP measurements is to investigate the susceptibility to pitting corrosion under normal operating conditions where dissolved oxygen is present in the electrolyte. This can be accomplished by evaluating the measured OCP at specific test conditions and comparing the measurements with measured E_{pit} and E_{rep} from the anodic CPP curves at equal test conditions. For this investigation a 5 wt% NaCl solution at 35 ± 2 °C was chosen as test condition. The 5 wt% NaCl solution represents chloride accumulation which can be an issue in marine atmospheric conditions.

4.3.1 Experimental procedure

A schematic illustration of the test set up used to conduct OCP measurements are provided in Fig. 4.4, and an overview of the experimental set up is presented in Fig. 4.5. This experiment was conducted by immersing the samples in the solution after preheating the solution to $35^{\circ}\text{C} \pm 2^{\circ}\text{C}$. The OCP of each sample was then measured immediately after immersing the samples and recorded for the entire test duration by using logging channels. As for the anodic CPP, the reference cell was connected to the bulk solution with a salt bridge. However, to ensure ionic contact a cotton rod was additionally used in the salt bridge. The heating plate and temperature regulator ensured to retain the temperature at $35^{\circ}\text{C} \pm 2^{\circ}\text{C}$ for the test duration.

Oxygen purging was conducted the last three days to investigate if the amount dissolved oxygen was below the saturation. Furthermore, the heating plate was turned off the last two days due to noise on the curves that was suspected to be caused by metastable pitting.

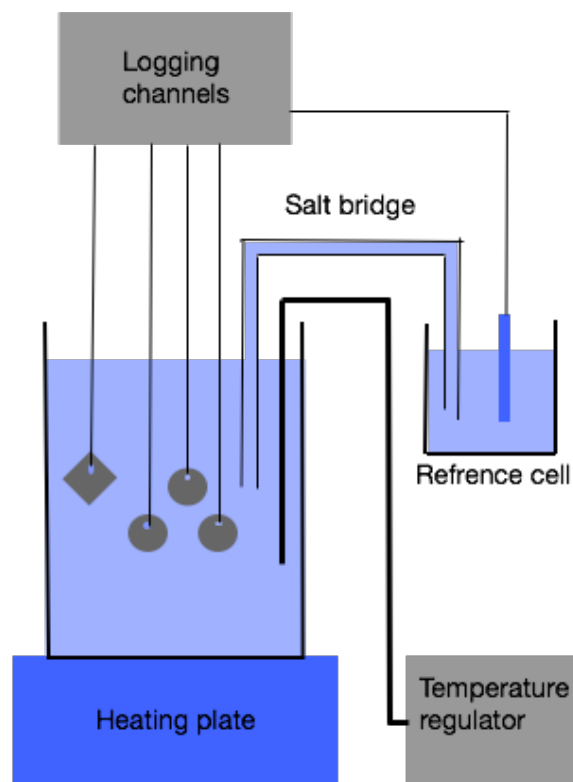


Fig. 4.4: Schematic illustration of the test set up used to conduct OCP measurements.

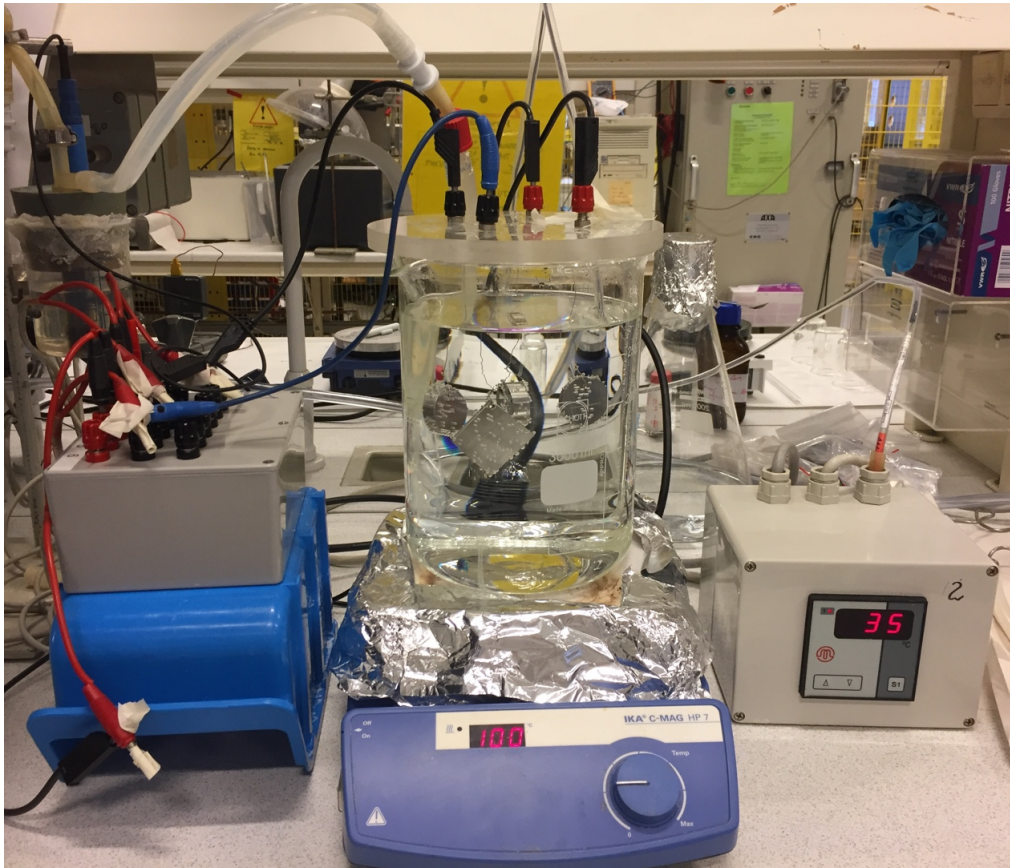


Fig. 4.5: The experimental set up used to conduct OCP measurements.

4.4 Salt spray test

The purpose of conducting a salt spray test was to investigate the effect of Mo in simulated marine atmosphere, where the focus was to investigate the weight loss and the visual appearance. Since the test materials is evaluated with respect to pitting corrosion when conducting anodic CPP and OCP measurements, a crevice was simulated on the samples for the salt spray test to include the difference in relative crevice corrosion of the test materials. The salt spray exposure was performed according to ASTM B117[80] to simulate marine atmosphere.

To obtain corrosion attacks during the exposure and to obtain a similar test condition as for the anodic CPP and OCP measurements, the salt spray solution used was 5 wt % NaCl and the salt spray chamber temperature was kept at 35°C. At this test condition at least A-316L and B-316L are expected to exhibit corrosion attacks based on a study done by Lv et al.[31], where pitting corrosion occurred on AISI 316L at similar temperature and NaCl concentration.

Anodic CPP curves of A-316L, B-316L, 317L and 316 Plus samples with a simulated crevice were additionally recorded according to the experimental procedure described in chapter 4.2.1. The purpose was to obtain OCP, E_{crev} , E_{rep} and i_{pass} since the samples contained a simulated crevice which can affect these parameters. Since the solution and temperature used in the salt spray chamber was 5 wt % NaCl at 35°C, the anodic CPP curves was recorded at this test condition.

4.4.1 Sample preparation

The samples were coated with Jotamastic 87[81] to simulate a crevice on the surface, which is a two-component epoxy mastic coating. The coating was prepared by mixing 12 ml Jotamastic 87 STD038 Grey with 2 ml Jotamastic 87 STD comp B. By using a pencil, a circular area of approximately 10 mm diameter on each sample was coated as presented in Fig. 4.6. The coating was then dried for two days before use. Four samples of each material quality were used for the salt spray test, while the fifth was for recording the anodic CPP curves.



Fig. 4.6: The samples prepared prior to the salt spray exposure and anodic CPP.

Each sample was weighted and marked on the backside before the salt spray test with a scribe needle to obtain control of material type and sample number. Marking the samples with a scribe needle can be an initiation site for pitting corrosion. The sample weight prior to the salt spray exposure is presented in Table 4.4.

Table 4.4: The weight (g) of the coated samples prior to the salt spray test.

Sample number	A-316L	317L	316 Plus	B-316L
1	44.3205	43.7705	28.1177	22.5941
2	44.6149	43.7603	28.5811	22.5059
3	44.8038	44.3651	28.4831	22.1468
4	44.2187	44.4970	28.5100	22.2419

4.4.2 Experimental procedure

The salt spray exposure was conducted in the salt spray chamber Ascott S1000 ip where the temperature was kept at 35 ± 2 °C. In a salt solution reservoir outside the chamber 5 wt% NaCl solution was prepared, and the solution was supplied to the salt spray chamber through a house. Spraying of solution was conducted continuous for the duration of the entire test period, except for short periods when the samples were inspected. First the chamber was opened after three days and later once a week to examine the samples for corrosion attacks.

The samples were placed in the salt spray chamber as demonstrated in Fig. 4.7, and to avoid water collecting beneath the samples they were placed on a polymer rod. After three days a 1-2 mm thick water layer covered the sample surface. This thickness is more similar to immersed conditions than marine atmosphere, hence three samples were slightly tilted to avoid the water layer on the surface. The fourth was not tilted in order to investigate the thick water layer effect.



Fig. 4.7: The samples placed in the salt spray chamber.

Due to absence of corrosion attacks during the test period some modifications were made. After 27 days crevice corrosion was visually observed on one A-316L sample, which indicate that the coating did not simulate a sufficient crevice to obtain crevice corrosion attacks. Since corrosion did not occur on several samples, mineral wool was placed on two of the tilted samples to create a less adherent crevice that may cause a higher probability of crevice corrosion attacks as presented in Fig. 4.8. 316 Plus slipped off the polymer rod during this test period. The surface roughness was suspected to be too smooth causing fewer corrosion initiation sites. To investigate if the smooth surface roughness caused lack of corrosion attacks not grinded A-316L, B-316L and 317L samples without coating were placed in the salt spray chamber after 31 days. 316 Plus samples were not included since these samples were delivered pickled. The samples were exposed 67 days in the salt spray chamber.



Fig. 4.8: The samples after 27 days in the salt spray chamber. Mineral wool was placed on selected samples and A-316L showed corrosion attack.

When the salt spray test was completed the samples were carefully removed from the salt spray chamber and cleaned with distilled water at ambient temperature to remove salt deposits and corrosion products. The samples were examined visually and weighted two times before the coating was removed cautiously with a scalpel on the samples where it was possible.

4.5 Artificial pit experiments

The purpose of developing and conducting artificial pit experiments was to study propagation of a single pit and investigate the effect of cathode area. Regarding pit propagation, the main purpose was to investigate if a pit reaches a limited pit size due to repassivation. Both potential and current measurements are of great importance when evaluating pit propagation and the effect of cathode area. Hence, the main goal with the artificial pit experiment was to obtain these parameters for a single pit.

The artificial pit experiment was developed by considering the solution chemistry evolving within propagating pits and creating a sample preparation method to obtain A-316L samples with a single pit. During pit propagation at marine atmospheric conditions the solution chemistry developing within the anodic dissolving pit has a low pH, and the thin water moisture layer surrounding the pit represents the cathode area has a higher pH. The approach for simulating the chemistry developing inside the pit and including the effect of cathode area is described below.

Conducting experiments by immersing or covering the entire sample surface with a chloride containing electrolyte gives the rise to several pits on the surface. Thus, the measured current and potential are not from a single pit. To solve this issue samples with an artificial pit was made by drilling a hole through the coating on A-316L samples.

Since the electrolyte developing within a pit has a low pH, a 6 wt% FeCl_3 solution was decided to be used as test solution. This solution simulates a condition where both the anode and cathode reaction can occur inside the artificial pit due to the low pH. Normally the cathode reactions are outside the pit as well. To simulate a cathode area outside the pit, the artificial pit can be connected to an external cathode. Since covering the pit with a thin film electrolyte caused challenges with connecting the pit to an external cathode, the experiments were performed immersed.

The purpose of coupling the artificial pit to an external cathode is to obtain the coupling potential and the galvanic current development from a single propagating pit, which can be used to determine if the pit repassivates. By using different sized external cathode areas, the effect of cathode area can be included. Since A-316L is expected to be susceptible to corrosion in 6 wt% FeCl_3 , a UNS S31254 (6Mo) sample was used as external cathode since 6Mo is more

corrosion resistant than A-316L. The higher corrosion resistance for 6Mo compared to A-316L can be seen from the material certificates in Appendix B, where 6Mo is alloyed with a higher amount of Cr, Mo and Ni. This coupling creates a galvanic coupling as presented in Fig. 2.6[40], where the current flows from the A-316L artificial pit to the 6Mo sample.

One of the samples connected to an external cathode and the freely exposed sample was placed in 5 wt% NaCl after exposure in 6 wt% FeCl₃ to examine if the pit repassivates or continue to propagate as the potential outside the pit changes. Furthermore, the electrolyte at the cathode area normally consist of a thin NaCl moisture layer, which may cause a different cathodic efficiency compared to the 6 wt% FeCl₃ solution used in this experiment. To compare the cathodic efficacy in 5 wt% NaCl with 6 wt% FeCl₃, cathodic potentiodynamic polarisation of the 6Mo sample was conducted in both 5 wt% NaCl and 6 wt% FeCl₃.

In the following chapters the experimental procedure for the artificial pit experiments and cathodic potentiodynamic polarisation of the 6Mo samples that were performed to obtain cathodic curves for 6 Mo, will be described. Additionally, anodic CPP of A-316L according to the experimental procedure described in chapter 4.2.1 was conducted to obtain polarisation properties of A-316L in 6 wt% FeCl₃. The experiments presented in this chapter were performed at RT.

4.5.1 Sample preparation

Experiments with artificial pits require that only the artificial pit on the sample is exposed to the solution. Therefore, a coated AISI 316L rod with threads on the end was used as sample holder. On the lateral edge of each sample a threaded hole was prepared by the workshop at NTNU to fasten the rod. The samples were screwed on the rod and coated with Jotamastic 87[81], which was prepared as described in chapter 4.4.1. Three coating layers were applied to ensure that no other parts of the sample than the artificial pit did come in contact with the electrolyte. After each layer the samples were dried for two days. An artificial pit was made on each sample by drilling a small hole of 2 mm diameter and approximately 0.5 mm depth below the coating as presented in Fig. 4.9. This gives an artificial pit surface area of 0.05 cm^2 .

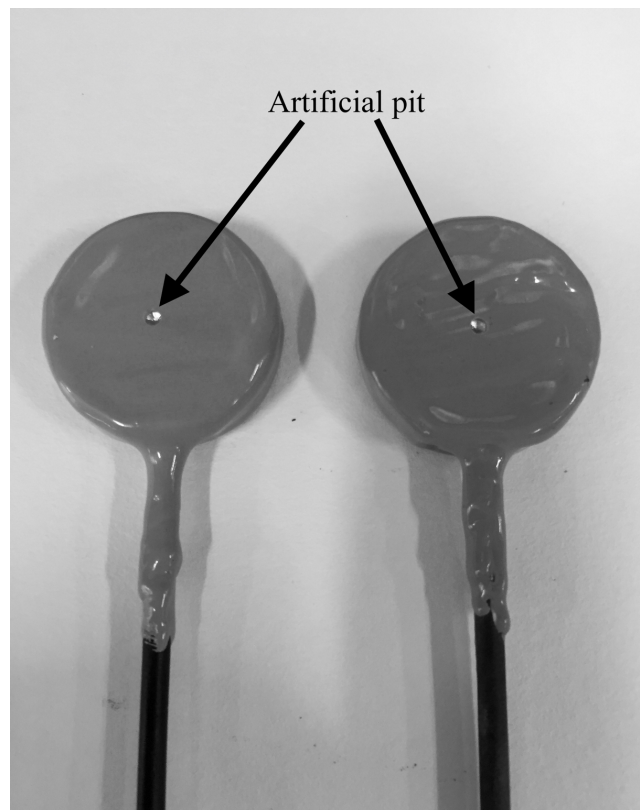


Fig. 4.9: The samples prepared prior to the artificial pit experiments.

Pickled rectangular 6Mo samples with 40 mm length, 40 mm width and 3 mm thickness were provided. The rectangular samples were used as received for all experiments, except for one that were cut to the size 15 mm length and width with the cutting machine Accutom-50. The surface area of the large 6Mo sample was 36.8 cm^2 , while the small sample was 6.30 cm^2 . Before use the 6 Mo samples were ultrasonically degreased for 5 min, and thoroughly rinsed with acetone and distilled water before drying.

4.5.2 Experimental procedure

The artificial pit experiments was performed with three different experimental set ups for the cathode area. Two samples were connected to a 6Mo sample that served as cathode, while one sample was freely exposed. Due to limited space in one beaker, the samples were exposed in two beakers. The different experimental set ups are listed in Table 4.5.

The electrolyte was prepared by dissolving 100 g of $\text{FeCl}_3 \cdot 6\text{H}_2\text{O}$ in 900 mL distilled water, as described in ASTM G48[52], giving a total of about 6 wt% FeCl_3 . For this electrolyte the measured pH was 1.23 at 22.5°C, obtained with the instrument PHM220 Lab pH Meter.

Table 4.5: The experimental set ups for the artificial pit experiments.

Experimental set up	Sample	Surface area of 6Mo sample (cm²)	Beaker
A-316L connected to 6Mo	1	36.8	1
A-316L connected to 6Mo	2	6.30	2
A-316L freely exposed	3	-	1

An illustration of the experimental test set up is provided in Fig. 4.10, which demonstrates the approach to obtain the galvanic current from the artificial pit sample to the 6Mo sample. In this experiment, the artificial pit served as anode and the 6Mo sample served as cathode. The reference cell was connected to the bulk solution by a salt bridge with a cotton rod to ensure ionic contact if bubbles collected in the salt bridge, and the 6Mo sample was connected to the circuit with a platinum wire. Additionally, the experimental set up for beaker 1 is presented in Fig. 4.11.

The samples were immersed and the potential was recorded by using logging channels. Sample 1 and 2 were then connected to the 6Mo sample to obtain the galvanic current flowing from the pit to the external cathode area. To obtain the galvanic current a resistance of 1Ω was mounted between the artificial pit and 6Mo samples. Thus, the potential drop was measured, and the galvanic current was obtained by using ohms law. The potential on each sample and the galvanic current were recorded throughout the experiment. The measured potential when the samples was connected to 6Mo is the coupling potential. As can be seen from Fig. 2.6[40], the measured coupling potential is at the pit opening.

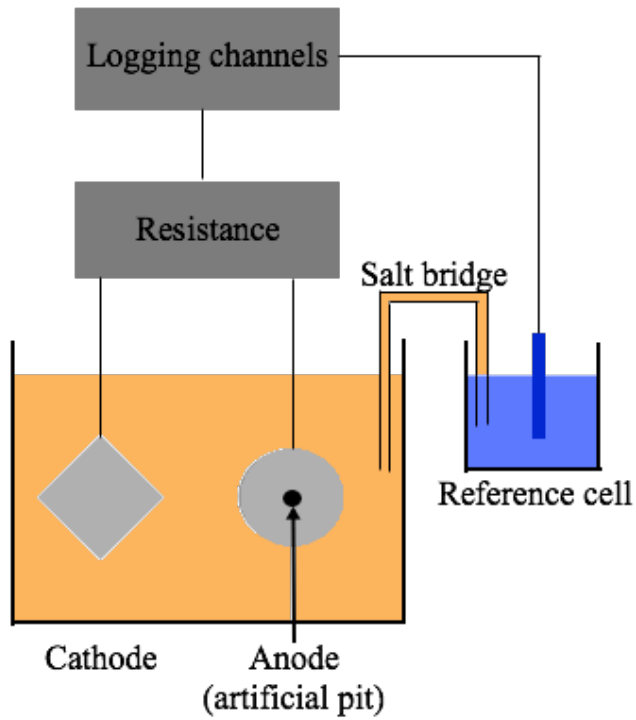


Fig. 4.10: Schematic illustration of the test set up where a A-316L sample with an artificial pit is connected to the 6Mo external cathode.

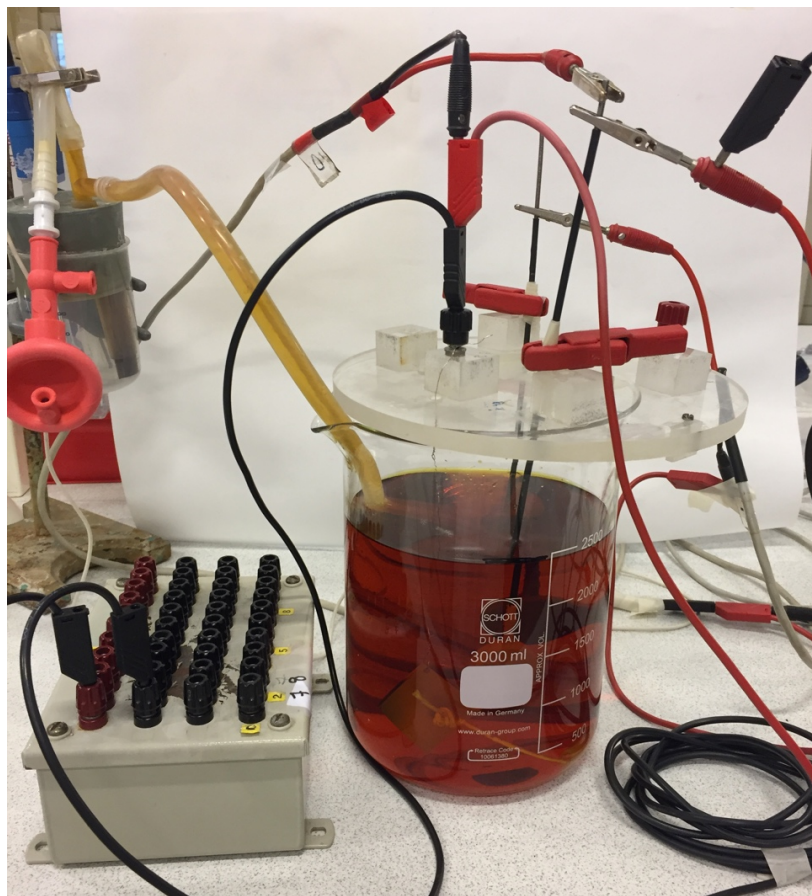


Fig. 4.11: The experimental set up for the beaker containing the artificial pit sample connected to 6Mo with a surface area of 36.8 cm^2 and the freely exposed artificial pit sample.

The samples were exposed in beaker 1 for 26 days before the electrolyte was changed to a 5 wt% NaCl solution. Changing the electrolyte was performed by lifting the glass plate and replacing the beaker containing 6 wt% FeCl₃ solution with a beaker containing 5 wt% NaCl solution. To avoid excessive FeCl₃ in the new solution the reference cell and salt bridge were changed. The sample in beaker 2 was exposed for 15 days in 6 wt% FeCl₃. The coating was removed carefully with a scalpel after the experiments, and the samples were rinsed with distilled water and ethanol.

4.5.3 Cathodic potentiodynamic polarisation

Cathodic potentiodynamic polarisation was performed with the 6Mo sample in 5 wt% NaCl and 6 wt% FeCl₃ at RT. The experimental test set up used for both electrolytes is presented in Fig. 4.12. The experimental set up was similar to the set up used for recording anodic CPP curves presented in chapter 4.2.1, however the cathodic potentiodynamic polarisation curves were conducted in an oxygen containing solution. Thus, nitrogen purging was not performed, and the test was started by immersing the samples and recording OCP for one hour. The potential scan started at +0.10 V vs OCP and the sample was polarised in the cathodic direction to -1.0 V vs OCP.

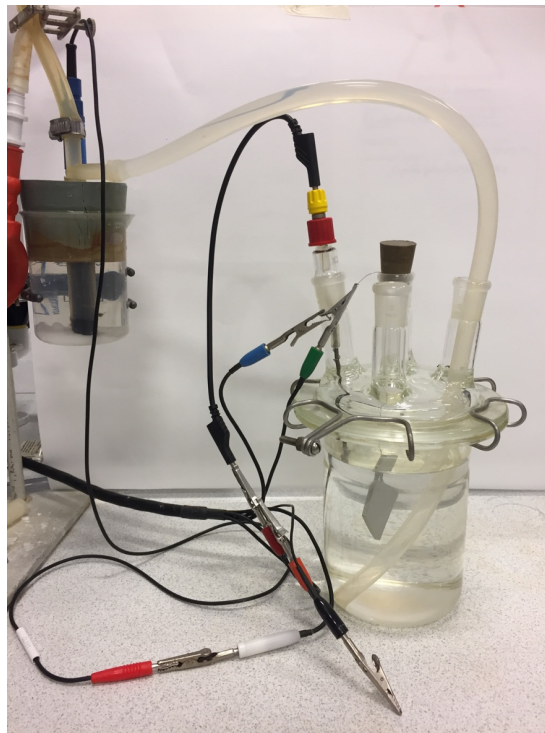


Fig. 4.12: The experimental set up used to conduct cathodic potentiodynamic polarisation for the 6Mo sample in 5 wt% NaCl and 6 wt% FeCl₃.

4.6 Surface characterisation

The sample surfaces after the electrochemical measurements and exposure in the salt spray chamber were characterised by optical microscopy. All surface characterisations by optical microscopy were achieved with a Alicona InfiniteFocus 3D Microscope (IFM)[82]. Observations in IFM that needed further investigation were additionally analysed with scanning electron microscopy (SEM) and energy dispersive spectroscopy (EDS) point analyse. The SEM used was a FEI Quanta FEG 650 Environmental SEM. Before investigating the surfaces, the samples were thoroughly rinsed with distilled water and ethanol.

Pit depth, diameter and density can be used to compare the difference in corrosion attacks between the test materials. IFM was used to obtain these parameters after anodic CPP and OCP measurements. Examples on how the pit depth and diameter were measured are demonstrated in Fig. 4.13 and Fig. 4.14, respectively.

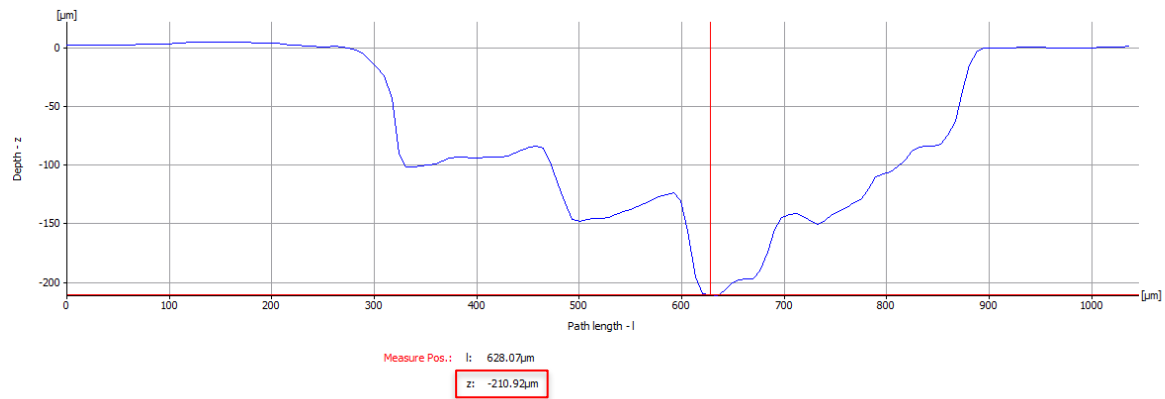


Fig. 4.13: Example of a pit depth (z) measurement obtained by IFM.

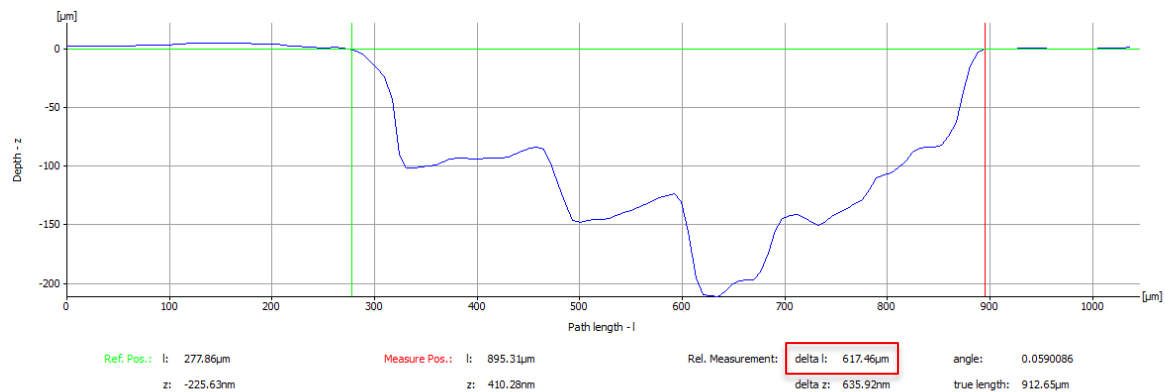


Fig. 4.14: Example of a pit diameter (ΔI) measurement obtained by IFM.

The samples subjected to anodic CPP in 5 wt% NaCl at 35°C were chosen for the IFM investigation since by visual inspection these samples contained the largest attacks compared to the samples subjected to anodic CPP at the other test condition. Furthermore, the surface on each sample that contained most severe attacks were chosen to analyse. The pit depth, diameter and density were additionally used for the anodic CPP samples to quantitatively evaluate the extent of pitting corrosion with standard charts as described in ASTM G46[68] to obtain a ranking number.

Each sample were investigated with IFM after the OCP measurements. Since 316 Plus exhibited indications of metastable pitting during the OCP measurement, 316 Plus was additionally investigated in SEM. Pits on B-316L were surrounded by a brown and blue coloured area. These pits were investigated with EDS point analyse to obtain information about the elements present at these spots and the surrounding bulk area. Furthermore, a statistical analysis by using a box and whiskers chart[83] were performed with the data obtained from the EDS point analyse to investigate if the elements in the spots differs from the bulk surface. The boxes represent the range where the majority of the data points lies within, and the range is a measure of the data spread. The whiskers in the chart are two lines outside the box that represent the highest and lowest values of the dataset. Inside the box is a line that represents the median of the dataset.

The topography of the sample surfaces, the actual volume loss and geometrical parameters of the pits were obtained with IFM after the artificial experiment. The actual volume loss of the samples was found by obtaining a 3D photograph of the samples such that volume loss was provided by the IFM software. Additionally, the volume loss of the samples was calculated according to Eq.2.7, which can be compared to the actual volume loss. Last, the surface of A-316L after anodic CPP in FeCl₃ at RT was investigated with IFM.

5 Results

This chapter presents the results from the experimental work in four parts. The first three parts are dedicated to the experimental work conducted to investigate the effect of small changes Mo content, where the test materials A-316L, B-316L, 317L and 316 Plus were included in the test program. The anodic CPP curves according to the test matrix given in Table 4.3 are presented first, and the OCP measurements are presented after. In the third part, the result from the salt spray chamber exposure of samples with a simulated crevice and the anodic CPP curves of these samples are presented. In the last part the results from the artificial pit experiments performed with A-316L as artificial pit sample are presented. In this part, cathodic potentiodynamic polarisation of 6Mo and anodic CPP of A-316L are presented as well. After the results of each experiment are presented, the corresponding surface characterisation is presented. All potential values refer to an Ag/AgCl electrode saturated with KCl.

5.1 Anodic cyclic potentiodynamic polarisation

Anodic CPP curves were recorded to investigate the effect of Mo content on the relative susceptibility to pitting corrosion for the test materials A-316L, B-316L, 317L and 316 Plus. This section presents the anodic CPP curves obtained according to ASTM G61[62] conducted in 3 and 5 wt% NaCl at RT and 35°C.

The anodic CPP curves for A-316L, B-316L, 317L and 316 Plus at the different test conditions are presented in Fig. 5.1-Fig. 5.4, and the corresponding OCP, E_{pit} , E_{rep} and i_{pass} obtained from the curves are presented in Table 5.1-Table 5.4. Additionally, the calculated PSF according to Eq. 2.9 at each test condition is presented. At all test conditions the anodic CPP curves for each test material contained a hysteresis loop.

The potential at which metastable pitting starts according to the anodic CPP curves are presented in Table 5.5. Current transients were observed below E_{rep} on some of the curves. Since metastable pitting occurs between E_{rep} and E_{pit} , metastable pitting in this case is assumed to start at E_{rep} . As it can be seen from Fig. 5.1-Fig. 5.4, the magnitude of the current transients varies among test material and test condition. Metastable pitting appeared not to occur on B-316L since E_{pit} and E_{rep} are similar.

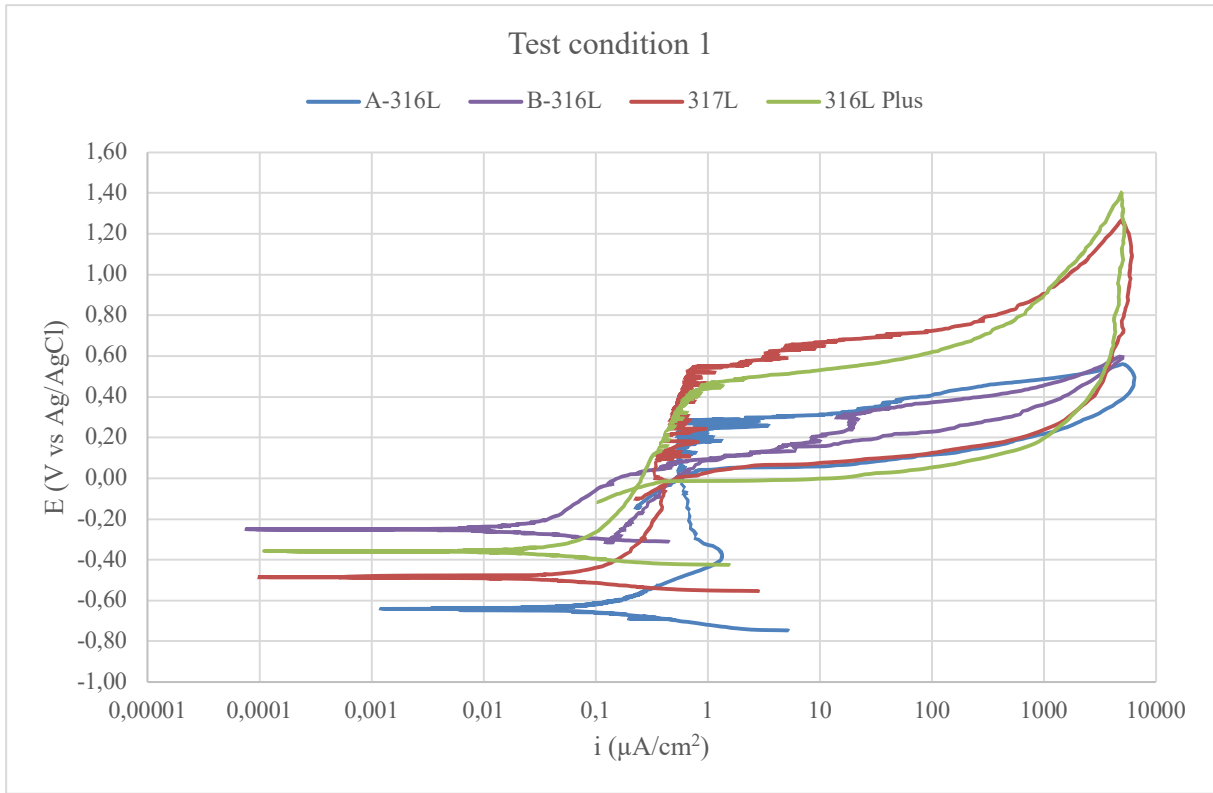


Fig. 5.1 Anodic CPP curves for A-316L, B-316L, 317L and 316 Plus obtained in 3 wt% NaCl at RT.

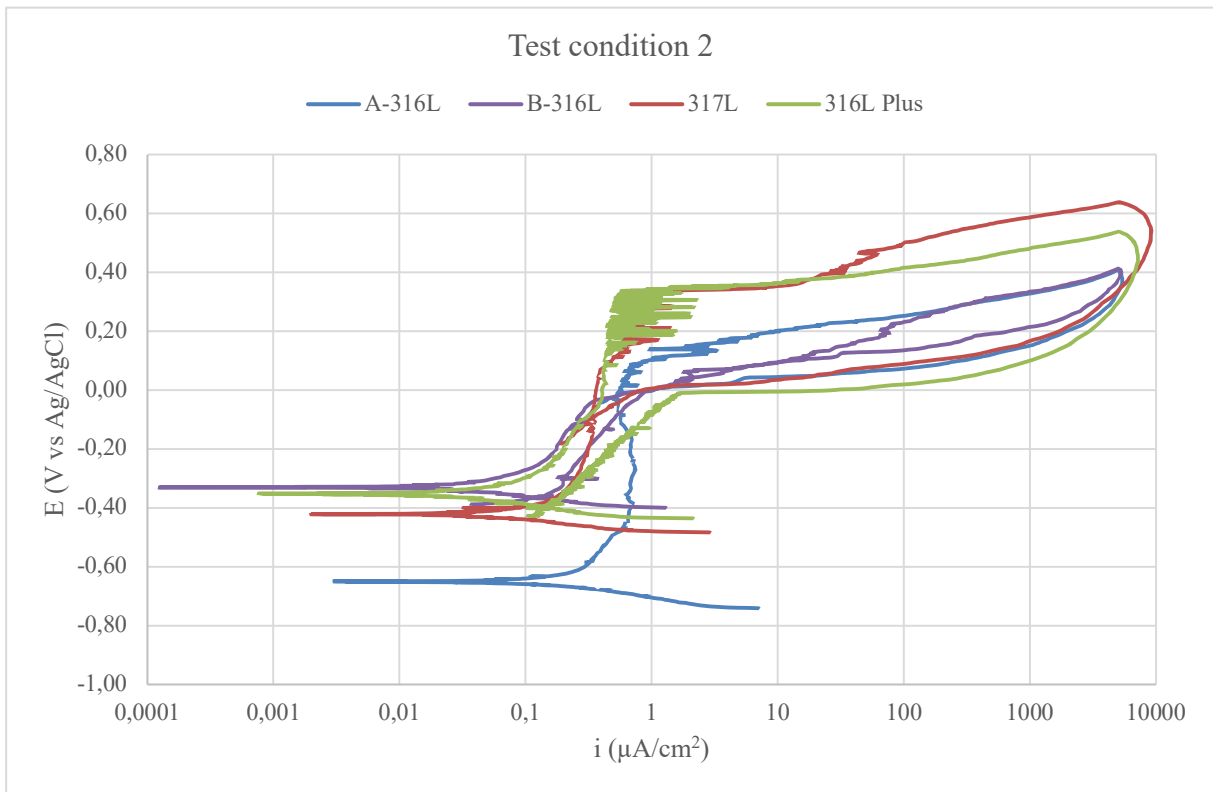


Fig. 5.2: Anodic CPP curves for A-316L, B-316L, 317L and 316 Plus obtained in 3 wt% NaCl at 35 °C.

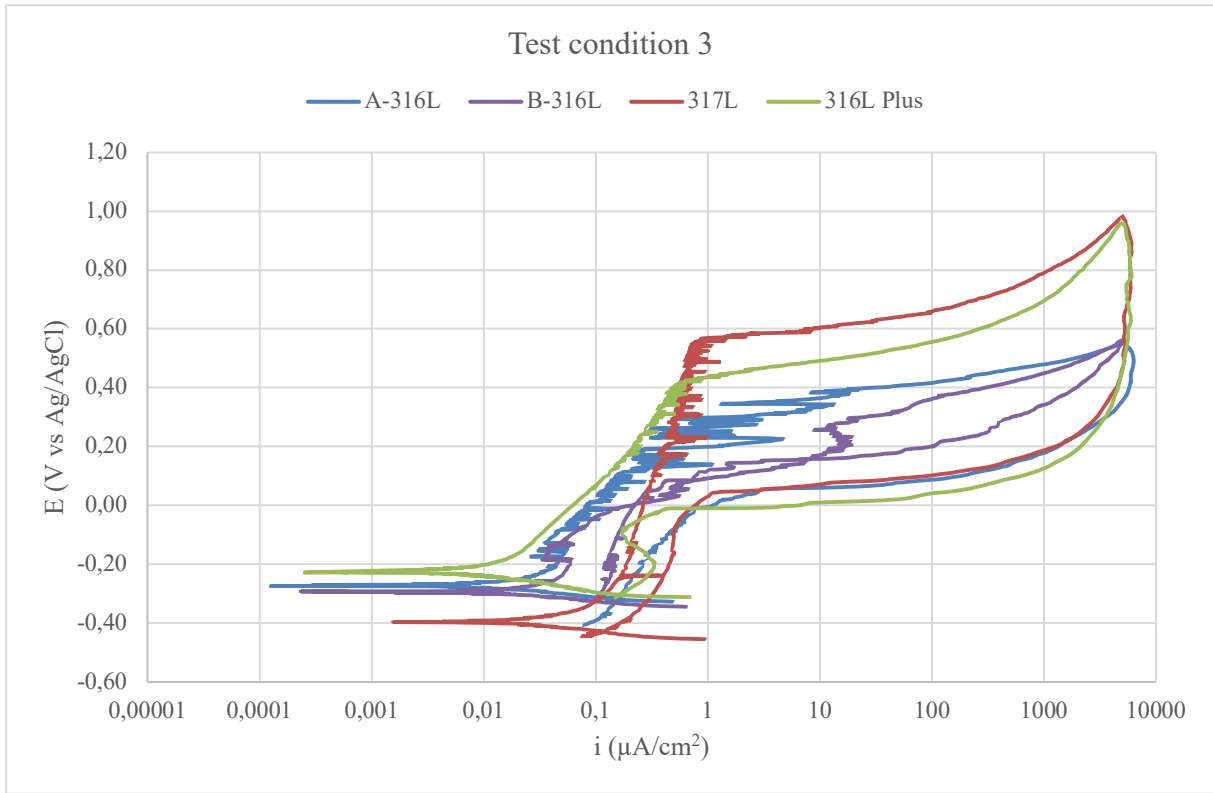


Fig. 5.3: Anodic CPP curves for A-316L, B-316L, 317L and 316 Plus obtained in 5 wt% NaCl at RT.

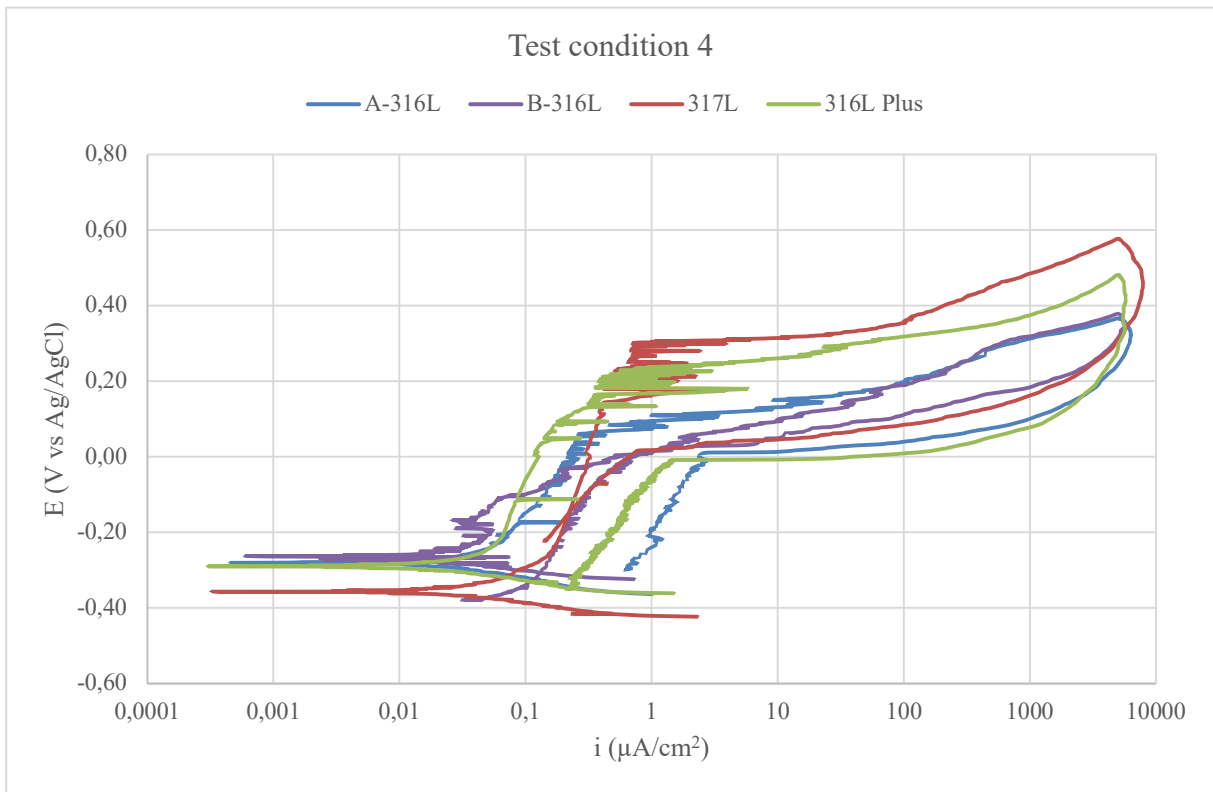


Fig. 5.4: Anodic CPP curves for A-316L, B-316L, 317L and 316 Plus obtained in 5 wt% NaCl at 35 °C.

Table 5.1: Parameters obtained from the anodic CPP curves recorded in 3 wt% NaCl at RT.

Test material	OCP (V)	E _{pit} (V)	E _{rep} (V)	i _{pass} (μA/cm ²)	PSF
A-316L	-0.64	0.27	0.051	0.62	0.24
B-316L	-0.25	0.050	0.050	0.032-0.18	0.00
317L	-0.49	0.53	0.061	0.46	0.46
316 Plus	-0.36	0.45	-0.014	0.20	0.57

Table 5.2: Parameters obtained from the anodic CPP curves recorded in 3 wt% NaCl at 35 °C.

Test material	OCP (V)	E _{pit} (V)	E _{rep} (V)	i _{pass} (μA/cm ²)	PSF
A-316L	-0.65	0.12	-0.0056	0.63	0.16
B-316L	-0.33	-0.047	-0.047	0.20	0.00
317L	-0.42	0.33	0.018	0.39	0.42
316 Plus	-0.35	0.34	-0.0066	0.35	0.50

Table 5.3: Parameters obtained from the anodic CPP curves recorded in 5 wt% NaCl at RT.

Test material	OCP (V)	E _{pit} (V)	E _{rep} (V)	i _{pass} (μA/cm ²)	PSF
A-316L	-0.27	0.35	0.058	0.03-12.0	0.47
B-316L	-0.29	0.051	0.051	0.033-0.68	0.00
317L	-0.39	0.57	0.048	0.38	0.54
316 Plus	-0.23	0.41	-0.001	0.018-0.59	0.64

Table 5.4: Parameters obtained from the anodic CPP curves recorded in 5 wt% NaCl at 35 °C.

Test material	OCP (V)	E _{pit} (V)	E _{rep} (V)	i _{pass} (μA/cm ²)	PSF
A-316L	-0.28	0.08	0.012	0.16	0.20
B-316L	-0.26	-0.06	-0.059	0.003-0.25	0.00
317L	-0.39	0.29	0.038	0.30	0.37
316 Plus	-0.29	0.21	-0.009	0.17	0.44

Table 5.5: The potential (V) where metastable pitting starts at the different test conditions.

Test material	Test condition 1	Test condition 2	Test condition 3	Test condition 4
A-316L	0.051	-0.0056	0.058	0.012
B-316L	-	-	-	-
317L	0.077	0.085	0.091	0.13
316 Plus	0.13	0.051	0.18	0.044

5.1.1 Surface characterisation

The surface of each material that contained the most severe attacks after anodic CPP in 5 wt% NaCl at 35°C was analysed to compare the pitting corrosion attacks among the test materials. Average pit depth, average diameter and the number of pits were obtained with IFM, and these parameters were used to obtain a pit rating number with a standard chart as described in ASTM G46[68]. The different parameters and the pit rating are presented in Table 5.6, where the pit depth and diameter from this analyse are the largest measured for each pit. B-316L contained a large number of pits with depth smaller than 50 µm which was not considered when counting the number of pits and calculating average pit depth and diameter. The lateral edges on the samples contained pits as well, but these were not considered since it is challenging to investigate the lateral edges on B-316L and 316 Plus due to the thickness of these samples.

Table 5.6: Average pit depth and diameter, number of pits and pit rating according to ASTM G46 for each sample after recording anodic CPP curves in 5 wt% NaCl at 35 °C.

Test material	Number of pits	Average pit diameter (µm)	Average pit depth (µm)	Pit rating
A-316L	23	605.25	211.24	A-3, B-1, C-1
B-316L	50	312.35	116.11	A-4, B-1, C-1
317L	13	608.85	73.77	A-2, B-1, C-1
316 Plus	5	771.92	188.02	A-2, B-1, C-1

The surface of each sample subjected to anodic CPP in 5 wt% NaCl at 35°C are presented in Fig. 5.5-Fig. 5.8, which was obtained with IFM at 10X magnification. As it can be seen from the figures, there is a large variation on the pit density where B-316L contained a great number of pits compared to the other test materials.

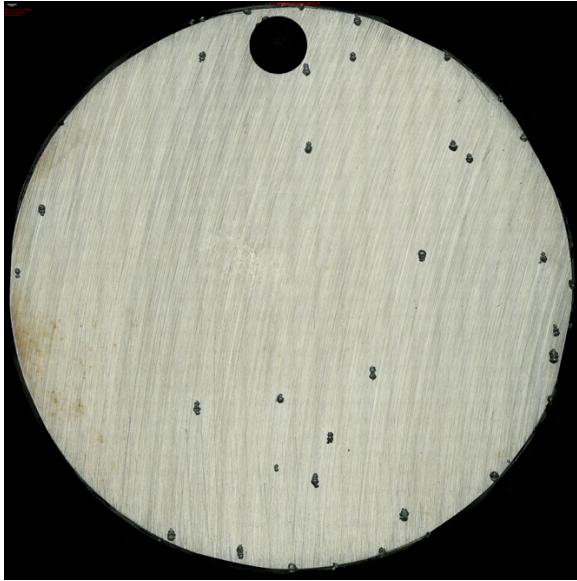


Fig. 5.5: The A-316L surface after anodic CPP in 5 wt% NaCl at 35 °C.



Fig. 5.6: The B-316L surface after anodic CPP in 5 wt% NaCl at 35 °C.

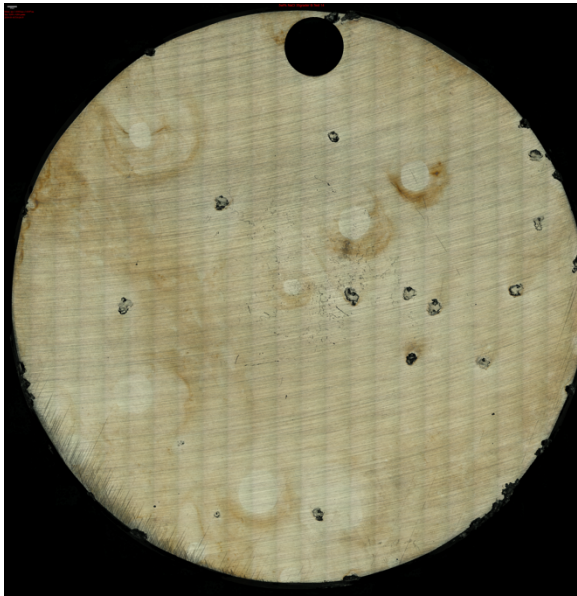


Fig. 5.7: The 317L surface after anodic CPP in 5 wt% NaCl at 35 °C.



Fig. 5.8: The 316 Plus surface after anodic CPP in 5 wt% NaCl at 35 °C.

5.2 Open circuit potential measurements

OCP measurements of A-316L, B-316L, 317L and 316 Plus were conducted to investigate the difference in pitting corrosion resistance among the test materials, and to compare the OCP for each test material to the anodic CPP curves obtained at equivalent temperature and solution. The OCP measurements were conducted in a 5 wt% NaCl solution at 35°C for two weeks and at RT the last two days, and oxygen purging was performed the last three days.

The OCP measurement for each test material are presented in Fig. 5.9-Fig. 5.12. Between day 1-2 and 4-6 noise can be observed, which was caused by lack of ionic contact between the RE and bulk solution due to air bubbles in the salt bridge. As it can be seen from the figures, purging with oxygen from day 13 caused a noticeable OCP increase only for 317L, while A-316L exhibited a slightly higher more stable noisy value. The curves for A-316L, B-316L and 316 Plus exhibited large potentials drops and rises at 35°C, and a change in this trend can be observed when the temperature was decreased to RT on day 14.

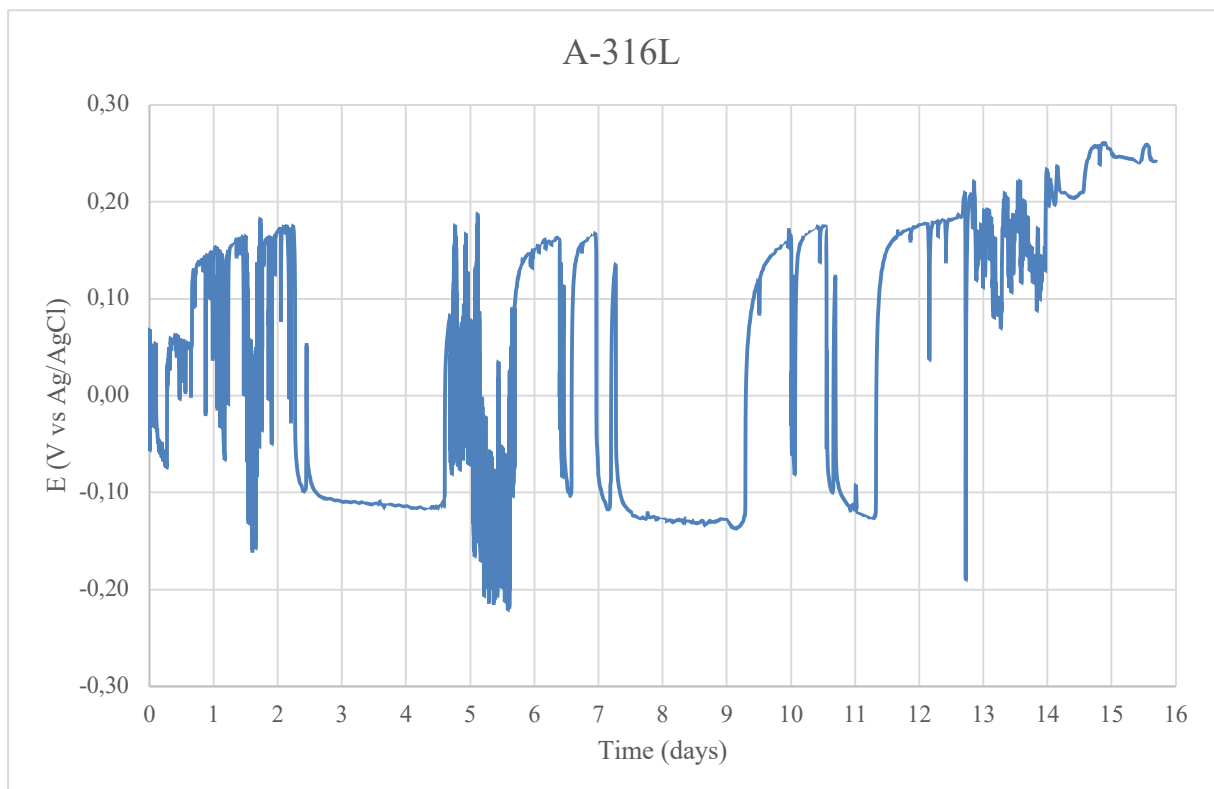


Fig. 5.9: OCP measurement for A-316L in 5 wt% NaCl at 35°C (day 0-14) and at RT (day 14-16)

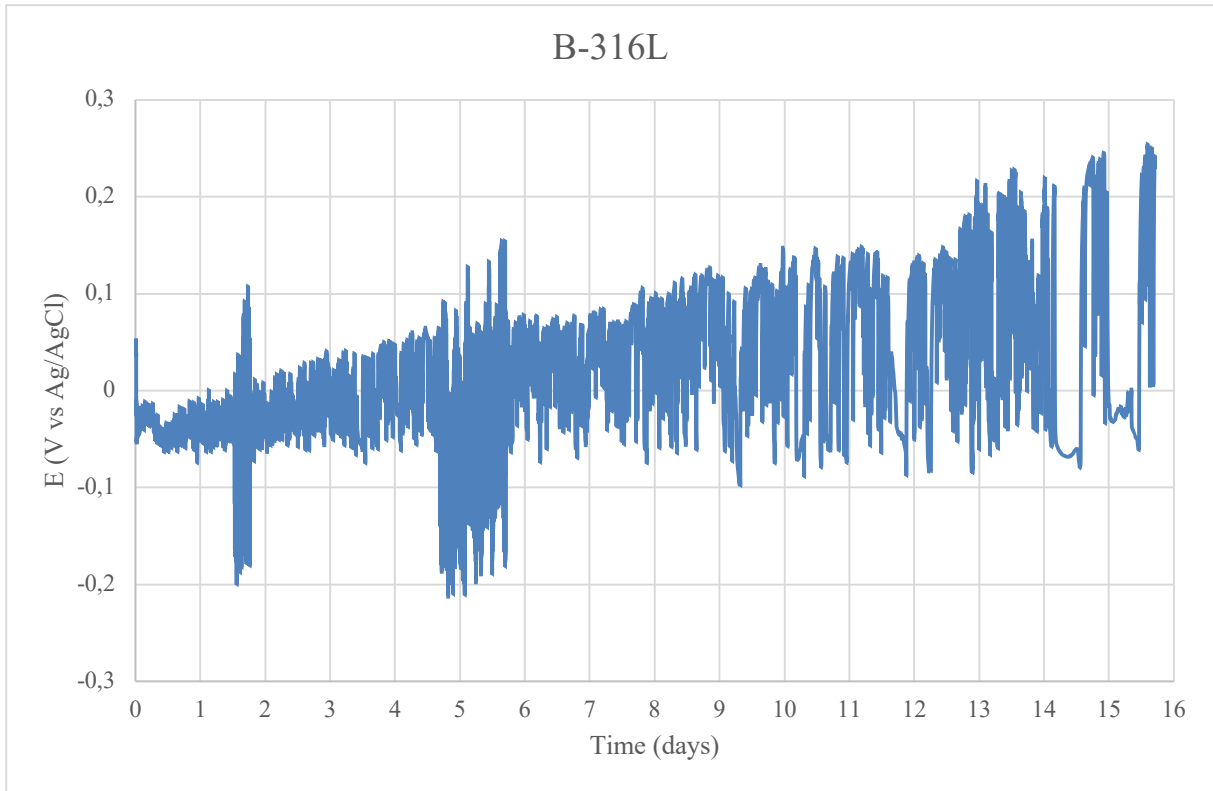


Fig. 5.10: OCP measurement for B-316 L in 5 wt% NaCl at 35 °C (day 0-14) and at RT (day 14-16).

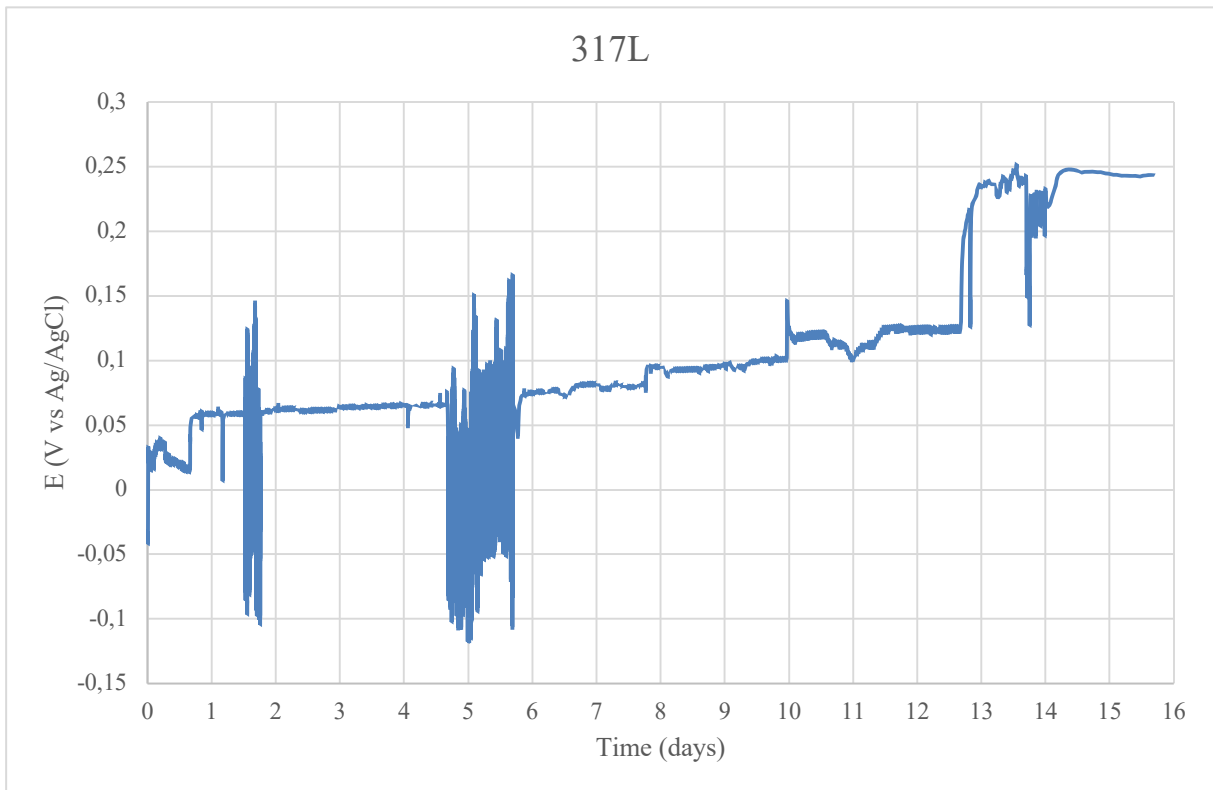


Fig. 5.11: OCP measurement for 317L in 5 wt% NaCl at 35 °C (day 0-14) and at RT (day 14-16).

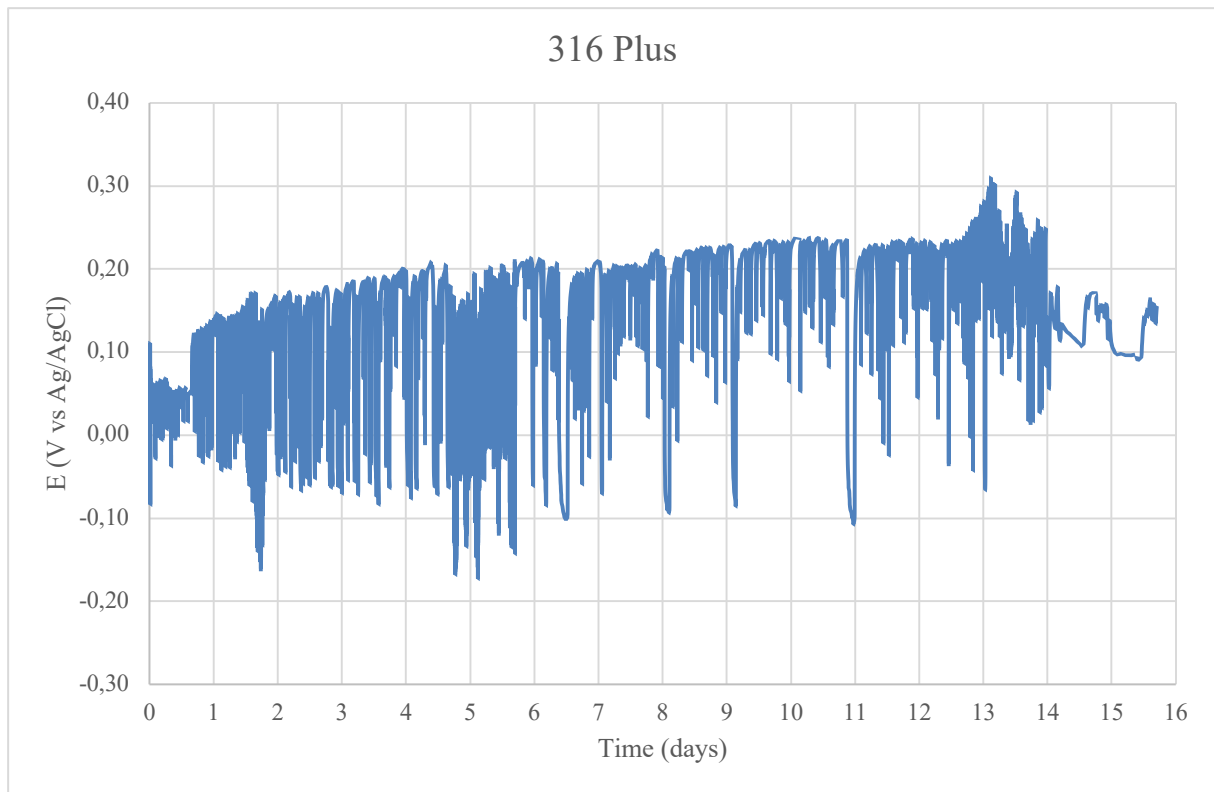


Fig. 5.12: OCP measurement for 316 Plus in 5 wt% NaCl at 35 °C (day 0-14) and RT (day 14-16).

5.2.1 Surface characterisation

The sample surfaces after OCP measurement in 5 wt% NaCl at 35 °C for 14 days and at RT for two days were investigated to compare the measurements to the surface condition after the exposure. Indications of metastable pitting or stable pitting corrosion during the OCP measurements can be confirmed through surface examinations. According to the IFM analyse, corrosion attacks could not be seen on 317L. The observations on A-316L, B-316L and 316 Plus are presented in this chapter.

The A-316L surface contained one pit of 9.18 µm depth and 179.64 µm diameter, however on the lateral edge a brown blue and pitted area was observed. The attacked area on the lateral edge is presented in Fig. 5.13, which was obtained with 5X magnification. As it can be seen from the figure, both pits and a brown coloured area which indicates changes in the surface can be observed. The pit depths and diameters were below 1.16 µm and 178.66 µm, respectively. Furthermore, the curvature of the sample surface arises since the sample were circular.

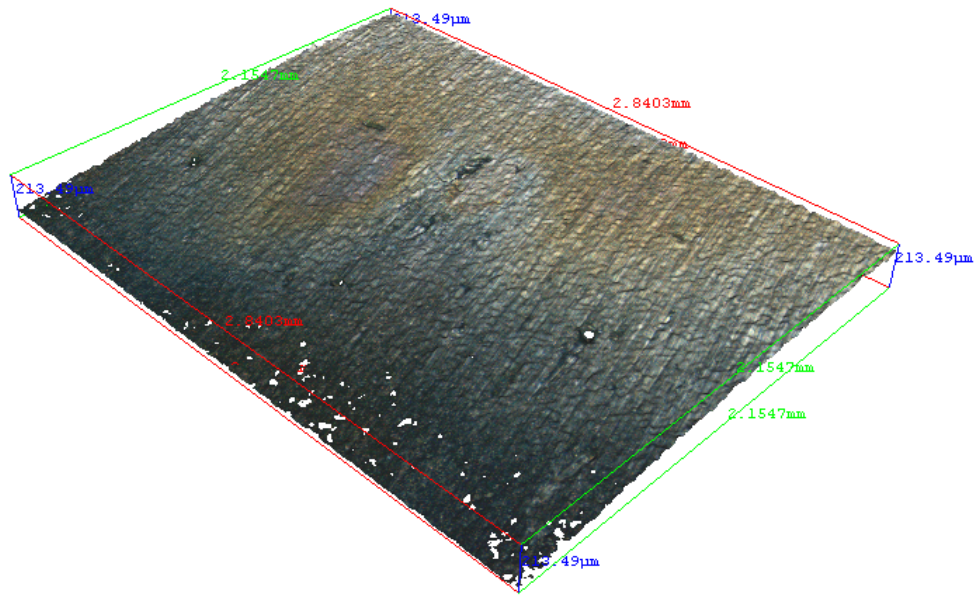


Fig. 5.13: 3D photograph of the pitted area on the lateral edge of A-316L after the OCP measurement in 5 wt% NaCl at 35 °C for 14 days and at RT for two days.

B-316L contained several pits with a surrounding brown and blue colour scattered over the surface as presented in Fig. 5.14 a), which was obtained with 5X magnification. Fig. 5.14 b) illustrates the characteristics of these pits obtained with 50X magnification, which indicate either containments or changes in the passive film close to the pits. The depths of these pits were in the order of 50 nm to 2 µm. Additionally, the lateral edge contained visually indications of pits.

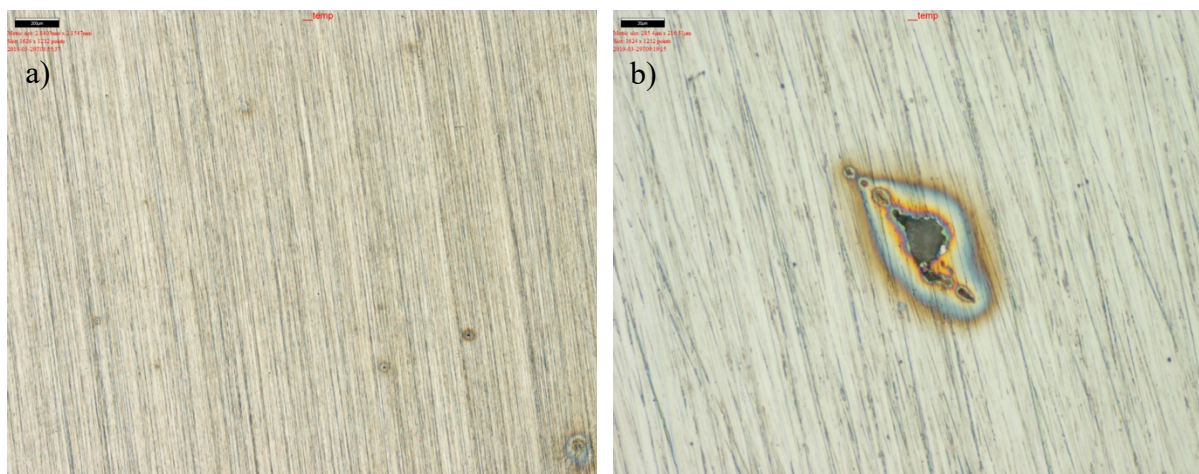


Fig. 5.14: Pits on B-316L surrounded by a brown and blue colour after the OCP measurement in 5 wt% NaCl at 35 °C for 14 days and at RT for two days. a) Several pits obtained with 5X magnification and b) the characteristics of these pits obtained with 50X magnification.

The blue and brown spots on B-316L observed with IFM were investigated with EDS point analyse, which detected the elements Fe, Cr, Mo, Ni, Mn and Si on both the bulk surface and the spots. In this analyse, the elements in 21 blue and brown spots were investigated, and 17 points at the bulk surface were included. A similar amount (wt %) of Si, Ni and Mn were detected on both the bulk surface and the spot. However, the Mo and Cr amount were higher in the spot compared to the bulk solution, while the Fe amount was less as presented in Fig. 5.15- Fig. 5.17. Since the boxes does not overlap, it indicates that there is a composition difference between the spots and the bulk surface.

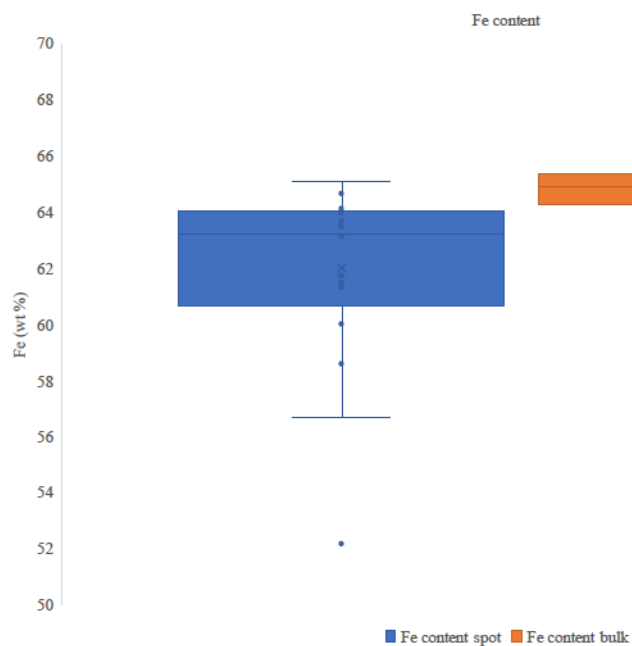


Fig. 5.15: The amount of Fe (wt%) at the spots and bulk surface for B-316L.

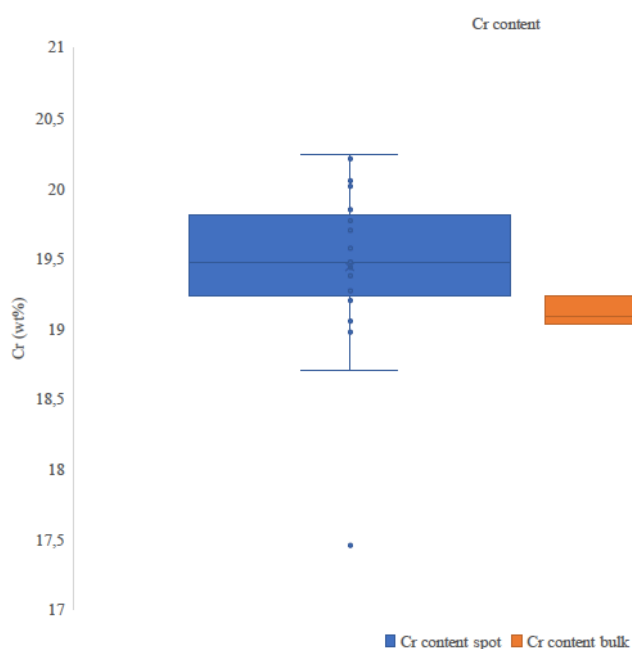


Fig. 5.16: The amount of Cr (wt%) at the spots and bulk surface for B-316L.

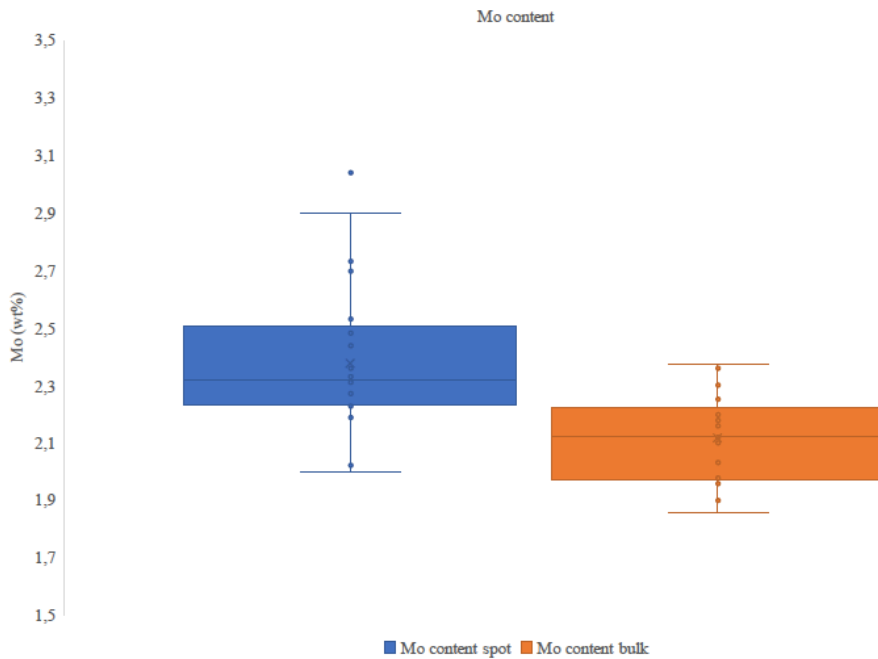


Fig. 5.17: The amount of Mo (wt%) at the spots and bulk surface for B-316L.

Through the IFM analyse five shallow dish shaped pits on 316 Plus were observed, and two are presented in Fig. 5.18 obtained with 20X magnification. One of the five pits was 5.16 μm deep with 286.59 μm diameter, while the others were in the order of 1 μm deep and 150 μm diameter. One of the pits observed on 316 Plus with SEM is presented in Fig. 5.19, while an indication of a pit that initiated and repassivated shortly after initiation is presented in Fig. 5.20.

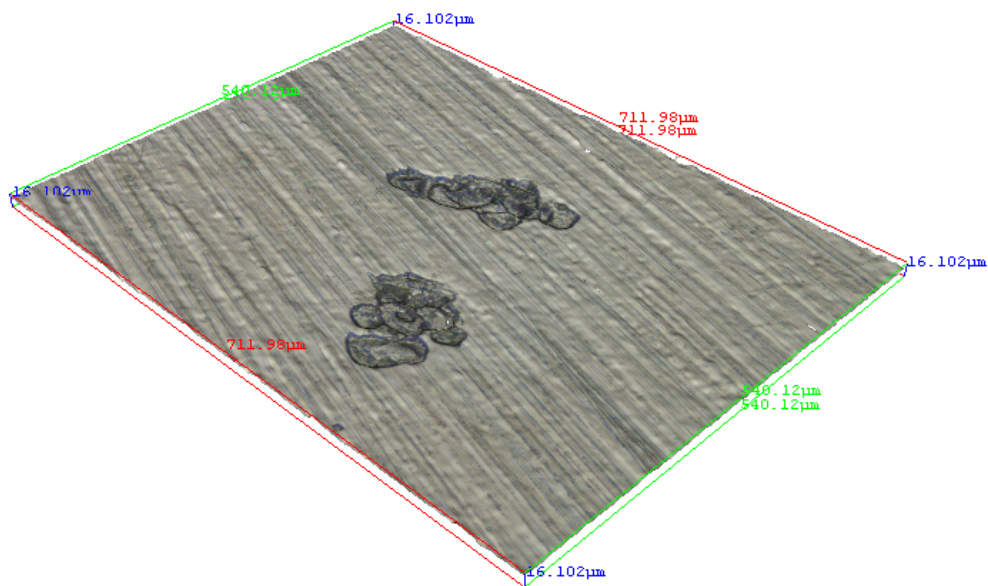


Fig. 5.18: Shallow dish shaped pits on 316 Plus after the OCP measurement in 5 wt% NaCl at 35 °C for 14 days and at RT for two days.

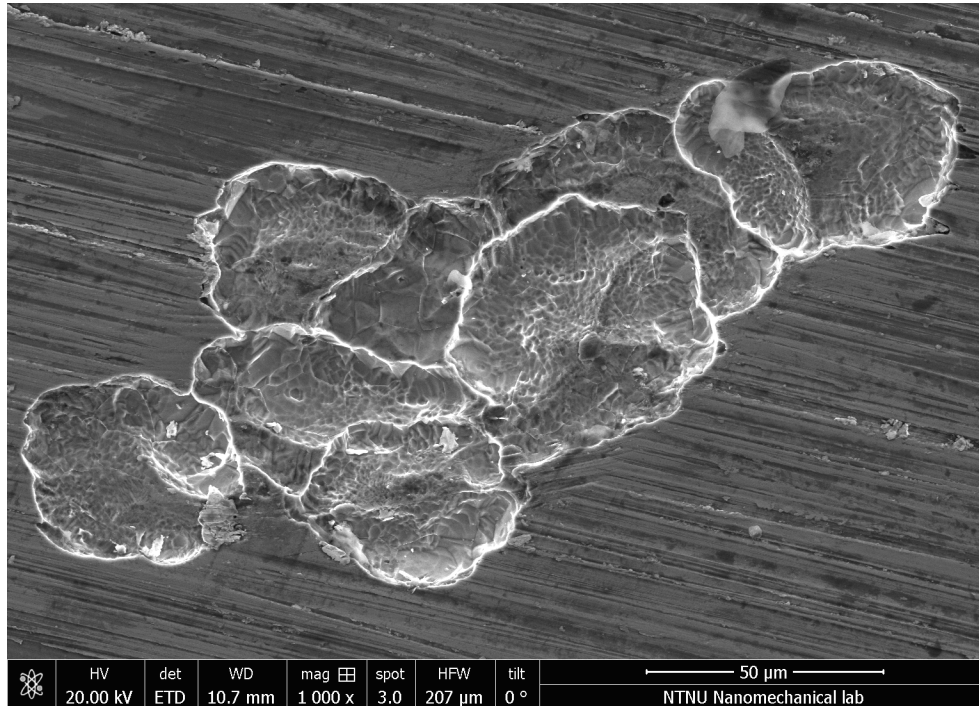


Fig. 5.19: Pit on 316 Plus after the OCP measurement in 5 wt% NaCl at 35 °C for 14 days and at RT for two days.

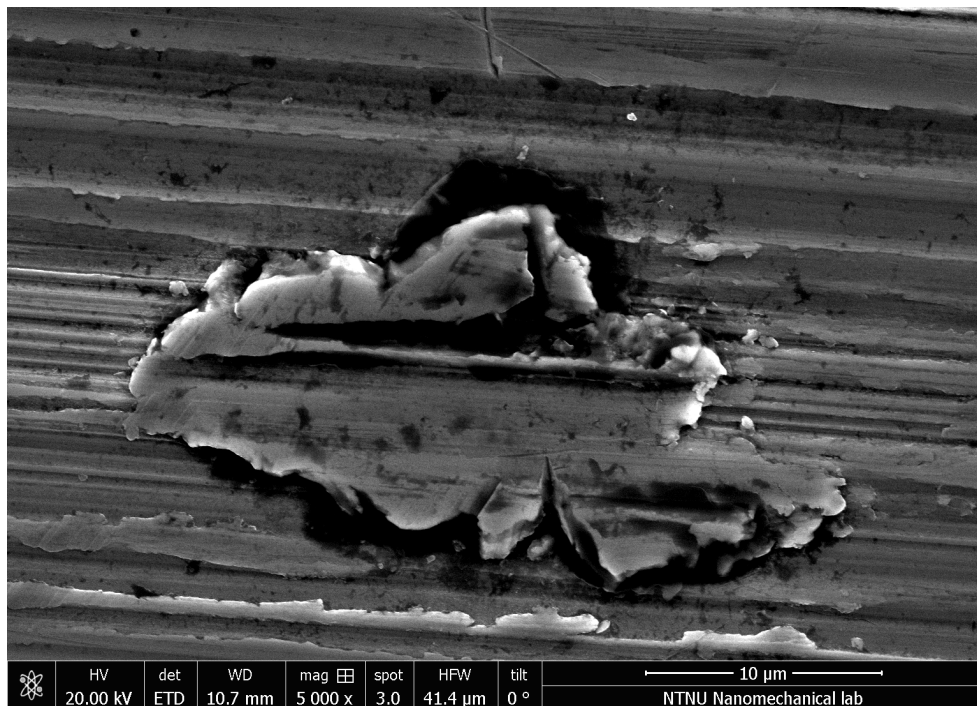


Fig. 5.20: Indications of a pit that re-passivated shortly after initiation on 316 Plus after the OCP measurement in 5 wt% NaCl at 35 °C for 14 days and at RT for two days.

5.3 Salt spray test

To compare the relative corrosion resistance of A-316L, B-316L, 316 Plus and 317L at simulated atmospheric conditions the test materials were exposed in a salt spray chamber according to ASTM B117[80]. The exposure was conducted with a 5 wt% NaCl salt spray solution with the chamber temperature kept at 35 ± 2 °C. Information on the relative corrosion resistance after the exposure was obtained by visual inspection, weight loss measurements and IFM investigation of crevice corrosion attacks, which are presented in this chapter. The anodic CPP curves of the coated samples conducted to obtain OCP, E_{crev} , E_{rep} and i_{pass} are presented in the next chapter.

After 27 days, crevice corrosion was observed on A-316L, and after 50 days crevice corrosion was observed on both 316 Plus and B-316L. When the exposure in the salt spray chamber was completed after 67 days, no further crevice corrosion attacks at the coating were observed after removing the mineral wool as shown in Fig. 5.21. One of the A-316L samples that was not grinded and coated visually showed significant corrosion attacks on the lateral edge, while the other not grinded samples contained mild and insignificantly corrosion attacks. Furthermore, marking the samples with a scribe needle did not act as an initiation site since corrosion were not observed at the marks.



Fig. 5.21: The samples after 67 days in the salt spray chamber at 35 ± 2 °C with a 5 wt% NaCl salt spray solution. Crevice corrosion was observed on A-316L, B-316L and 316 Plus.

The weight loss per unit area and the visual observation of the coated samples are presented in Table 5.7, where it is specified which samples that were covered with mineral wool. The visual observation was divided into crevice corrosion underneath the coating (cc), pitting corrosion (pc) and no corrosion (nc). Since the corrosion attacks underneath the mineral wool were similar to the pitting corrosion attacks, these are named pitting corrosion in this investigation. Insignificant pitting corrosion occurred at edges, beneath samples and underneath the mineral wool.

Table 5.7: Weight loss per unit area and visual observation of the samples after exposure in the salt spray chamber with a 5 wt% NaCl salt spray solution at 35 °C. The visual observation was divided into crevice corrosion (cc) underneath the coating, pitting corrosion (pc) and no corrosion (nc).

Sample number	Area (cm²)	Weight after (g)	Weight loss per unit area (g/m²)	Visual observation
1: A-316L	20.2484	44.3134	3.5081	cc
2: A-316L (mineral wool)	20.5131	44.6134	0.7312	pc
3: A-316L (mineral wool)	20.7548	44.8031	0.3372	pc
4: A-316L	20.6170	44.2174	0.6305	nc
1: 317L	20.5287	43.7688	0.8281	nc
2: 317L (mineral wool)	20.3945	43.7587	0.7845	pc
3: 317L (mineral wool)	20.6588	44.3634	0.8229	pc
4: 317L	20.3487	44.4957	0.6389	pc
1: 316 Plus	26.8058	28.1147	1.1191	cc, pc
2: 316 Plus (mineral wool)	27.2432	28.5790	0.7708	pc
3: 316 Plus (mineral wool)	26.9740	28.4816	0.5561	pc
4: 316 Plus	26.8704	28.5088	0.4466	pc
1: B-316L	16.8496	22.5891	2.9674	cc
2: B-316L (mineral wool)	16.5760	22.5031	1.6892	pc
3: B-316L (mineral wool)	16.7831	22.1458	0.5958	pc
4: B-316L	16.5041	22.2407	0.7271	pc

Fig. 5.22 presents the weight loss per unit area of the coated samples, where the different exposure variables are specified. The samples were tilted to avoid a thick water layer on the surface and one of each was not tilted as can be seen in Fig. 5.21. The corrosion attacks observed on B-316L were more significant beneath the sample than at the surface underneath the mineral wool.

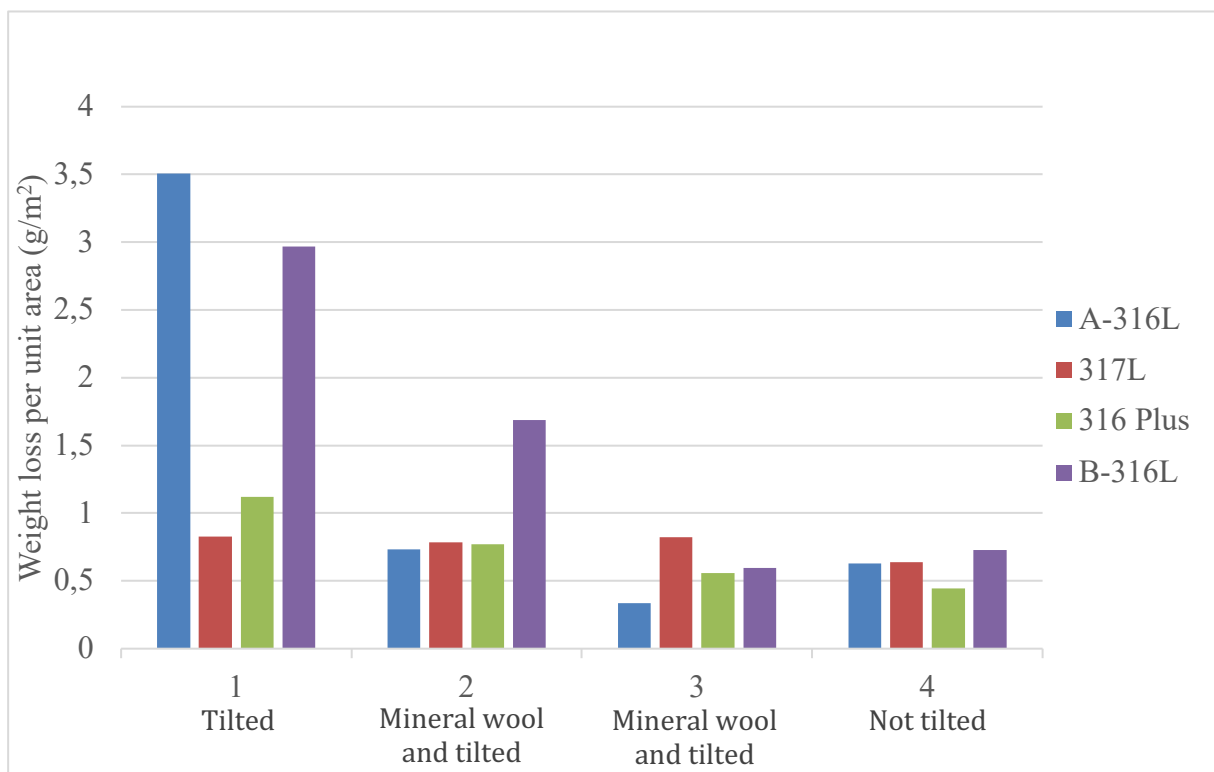


Fig. 5.22: Weight loss per unit area of A-316L, 317L, 316 Plus and B-316L after exposure in the salt spray chamber kept at 35 ± 2 °C with a 5 wt% NaCl salt spray solution. The samples are divided into groups depending on the different experimental variables during the exposure.

The crevice corrosion attacks on A-316L, B-316L and 316 Plus are presented in Fig. 5.23-Fig. 5.25, obtained with IFM at 5X magnification. These crevice corrosion attacks appeared as uniform corrosion, and a great amount of corrosion products can be observed on the samples. It was not possible to remove the corrosion products seen in the figures by cleaning with distilled water at ambient temperature. Additionally, residual coating that was not possible to remove carefully on A-316L and 316 Plus are marked. Compared to the crevice corrosion attacks, the pitting corrosion attacks were insignificantly. Fig. 5.26 illustrates an example of the insignificant pitting corrosion attacks marked with red circles. The size of these appeared to be visually similar for all test materials that exhibited pitting corrosion.

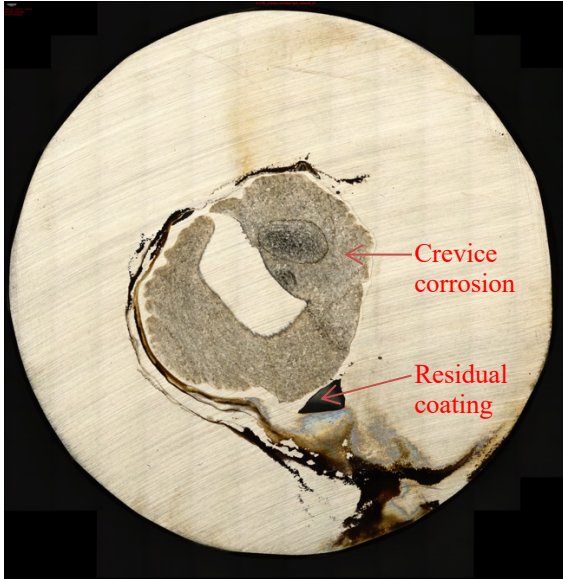


Fig. 5.23: Crevice corrosion attack on A-316L after exposure in the salt spray chamber at $35 \pm 2^\circ\text{C}$ with a 5 wt% NaCl salt spray solution.

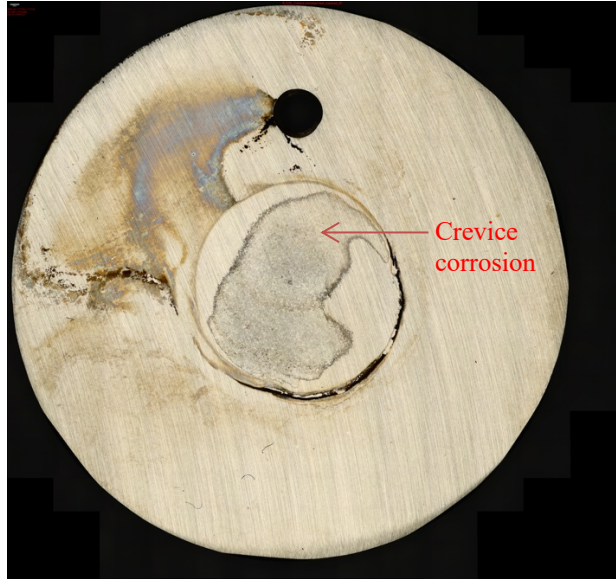


Fig. 5.24: Crevice corrosion attack on B-316L after exposure in the salt spray chamber at $35 \pm 2^\circ\text{C}$ with a 5 wt% NaCl salt spray solution.



Fig. 5.25: Crevice corrosion attack on 316 Plus after exposure in the salt spray chamber at $35 \pm 2^\circ\text{C}$ with a 5 wt% NaCl salt spray solution.

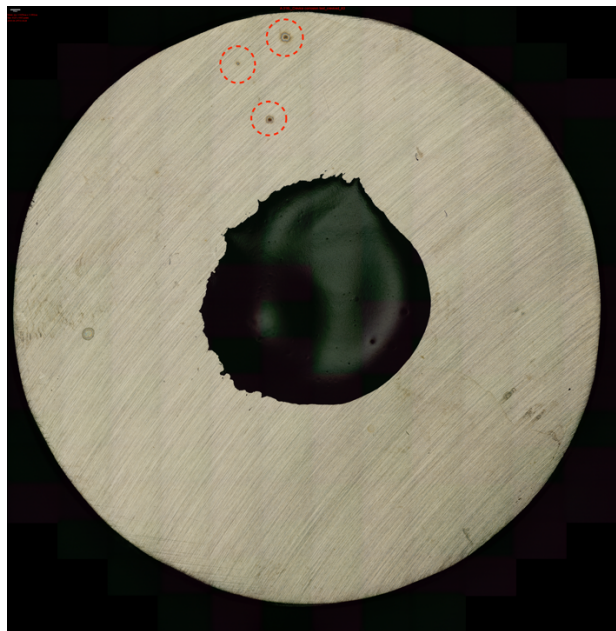


Fig. 5.26: A-316L after exposure in the salt spray chamber at $35 \pm 2^\circ\text{C}$ with a 5 wt% NaCl salt spray solution and mineral wool placed on the surface. Small and insignificant pitting corrosion attacks are marked with red circles.

5.3.1 Anodic cyclic potentiodynamic polarisation curves of coated samples

Anodic CPP of samples coated to simulate a crevice were recorded according to ASTM G61[62] to obtain OCP, E_{crev} , E_{rep} and i_{pass} . The purpose of obtaining these parameters were to investigate the effect of Mo content with respect to crevice corrosion and to compare this result with the salt spray exposure. The sample surfaces contained evidently pitting corrosion attacks, while no attacks were observed at the coating edge. Hence, crevice corrosion did not occur, and E_{crev} are named E_{pit} in this analyse. The anodic CPP curves for the samples with coating on the surface are presented in Fig. 5.27, and the corresponding OCP, E_{pit} , E_{rep} and i_{pass} are presented in Table 5.8.

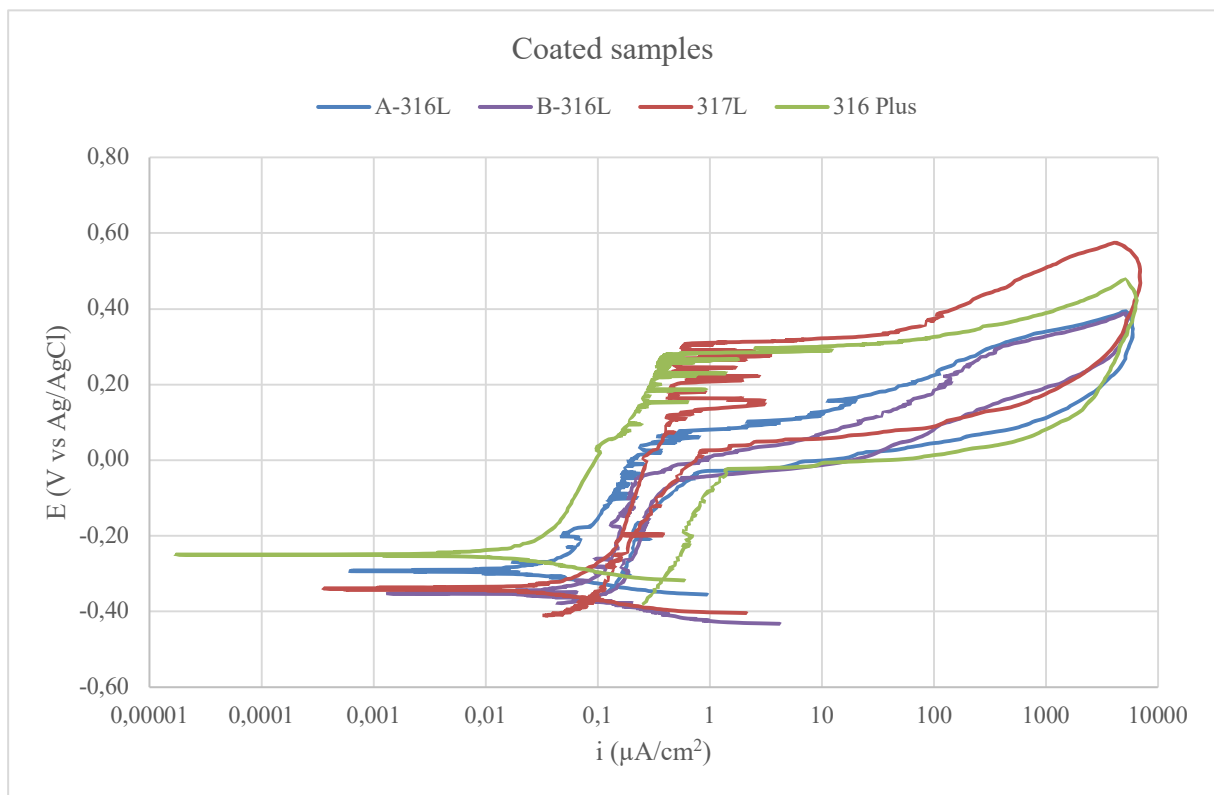


Fig. 5.27: Anodic CPP curves obtained in 5 wt% NaCl at $35\text{ }^{\circ}\text{C} \pm 2$ for the samples with coating that simulated a crevice.

Table 5.8: Parameters obtained from the anodic CPP curves of the coated samples conducted in 5 wt% NaCl at $35\text{ }^{\circ}\text{C} \pm 2$.

Test material	OCP (V)	E_{pit} (V)	E_{rep} (V)	i_{pass} ($\mu\text{A}/\text{cm}^2$)
A-316L	-0.29	0.046	-0.028	0.056-0.54
B-316L	-0.35	-0.047	-0.044	0.19
317L	-0.34	0.29	0.040	0.26
316 Plus	-0.25	0.27	-0.020	0.040-0.43

5.4 Artificial pit experiments

Artificial pit experiments were conducted with A-316L at RT with different set ups in 6 wt% FeCl₃ to investigate propagation of a single pit and the effect of cathode area. Furthermore, the effect of electrolyte was included by changing the electrolyte to 5 wt% NaCl for one of the beakers. Prior to and after the artificial pit experiments the pH was measured, which are presented below. In the next chapter, the results from the potential and galvanic current measurements are presented before the volume loss. Then the result from the recorded cyclic anodic and cathodic potentiodynamic polarisation curves for respectively A-316L and 6Mo are presented before the surface characterisation.

The measured pH in the beakers before and after the artificial experiments are presented in Table 5.9. Beaker 1 contained sample 1 and 3, and the electrolyte for this beaker was changed to 5 wt% NaCl after exposure in 6 wt% FeCl₃. A small decrease in pH can be observed for beaker 1, while a lower pH than prior to the experiment can be observed in beaker 2 which contained sample 2. The low pH of the 5 wt% NaCl solution are probably caused by residual FeCl₃ on the samples as the electrolyte was changed since the samples were not cleaned before exposure to 5 wt% NaCl.

Table 5.9: The measured pH of the 6 wt% FeCl₃ and 5 wt% NaCl solutions before and after the artificial pit experiments, and the temperature the pH was measured at.

Beaker	Solution	pH before	pH after	Temperature (°C) Before / after
1 (sample 1 and 3)	6 wt% FeCl ₃	1.23	1.22	22.5 / 22.0
	5 wt% NaCl	6.45	3.62	22.4 / 22.0
2 (sample 2)	6 wt% FeCl ₃	1.23	1.09	22.5 / 20.8

5.4.1 Potential and galvanic current measurements

Potential measurements of sample 1 and 2 that were connected to an external 6Mo cathode area of respectively 36.8 and 6.30 cm² and of the freely exposed sample 3 were conducted. Additionally, the galvanic current development for sample 1 and 2 were obtained from the measured potential drop by using ohms law. The galvanic current was used to obtain both the theoretical total volume loss and theoretical accumulated volume loss of each sample.

The potential development for sample 1 is presented in Fig. 5.28, and the potential development for sample 2 is presented in Fig. 5.29. Since the time the potential was measured before connecting sample 2 to the 6Mo sample was short (1 hour and 30 minutes), the first 10 hours are additionally presented in Fig. 5.30. The measured OCP for 6Mo before connecting to sample 1 was 650 mV vs Ag/AgCl, while the measured OCP for 6Mo before connecting to sample 2 was 720 mV vs Ag/AgCl. As the samples were connected to 6Mo the potential represents the coupling potential.

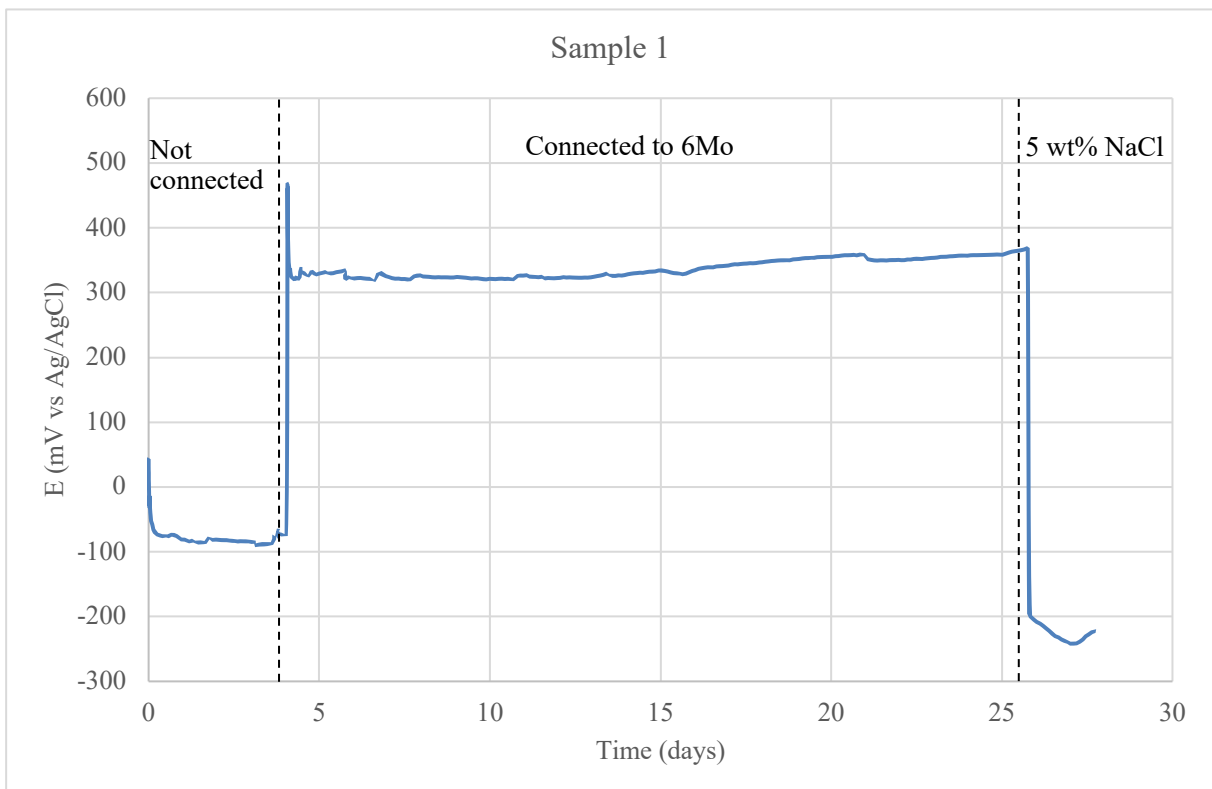


Fig. 5.28: Potential development for sample 1 during the entire exposure period, where the electrolyte was changed from 6 wt% FeCl₃ to 5 wt% NaCl after 26 days.

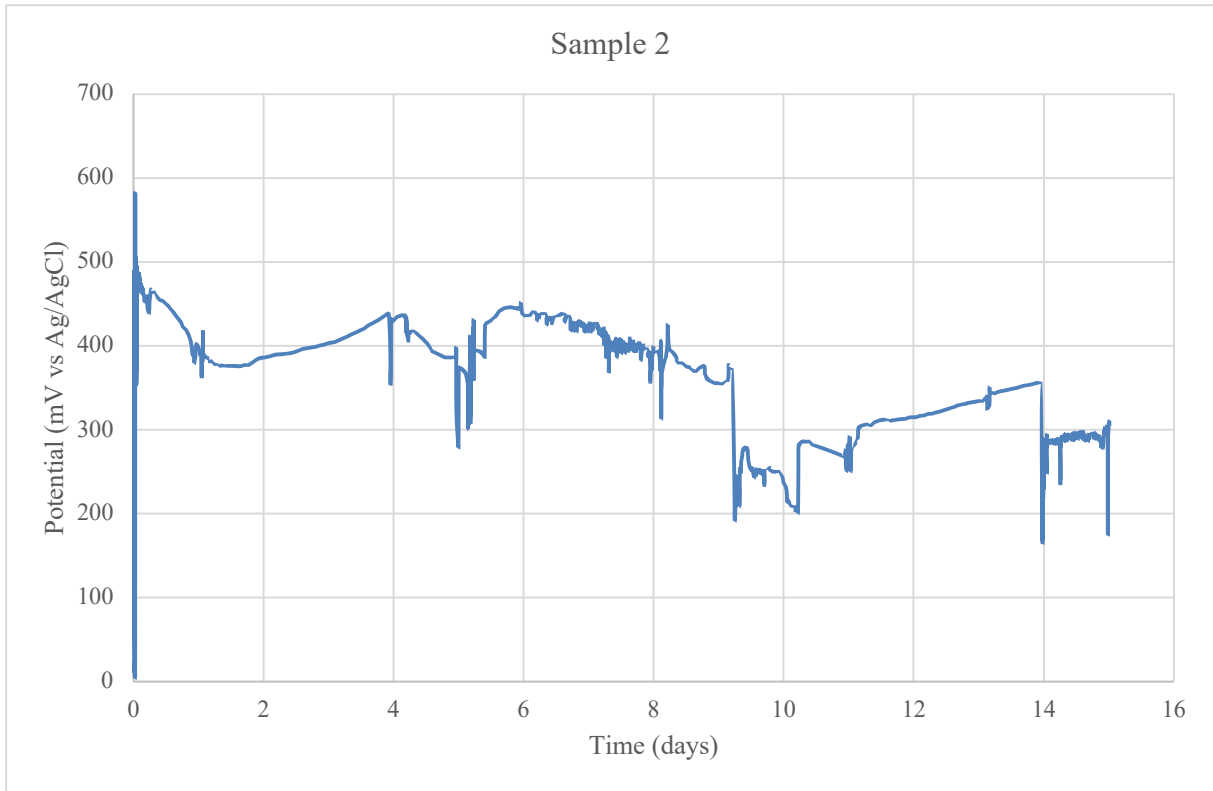


Fig. 5.29: Potential development during the entire exposure period for sample 2 in 6 wt% $FeCl_3$.

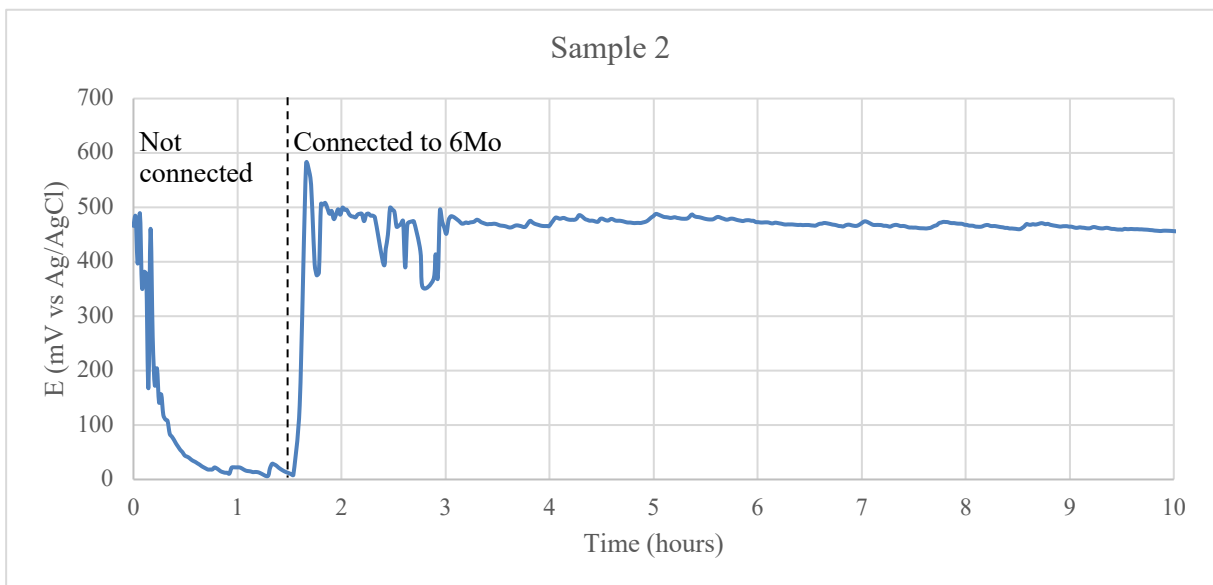


Fig. 5.30: Potential development the first 10 hours for sample 2 in 6 wt% $FeCl_3$.

The potential development for sample 3 is presented in Fig. 5.31. As it can be seen from the figure, the potential decreases slightly with time, and a potential drop can be observed when the electrolyte was changed from 6 wt% FeCl₃ to 5 wt% NaCl. The potential for sample 3 is approximately -100 mV vs Ag/AgCl in 6 wt% FeCl₃, while decreases to -310 mV vs Ag/AgCl in 5 wt% NaCl before a slight increase.

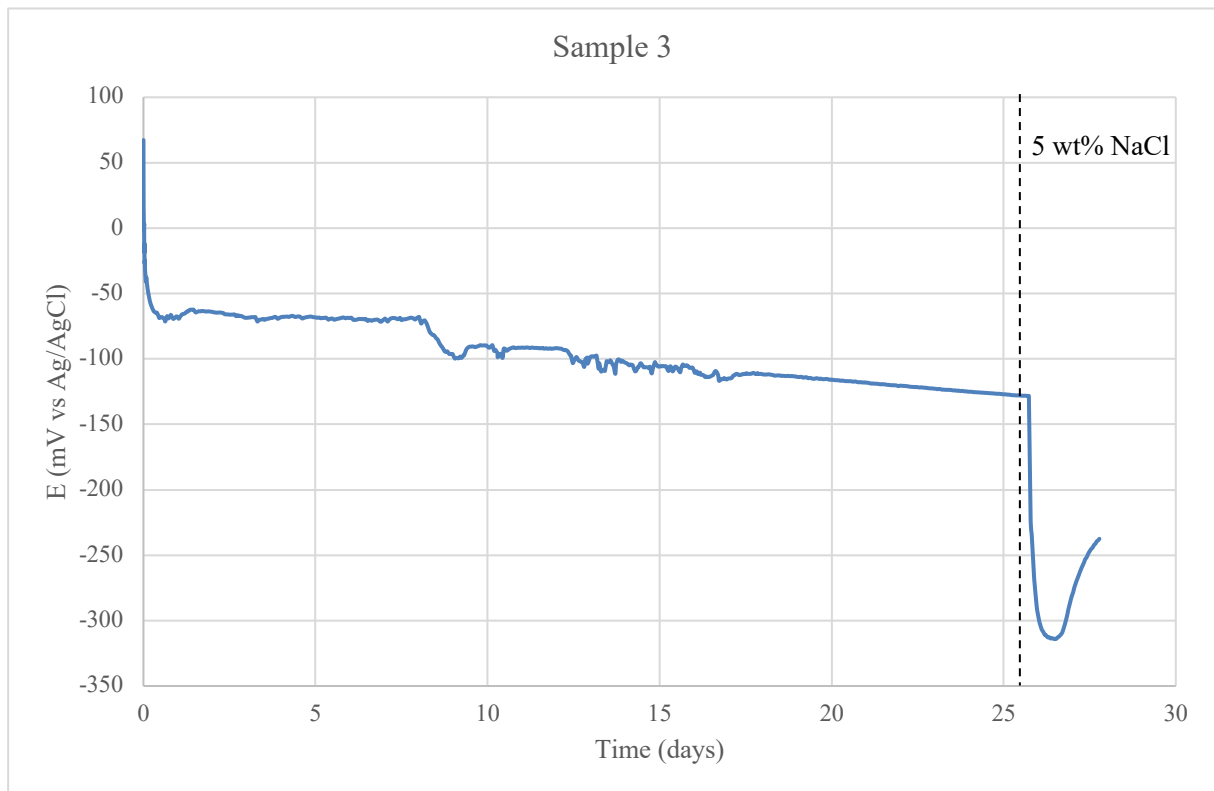


Fig. 5.31: Potential development during the entire exposure period for sample 3, which was freely exposed in 6 wt% FeCl₃. The electrolyte was changed to 5 wt% NaCl after 26 days.

The galvanic current development from the pit to the external 6Mo cathode area for sample 1 and sample 2 are presented in Fig. 5.32 and Fig. 5.33, respectively. For the duration of the test in 6 wt% FeCl₃ sample 1 exhibited a galvanic current between 3.5 to 4.3 mA, which decreased to 0.025 mA in 5 wt% NaCl. The galvanic current for sample 2 was between 1 to 3.4 mA and more unstable compared to sample 1. Due to challenges with the current logging for sample 2 the first five days, the galvanic current for this period are assumed to be the average of the measured current (2.087 mA) the last ten days.

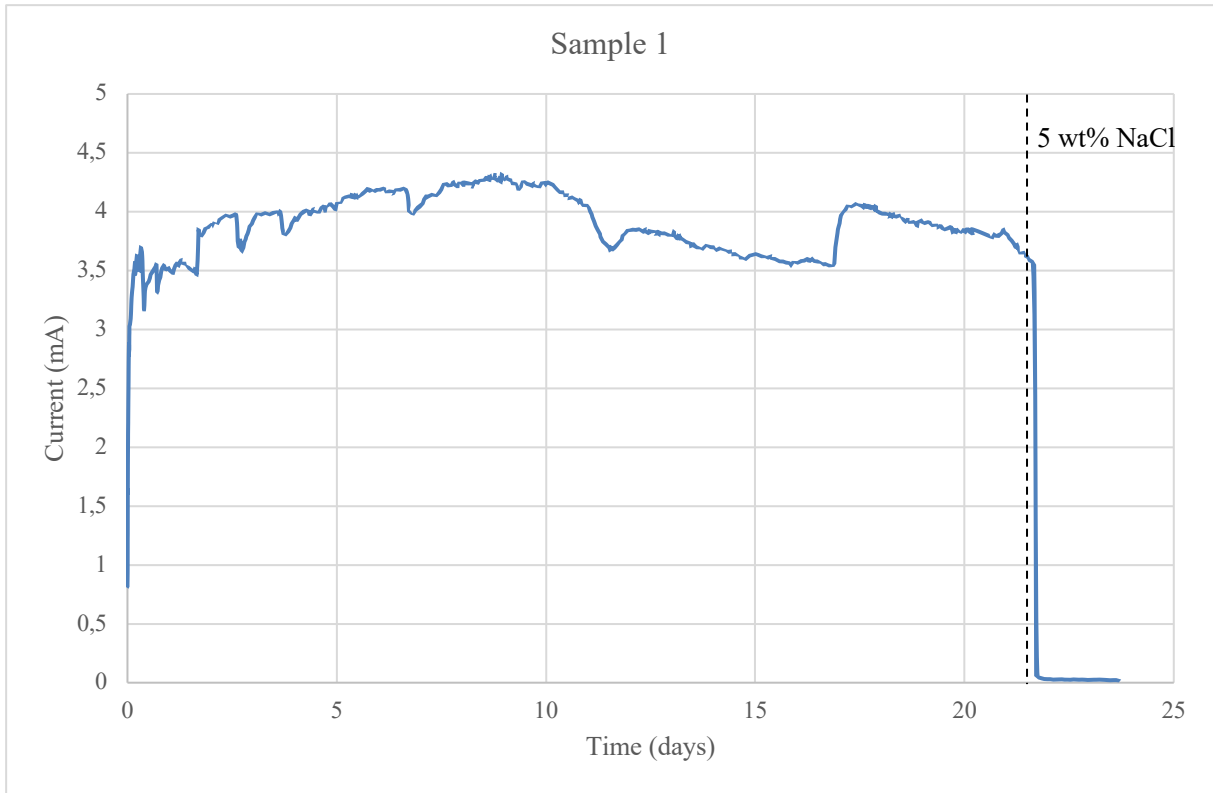


Fig. 5.32: Galvanic current development for sample 1, which was connected to 6Mo sample with a surface area of 36.8 cm^2 in 6 wt% FeCl_3 and in 5 wt% NaCl at the end of the test.

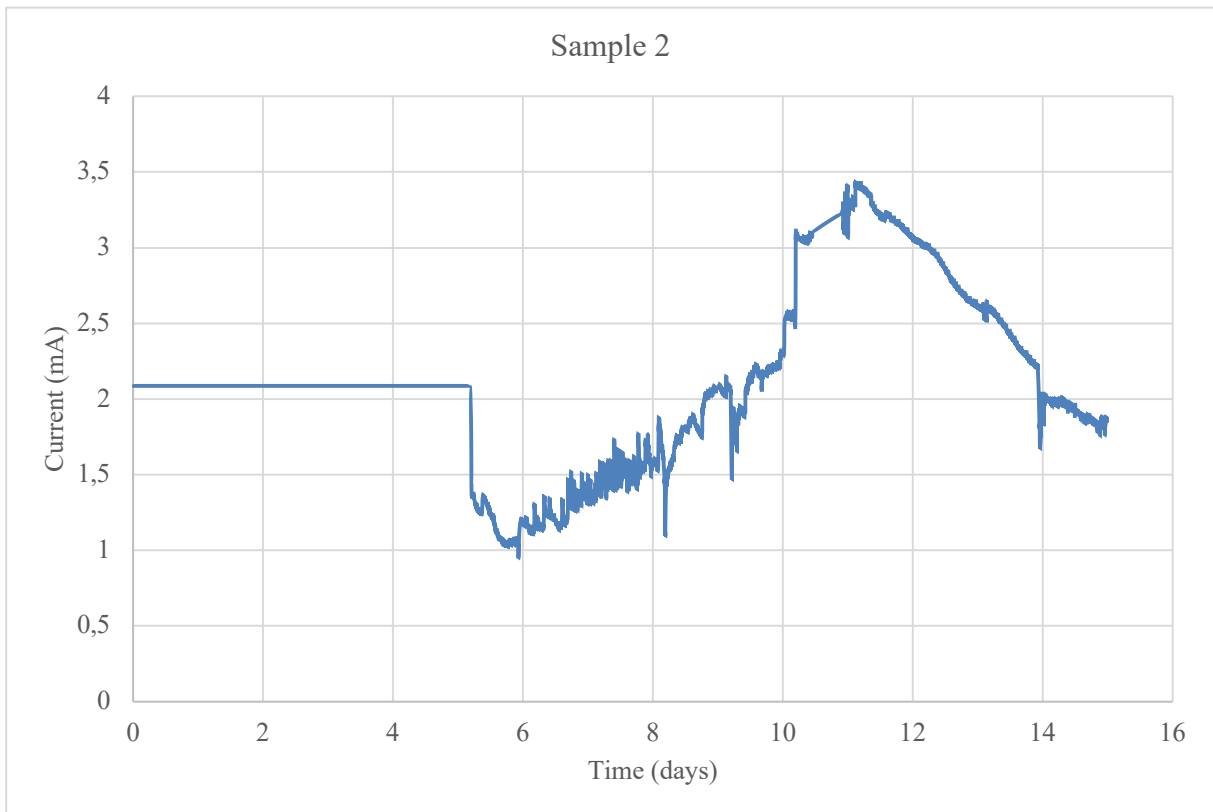


Fig. 5.33: Galvanic current development for sample 2, which was connected to a 6Mo sample with a surface area of 6.3 cm^2 in 6 wt% FeCl_3 .

Theoretical total volume loss can be calculated according to Eq.2.7, with the corresponding parameters presented in chapter 2.4.3 and the integral of the current time curves. The integral of the current time curve for sample 1 is presented in Eq. 5.1, and in Eq. 5.3 for sample 2. The calculation for theoretical total volume loss according to Faradays second law during the exposure times for sample 1 and 2 are presented in Eq. 5.2 and Eq. 5.4, respectively. For sample 1 the exposure in 5 wt% NaCl is included in the calculation since the contribution to the total volume loss after this exposure is negligible. The calculated theoretical total volume loss for sample 1 was 0.241 cm³, while the volume loss for sample 2 was 0.0908 cm³.

$$\int_{t=0}^{t=2051635\text{ s}} I(t)dt = 7293.99\text{ As} \quad (5.1)$$

$$\text{Volume loss sample 1} = \frac{M}{n\rho F} \int_{t=0}^{t=2051635\text{ s}} I(t)dt = 0.241\text{ cm}^3 \quad (5.2)$$

$$\int_{t=0}^{t=1295365\text{ s}} I(t)dt = 2748.51\text{ As} \quad (5.3)$$

$$\text{Volume loss sample 2} = \frac{M}{n\rho F} \int_{t=0}^{t=1295365\text{ s}} I(t)dt = 0.0908\text{ cm}^3 \quad (5.4)$$

The galvanic current in 6 wt% FeCl₃ for sample 1 and 2, and in 5 wt% NaCl for sample 1 was used to obtain the theoretical accumulated volume loss as a function of time as presented in Fig. 5.34 and Fig. 5.35, respectively. This was accomplished by calculating the volume loss according to Eq.2.7 at each data point for the galvanic current and adding the volume loss prior to each data point. Hence, the accumulated volume loss was obtained. As it can be seen from the trendlines, the accumulated volume loss increases linearly with time and can be described by the functions presented in the figures. The R² is close to 1 for each curve, which represents a suitable fit of the data and the linear trendline.

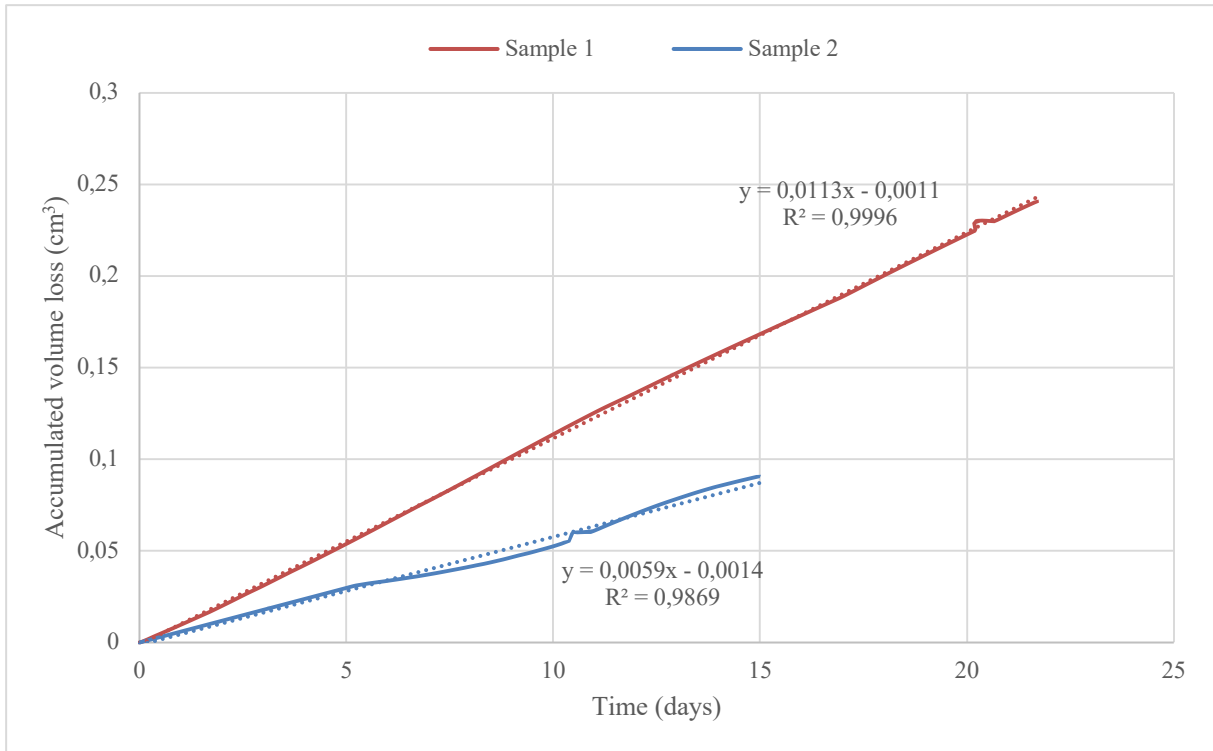


Fig. 5.34: Accumulated volume loss (cm^3) as a function of time (days) for sample 1 and 2 in 6 wt% FeCl_3 with the corresponding trendlines (stippled lines) and functions.

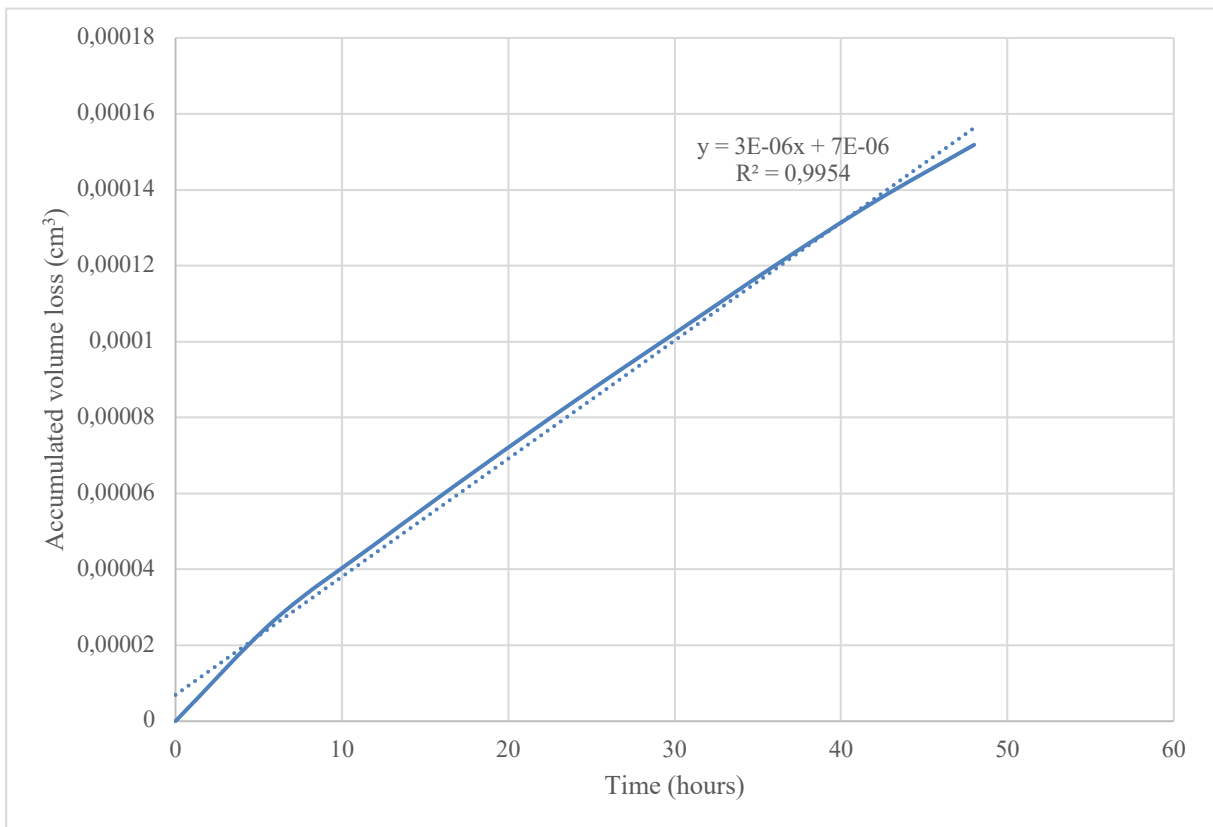


Fig. 5.35: Accumulated volume loss (cm^3) as a function of time (days) for sample 1 in 5 wt% NaCl with the corresponding trendline (stippled line) and function.

5.4.2 Anodic cyclic and cathodic potentiodynamic polarisation curves

The cathodic potentiodynamic polarisation curves obtained in 6 wt% FeCl₃ and 5 wt% NaCl for the 6Mo sample and the anodic CPP curve for A-316L obtained in 6 wt% FeCl₃ are presented in Fig. 5.36. As it can be seen from the figure, the anodic curve for A-316L and the cathodic curve for 6Mo in 6 wt% FeCl₃ intersects at 323 mV vs Ag/AgCl. The measured OCP for 6Mo in 6 wt% FeCl₃ is 703 mV and 200mV in 5 wt% NaCl. The OCP for A-316L is 301 mV, while after the scan is reversed the OCP approaches a lower value.

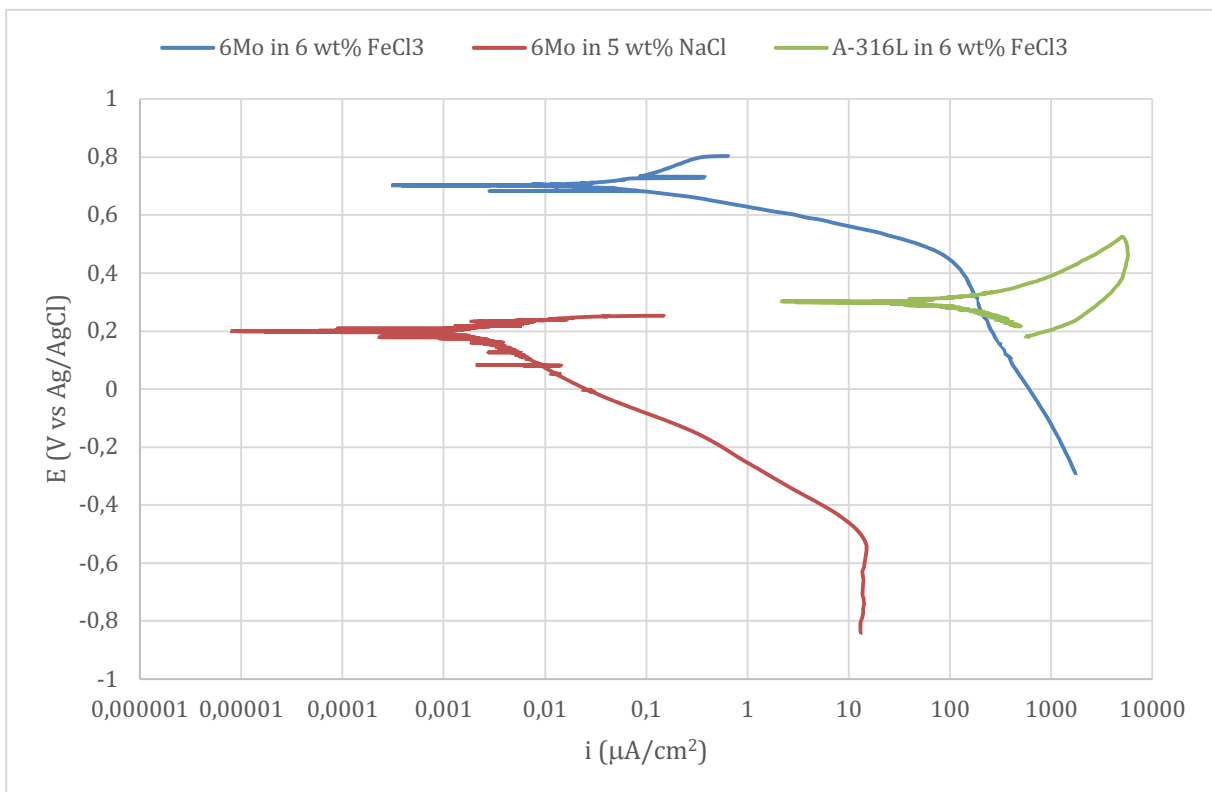


Fig. 5.36: Cathodic potentiodynamic polarisation curves for 6Mo conducted in 6 wt% FeCl₃ and 5 wt% NaCl, and the anodic CPP curve for A-316L conducted in 6 wt% FeCl₃.

5.4.3 Surface characterisation

The pits were investigated after the artificial pit experiments. Fig. 5.37 presents the samples prior to removing the coating and corrosion products can be observed from all pits. Fig. 5.38 presents the sample surfaces after the coating was removed. The coating hole was unchanged and not degraded due to the corrosion process, hence the pits propagated below the coating. Both sample 1 connected to an external cathode area of 36.8 cm² and sample 2 connected to an external cathode area of 6.30 cm² contained a large pit compared to the freely exposed sample 3.

Corrosion was not observed in the artificial pit on sample 3, but the area surrounding the pit below the coating experienced corrosion attacks with the appearance of uniform corrosion during the exposure. A great amount of corrosion products was observed inside the pit for sample 1 and 2 after removing the coating. The pits on sample 3 that can be observed outside the artificial pit in Fig. 5.38 are not from the artificial pit experiment. This sample was reused from an anodic CPP experiment due to lack of new A-316L samples.

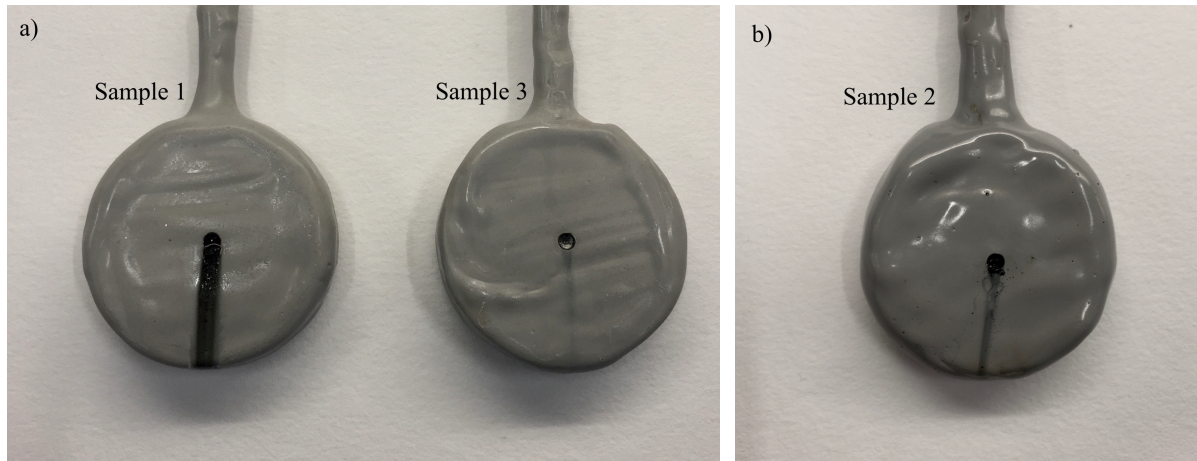


Fig. 5.37: The samples after the artificial pit experiment before cleaning and removing the coating. a) Sample 1 connected to an external cathode area of 36.8 cm^2 and the freely exposed sample 3, and b) sample 2 connected to an external cathode area of 6.30 cm^2 . Corrosion products in varying amount can be observed from the pits.



Fig. 5.38: The samples surfaces after the artificial pit experiment when the coating was removed.

The sample surfaces were investigated with IFM after the artificial pit experiment to obtain the actual volume loss and the pit size. The actual volume loss obtained for sample 1 connected to a 36.8 cm² 6Mo sample was 0.207 cm³, while sample 2 connected to a 6.30 cm² 6Mo sample was 0.072 cm³. Sample 3 which was freely exposed attained a volume loss of 0.0029 cm³. A summary of the calculated volume loss obtained from the galvanic current and actual volume loss in addition to the measured deepest point in the pits and the average pit diameter are provided in Table 5.10. The average diameter is presented since the pits were not entirely circular. The measured deepest point in the pit and average diameter were used to obtain the ratio pit depth to pit radius. Since the artificial pit on sample 3 was not attacked, the pit radius was not included, and the deepest measured point is in the attacked area surrounding the artificial pit.

Table 5.10: Actual volume loss and geometrical parameters of the pit on the samples after the artificial pit experiments.

Sample	Calculated volume loss (cm³)¹⁾	Actual volume loss (cm³)	Deepest point in the pit (mm)	Average pit diameter (mm)	Ratio pit depth to pit radius
1	0.241	0.207	4.684	15.78	0.6
2	0.0908	0.072	2.711	11.34	0.5
3	-	0.0029	0.286	-	-

1) Obtained from the galvanic current

The topography of sample 1, 2 and 3 with a scale bar presenting the depth distribution are presented in Fig. 5.39-Fig. 5.41, respectively. The black dots on the samples are spots the light source from the optical microscope did not reach and the colour rich area surrounding the samples are not signals from the sample surface.

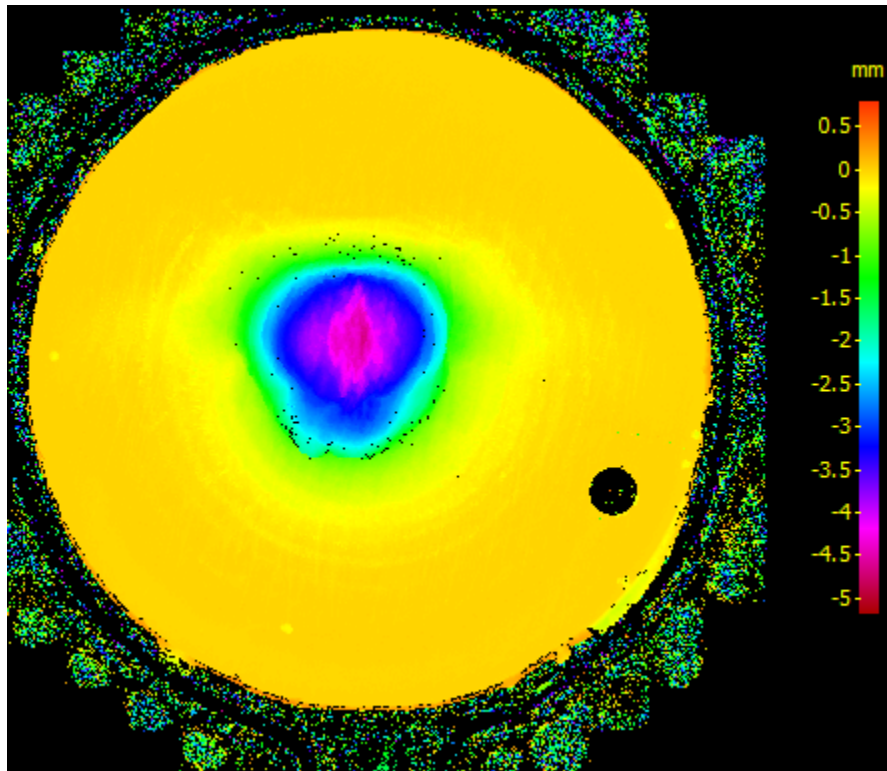


Fig. 5.39: Topography of sample 1 that was connected to an external cathode area of 36.8 cm² with the scale bar presenting the depth (mm) corresponding to the colours.

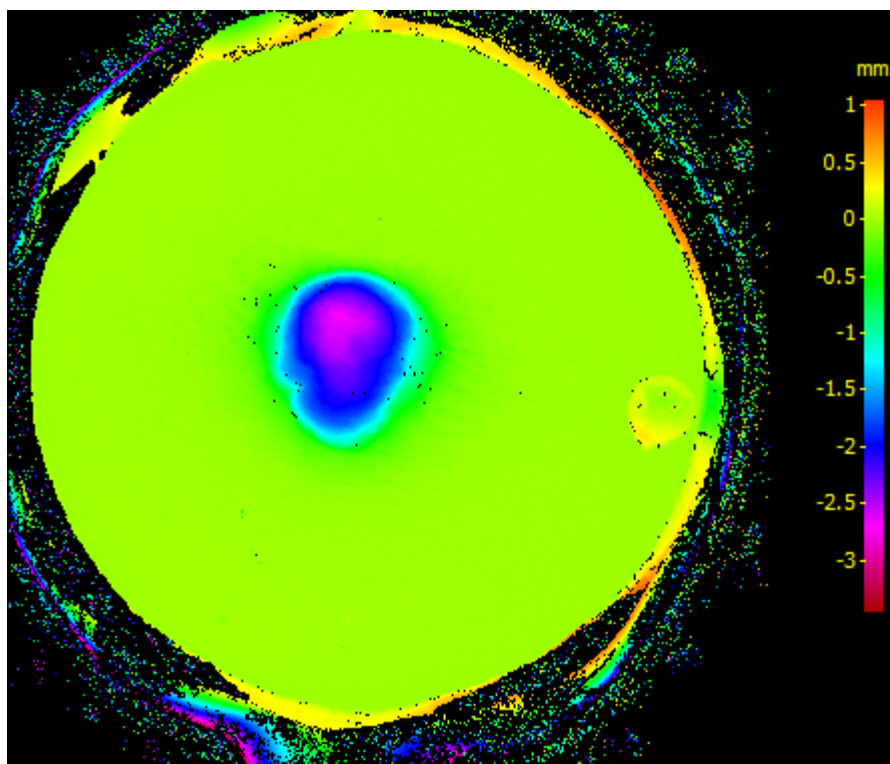


Fig. 5.40: Topography of sample 2 that was connected to an external cathode area of 6.30 cm² with the scale bar presenting the depth (mm) corresponding to the colours.

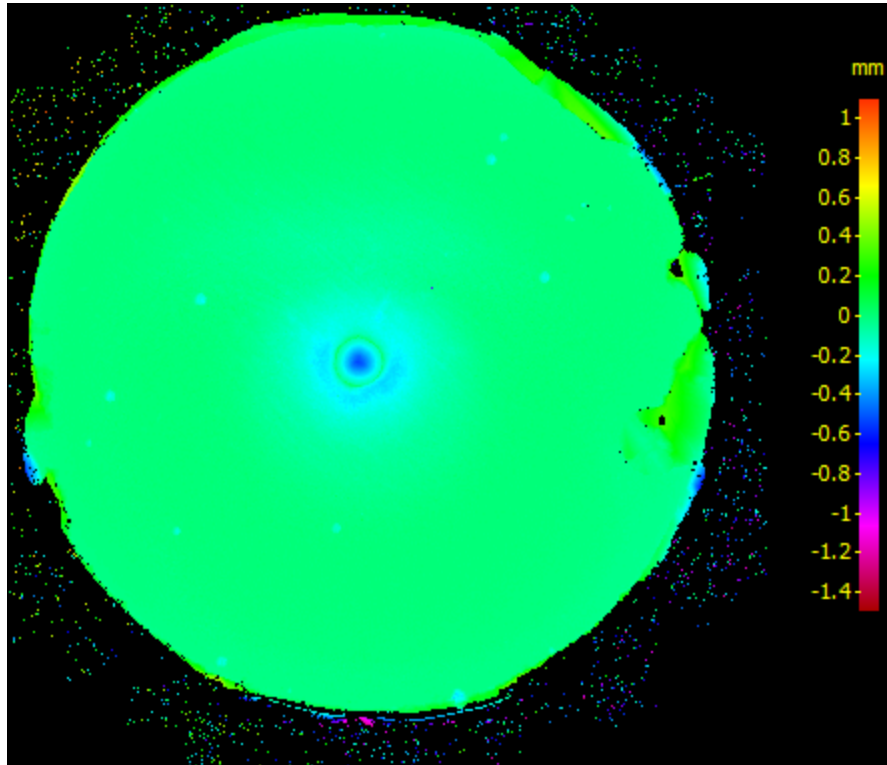


Fig. 5.41: Topography of sample 3 that was freely exposed with the scale bar presenting the depth (mm) corresponding to the colours.

The A-316L surface after anodic CPP in 6 wt% FeCl₃ at RT is presented in Fig. 5.42, obtained with 10X magnification. The average pit depth and diameter are 252.19 μm and 594.27 μm, respectively. Fifteen evidently pits can be seen from the figure, which were included when calculating average depth and diameter. Over the entire surface small pits of below 5 μm depth and 50 μm diameter was observed, but these were not taken into consideration when calculating average depth and diameter.

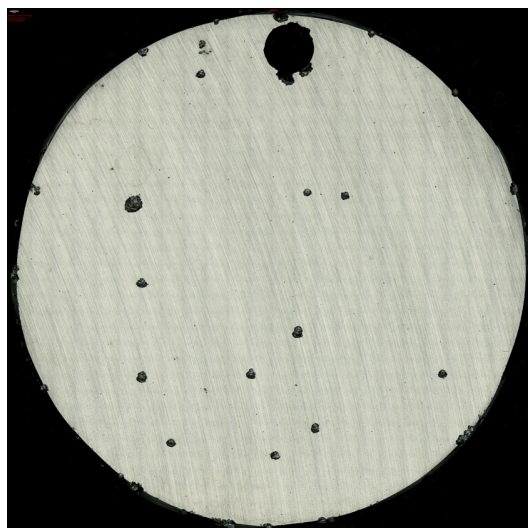


Fig. 5.42: The A-316L surface after anodic CPP in 6 wt% FeCl₃ at RT.

6 Discussion

The results from the experimental work presented in the previous chapter will be discussed thoroughly in this chapter. The anodic CPP, OCP measurements and exposure in a salt spray chamber conducted to investigate the effect of small changes in Mo content will be discussed separately in the three first chapters. Additionally, the result from the corresponding surface characterisation for each experiment will be discussed. The experimental results will then be compared to each other in a general discussion on the effect of Mo content. The results from artificial pit experiments will then be discussed, where the current and potential measurements, cyclic anodic and cathodic polarisation curves, and the surface characterisation are discussed in separate sections. A general discussion is then provided to compare the artificial pit experiments to normal operating conditions in marine atmosphere.

6.1 Anodic cyclic potentiodynamic polarisation

Anodic CPP curves were recorded to obtain OCP, E_{pit} , E_{rep} and i_{pass} for the test materials A-316L, B-316L, 317L and 316 Plus. The anodic CPP curves and the corresponding parameters were presented in Fig. 5.1-Fig. 5.4 and Table 5.1-Table 5.4, and will be discussed in this chapter. The difference in E_{pit} and E_{rep} for the test materials are of great importance when investigating the effect of Mo content. Increased corrosion resistance due to Mo or other alloying elements improving the resistance appear as higher E_{pit} and E_{rep} , and reduced i_{pass} on the anodic CPP curves.

To investigate the effect of Mo, the obtained E_{pit} as a function of Mo content at each test condition are presented in Fig. 6.1. E_{pit} generally decreases with increased temperature as it can be seen from the figure, which is consistent with the study done by Ramana et al.[56]. However, E_{pit} appears to be less affected by chloride concentration compared to temperature except for 316 Plus at 35°C. Since the curve was recorded only once, it can be measurement inaccuracy that causes the deviation for 316 Plus.

As can be seen from Fig. 6.1, the observed trend with respect to Mo content is similar for all test conditions. E_{pit} decreases with increased Mo content up to 2.548 wt% Mo, while E_{pit} increases significantly from 2.548 wt% to 3.06 wt% Mo. By considering the PREN value presented in Table 4.2, the corrosion resistance is expected to be ranked as 317L > B-316L > 316 Plus > A-316L. However, the E_{pit} trend does not represent the expected E_{pit} based on neither

PREN nor Mo content, which indicates that other alloying elements also influences E_{pit} . This effect is particularly significant for 316 Plus since E_{pit} is 210-399 mV more positive than B-316L depending on test condition.

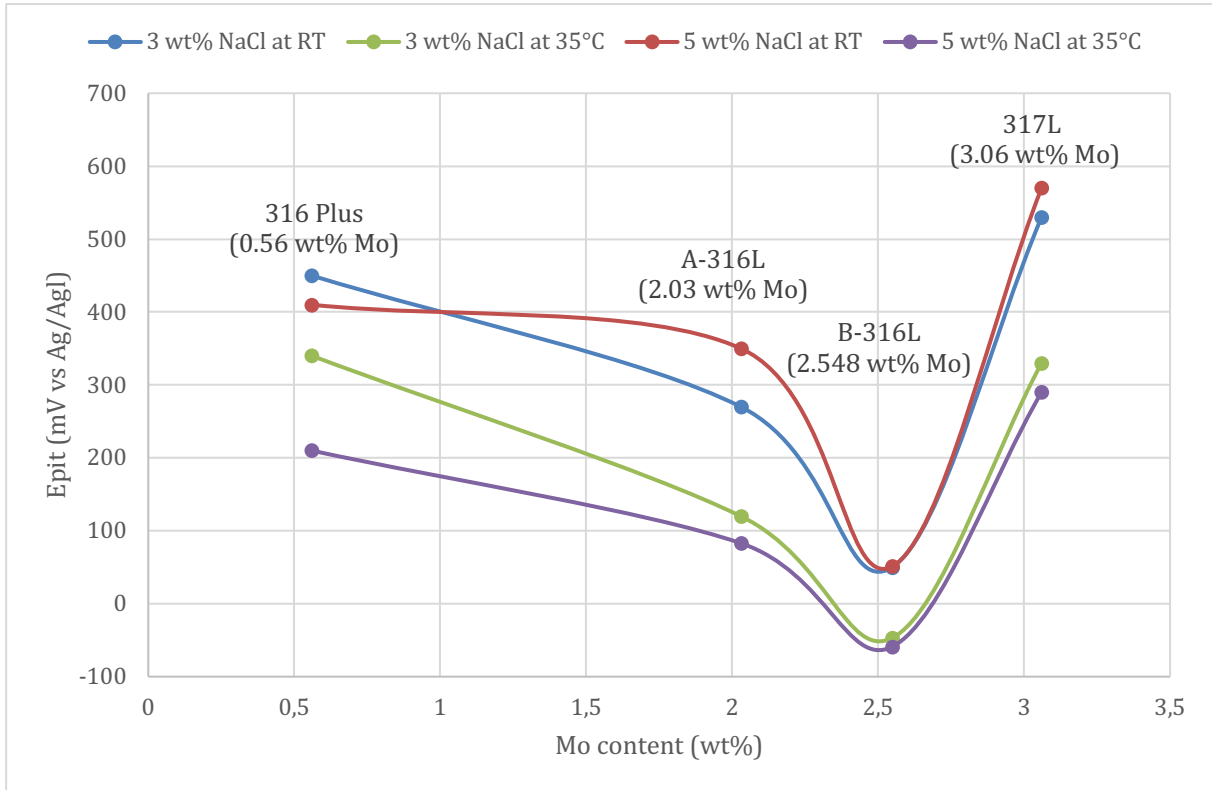


Fig. 6.1: E_{pit} obtained from the anodic CPP curves at each test condition as a function of Mo content.

The main difference between B-316L and 316 Plus regarding elements that may notably affect the corrosion properties besides Mo are the N and Cr content, where both are included in the PREN. The N content in 316 Plus is five times greater than B-316L even though the N content is small compared to the amount of the other elements affecting pitting and crevice corrosion resistance. Furthermore, the N content in A-316L is two times higher than for B-316L, while the Cr content is lower for A-316L. Even though B-316L has a higher Mo content, E_{pit} is 84-300 mV less than for A-316L depending on test condition. This indicates that N can affect E_{pit} , which was also observed by Loable et al.[6] and Kamachi and Dayal[76]. Furthermore, the small differences in Cr content among A-316L, 316 Plus and B-316L did not appear to affect E_{pit} as significantly as the differences in N content.

The corrosion resistance for 316 Plus is higher compared to A-316L according to the PREN presented in Table 4.2, which correlates well with the higher E_{pit} for 316 Plus at all test

conditions. However, compared to B-316L both 316 Plus and A-316L contains Cu which may additionally improve the corrosion properties[4, 12]. A combined effect of both N and Cu may cause E_{pit} for A-316L and 316L Plus to be higher than B-316L, which is the opposite of what should be expected since PREN has been demonstrated to increase with Mo content if the Cr content is similar[75]. Furthermore, from the study conducted by Liptakova and Zatkalikova[75], the greatest increase in E_{pit} with increasing Mo content for AISI 316Ti are when the Mo content increases from 2.82 to 2.88 wt% as it can be seen from Table 3.1. The alloy with 2.88 wt% Mo additionally contained N, which can be seen from Appendix A. This further emphasises the strong effect of N compared to Mo. Based on this and the obtained E_{pit} for A-316L, B-316L, 317L and 316 Plus presented in Fig. 6.1, it implies that the effect of N on PREN may be too conservative, and small amounts of other elements causes the predicted corrosion resistance ranking based on PREN to be incorrect.

Due to the small difference in N content between A-316L and 317L, these test materials are more correct to compare with respect to the effect of Mo content. E_{pit} for 317L increases 207-260 mV compared to A-316L depending on test condition. Thus, indicating a small positive effect of 1 wt% increased Mo content. An even greater increase of several hundred mV for E_{pit} at a similar increase in Mo content was observed by Upadhyay et al.[70] for AISI 316LN and 317LN. The N content in AISI 316LN and 317LN is similar as can be seen from Appendix A, thus differences in N content will not be a contributing factor for dissimilarities in corrosion properties. However, since AISI 316LN and 317LN contains initially more N than A-316L and 317L the synergy effect with N and Mo appear to be more pronounced at higher N contents.

317L contains a higher amount of Cr and Ni than A-316L, which may improve the passive film properties. Furthermore, the effect of small changes in Mo content on E_{pit} appear to be greater at higher Mo contents when comparing this result with the study done by Laycock and Newman[36]. Based on the result from analysing E_{pit} , changes in N content appear to have a greater effect on E_{pit} than changes in Mo content, and the ranking of the alloys with respect to E_{pit} are 317L > 316 Plus > A-316L > B-316L.

The obtained E_{rep} from the anodic CPP curves as a function of Mo content is presented in Fig. 6.2. A temperature dependent trend can be observed for E_{rep} , where E_{rep} at RT increases with Mo content from 0.56 to 2.03 wt%, while above 2.03 wt% E_{rep} appear not to be affected by

increased Mo content. Furthermore, at 35°C E_{rep} increases both above and below 2.548 wt% Mo.

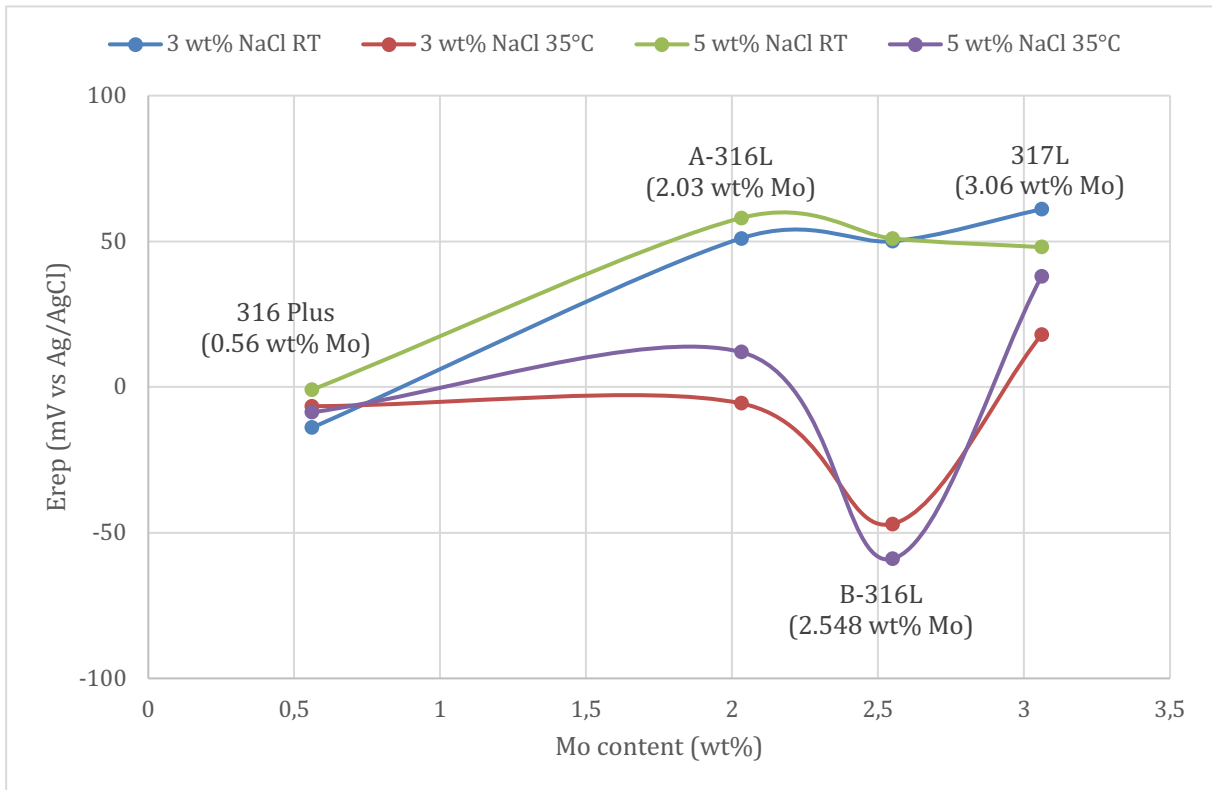


Fig. 6.2: E_{rep} obtained from the anodic CPP curves at each test condition as a function of Mo content.

E_{rep} for 316 Plus and 317L appear to be independent on temperature and chloride concentration since the difference between the test conditions is less than 50 mV. However, A-316L and B-316L appear to be slightly dependent on temperature, while the chloride concentration does not affect E_{rep} as much. The higher influence of temperature compared to chloride concentration is similar as for E_{pit} as discussed above. This indicates that the temperature has a slightly greater effect on the corrosion properties than chloride concentrations between 3 to 5 wt% NaCl for A-316L, B-316L and 317L, which correlates well with the observation done by Park et al.[61].

The temperature effect on E_{rep} is more pronounced for B-316L compared to the other test materials, which may have a correlation with the lower N content. As suggested by Loable et al.[6], N assist the repassivation process. However, in general the difference in E_{rep} lies in the range -59 mV to +61 mV, which are considered to be small and may not cause a significant difference in repassivation properties among the test materials. Thus, differences alloying

content between the test materials appear to not affect E_{rep} significantly, which is consistent with the observation regarding Mo content by Newman[73].

The OCP value of A-316L at test condition 1 and 2 is lower than expected. However, this does not appear to affect E_{pit} and E_{rep} since the results are in good agreement with the results obtained at test condition 3 and 4, and the overall trend for the test materials. On the contrary, a lower OCP causes the calculated PSF at these test conditions to be lower. Thus, the PSF at these test conditions causes an incorrect quantification of the pitting corrosion resistance. According to the calculated PSF presented in Table 5.1-Table 5.4, the test materials are not susceptible to pitting corrosion at these test conditions since the PSF is below 1. However, the OCP from the anodic CPP curves are recorded in a solution where oxygen is removed, which causes the measured OCP to be lower and hence the PSF.

Current transients between E_{rep} and E_{rep} can be observed on some of the anodic CPP curves, which implies metastable pitting. The presence of metastable pitting in the passive region indicates that the passive film is not stable at the potential where metastable pitting is occurring. Since larger current transients can be observed on both 316 Plus and 317L at 35°C compared to RT, it implies that the passive film is less stable at increased temperature. Metastable pitting can be observed on A-316L as well, however the magnitude varies and there is no specific correlation among the test conditions. Regarding i_{pass} it does not appear to be any clear trend with the test materials which can be correlated to the alloying elements. However, at each test condition the passive current density slope on the anodic CPP curves are less steep for B-316L, which implies less resistance to passive film dissolution compared to the other test materials.

6.1.1 Surface characterisation

When recording anodic CPP curves, pitting corrosion is forced to be initiated, except for cases where oxygen evolution occurs when the potential is above 1 V vs Ag/AgCl. In this experiment, pits are expected to be observed on the samples after anodic CPP since the curves contained a hysteresis loop. However, the extent of pitting corrosion on the samples may vary due to differences in corrosion properties. The sample surfaces were investigated to evaluate the difference in pitting corrosion attacks caused by the anodic CPP measurements, and to obtain a correlation between the pits that occurred according to the anodic CPP curves and the pits

that actually occurred. This section is based on the results presented in Table 5.6 and Fig. 5.5- Fig. 5.8.

Since B-316L contained a large amount of small pits that were not included in this investigation, the pit density is higher, while the average pit depth and diameter are less than presented in Table 5.6. However, since B-316L experienced the highest pit density, the lowest average diameter and the smallest average depth except for 317L, neglecting the small pits is justified when comparing the significance of the attacks on B-316L to the other test materials except for depth comparison with 317L.

According to the pit rating, the difference in the corrosion attacks are the pit density, while the depth and radius are similar. This arises since the size and depth on each sample are less than the smallest size and depth used to obtain a rating for the average size and depth. Thus, the pit rating indicates that the attack difference in terms of depth and size are not significant. Therefore, to compare the pitting corrosion attacks, the attacks will be further discussed by comparing the magnitude of the number of pits and the average pit diameter and depth.

There is a large scatter in the number of pits between the test materials, which is probably correlated to the passive composition since the experimental parameters except for the alloy composition is similar. This is confirmed by E_{pit} for the test materials as can be seen from Table 5.4. 317L and 316 Plus exhibited the most noble E_{pit} and the lowest number of pits compared to A-316L and B-316L. B-316L contained the highest number of pits which correlates well with the i_{pass} slope for B-316L that was less steep compared to the other test materials. Furthermore, the pit diameter is larger than the depth for each test material indicating that pits propagates in the lateral direction. The average pit diameter appears to increase with reduced number of pits, which may have a correlation with closely spaced pits sharing the available cathode area assuming that the pits grew simultaneously, thus the current density from each pit may decrease.

The number of pits on the test materials are probably related to the Mo content. As suggested by Ilevbare and Burstein[72] the Mo content can affect nucleation and metastable pitting. Thus, a reduced number of metastable events causes fewer pits that can become stable propagating pits. In this investigation this is correct when comparing A-316L or B-316L with 317L. The pit density on B-316L was greater compared to A-316L, but the depth and diameter of the attacks

were larger on A-316L. This indicates that A-316L has a higher resistance to initiation, however once initiated the pits can grow larger at similar conditions possibly due to higher current densities from each pit. On the contrary, the pits on A-316L and 317L are of similar average diameter but the pits on 317L are less deep. As it can be seen from Fig. 5.5 and Fig. 5.7, the pits on A-316L are more oval, while the pits on 317L are more circular. Since the pit diameter measured were the largest for each pit, the surface area of the pits is slightly larger on 317L. Based on this, Mo appears to affect the pit depth since the depth decreases with increasing Mo content independent of N content except for 316 Plus.

The significance of the attacks on A-316L, B-316L and 317L correlates well with the corrosion resistance based on E_{pit} from the anodic CPP curves. However, the deviation for 316 Plus is probably due to the high N content compared to the test materials. Due to the low Mo content in 316 Plus, N appears to significantly influence the pit density at sufficient high N content.

The pits on the lateral edges were not considered in this investigation, however the lateral edges can be more susceptible to pitting corrosion due to more initiation sites. There may be two possible reasons for pronounced attacks on the lateral edges. During sample preparation the lateral edges are more difficult to grind due to the curvature on the circular samples A-316L, 317L and B-316L, which can cause a more uneven surface compared to the top and bottom. Another possibility is more containments on the lateral edge caused by the nature of solidifying during steel production. The steel solidifies at the surface first and in the middle last, which can cause more containments on the lateral edges of the samples since all test materials except for B-316L were cut from plates.

6.2 Open circuit measurements

This section discusses the OCP measurements presented in Fig. 5.9-Fig. 5.12, which were obtained in 5 wt% NaCl at 35°C for 14 days and at RT for two days. Simultaneously, oxygen purging was conducted the last three days to investigate if the concentration was below saturation. OCP measurements are of great importance since the materials can be ranked in terms of corrosion resistance. If the OCP is higher than E_{pit} obtained from anodic CPP curves for the material of interest presented in Table 5.4 at 35°C or Table 5.3 at RT, stable pitting can occur. Stable pitting appears on OCP curves as potential drops that lasts longer than a few seconds. Metastable pitting can occur if the OCP is above the potential at which metastable pits

can be formed from anodic CPP values as presented in Table 5.5. However, in general metastable pitting can occur if the OCP are between E_{pit} and E_{rep} .

Stable OCP values below E_{pit} are observed for 317L even though the OCP values are above E_{rep} and metastable pitting can occur at both temperatures. Since OCP became higher for 317L as oxygen purging was performed it implies that the oxygen concentration near the surface increased. On the contrary, B-316L and 316 Plus exhibited noisy values that may be attributed to an unstable passive film causing metastable pits to be initiated and repassivated. Thus, the conditions were not sufficient to cause stable pit propagation. Metastable pitting can be confirmed by the change in OCP trend to a more stable value when the temperature was decreased to RT.

The peaks on the A-316L curve are above E_{pit} at 35°C and below E_{pit} at RT. However, at RT the OCP is above the potential where metastable pitting can occur. At 35°C some of the potential drops for A-316L lasted several days, which means that stable pits initiated and grew as stable pits a few days before repassivation. Compared to the other test materials, pit propagation is most significant for A-316L. As oxygen purging started the potential drops became more frequent and smaller. This may have a correlation with oxygen purging causing stirring in the solution such that the more aggressive electrolyte at pitting corrosion initiation sites is diluted. Furthermore, as the temperature was decreased to RT a higher but less noisy OCP is observed, which indicate that the passive film became more stable as for 317L through the whole exposure period.

The curve peaks are above E_{pit} for B-316L throughout the test at both temperatures. The size of the potential drops for B-316L increased throughout the test, oscillating around an increasing mean potential value. This may have a correlation with reduced protectiveness of the passive film as the passive film adapted to the environment during the test. However, as the temperature was decreased to RT, the potential drops lasted a longer time indicating that pits started to propagate as stable pits and repassivated. Both changes in temperature and oxygen concentration can affect OCP. As it can be seen from Fig. 6.1, E_{pit} for B-316L was least affected by temperature compared to the other test materials, and the change was not significant. Therefore, stable pitting may be explained by having a correlation with increased amount of oxygen that raised OCP exactly sufficient to obtain stable pitting for a longer period of time.

The OCP peak values of 316 Plus are well above the potential where metastable pitting can occur and around E_{pit} at 35°C, thus metastable and stable pitting can occur at this temperature. This noisy behaviour correlates well with the potentials where metastable pitting is observed on the anodic CPP curve for 316 Plus as can be seen from Fig. 5.4. The potential drops generally increase rapidly with time. However, some of the drops attain at a low value for a noticeable period of time indicating stable pit propagation. Compared to A-316L, the stable pit propagation has a significantly shorter lifetime for 316 Plus. This can be explained by the potential the pits grew at relative to E_{pit} for the respective material. The stable propagating pits before re-passivating on A-316L propagated at a higher potential above E_{pit} compared to 316 Plus. As the temperature were decreased to RT, OCP falls below E_{pit} to around the potential where metastable pitting starts and appear to stabilise more for 316 Plus.

Based on this, one can conclude that the passive film on 317L is more stable at this test condition compared to the other test materials. Both B-316L and 316 Plus exhibit unstable passive films and are susceptible to stable pitting corrosion at 35°C. However, at RT only B-316L and A-316L are susceptible to stable pitting corrosion. From the OCP measurements the materials can be ranked as 317L > 316 Plus > B-316L > A-316L at 35°C, while A-316L exhibits a higher corrosion resistance than B-316L at RT.

6.2.1 Surface characterisation

This section is based on the surface characterisation after OCP measurements, where the purpose is to compare the observations on the sample surfaces to the OCP measurements. Pits were observed on A-316L, B316L and 316 Plus, while 317L did not contain pits as can be seen from chapter 5.2.1.

The pits on A-316L correlate well with observed stable pitting from the OCP measurement presented in Fig. 5.9, which demonstrates that A-316L is susceptible to pitting corrosion at 35°C in 5 wt% NaCl. Accordingly, a positive effect of increased Mo content can be observed when comparing A-316L to 317L. The absence of corrosion attacks on 317L additionally demonstrates that the small (0.01 wt%) N increase in A-316L compared to 317L does not significantly affect the corrosion properties compared to the Mo content at this test condition.

The blue and brown coloured spots surrounding small pits on B-316L contained a smaller Fe amount and a higher amount of Mo and Cr compared to the bulk surface as presented in Fig. 5.15-Fig. 5.17. This indicates that the spots are areas enriched in Mo and Cr. The lower Fe content is probably due to preferential dissolution of Fe at the pit site. Thus, the colour may arise due to composition changes at the surface around the pit. The EDS point analyse provides information about the elements present and not which compounds. To investigate the occurrence of these spots it is necessary to perform XPS to obtain information of the compounds present, which is out of the objective of this thesis. However, the depth of the pits on B-316L can correspond to the surface roughness due to the micron size, which implies that this is not well developed pits. Hence, there is a possibility that these are pits that only reached the metastable stage before repassivation. However, these pits and the visually indications of pits on the lateral edge may imply that the passive film on B-316L was not stable during the OCP measurement.

As discusses in chapter 6.2, 316 Plus exhibited indications of both pits that repassivated at the metastable stage and stable pit propagation. These observations coincide with the pits on 316 Plus through the IFM and SEM analyse. As can be seen from Fig. 5.18 and Fig. 5.19, grains in the microstructure appear to have dissolved from the surface. This implies pit initiation and propagation during the OCP measurement. However, these pits are not as developed as the larger stable propagated pits from the anodic CPP measurements which can be seen from Fig. 5.8. Hence, these pits probably repassivated shortly after initiation. The pit presented in Fig. 5.20 is an indication of metastable pitting during the OCP measurement. This pit appears to have initiated at the grain boundary, but repassivated before the entire grain dissolved. Thus, the noisy OCP measurement is probably due to an unstable passive film causing pitting initiation and repassivation during the OCP measurement.

6.3 Salt spray test

This section is based on the results in chapter 5.3 from the salt spray exposure and the recorded anodic CPP curves of the coated samples. The differences in corrosion resistance among the test materials will be discussed in terms of weight loss and visual appearance, which can give an indication if dissimilarities in alloying content affects the corrosion properties.

Generally, to obtain a more reliable result for the weight loss measurement several samples should be used such that the standard deviation can be calculated. In this exposure the different variables (mineral wool, tilted and not tilted samples) can affect the weight loss, hence it may be incorrect to use the standard deviation during the evaluation. Furthermore, since the samples were coated the coating can affect the weight loss due to water adsorption of the coating. This can cause the measured weight after the exposure can be higher than the actual weight loss due to corrosion. Therefore, differences in sample weight loss will not be accounted for in the same degree as the visual appearance and the IFM analyse of the samples that exhibited crevice corrosion attacks.

As it can be seen from Table 5.7, one sample of both A-316L and 317L did not visually contain corrosion attacks. By comparing the weight loss per unit area of these samples to the samples that exhibited pitting corrosion attacks, it can be seen that the weight loss per unit area is of similar magnitude. This implies that the observed pitting corrosion attacks did not contribute significantly to the total weight loss. However, the weight loss may have been caused by more uniform corrosion.

The crevice corrosion attacks on A-316L, B-316L and 316 Plus appeared as uniform corrosion where the attacks seemed similar. However, crevice corrosion occurred on A-316L before attacks were observed on B-316L and 316 Plus. Since crevice corrosion attacks were not observed on 317L, it indicates that 317L has a higher crevice corrosion resistance than A-316L, B-316L and 316 Plus at the environment in the salt spray chamber. As can be seen from Fig. 5.23-Fig. 5.25, a larger area below the coating was attacked on A-316L and B-316L compared to 316 Plus, which indicates a higher resistance to crevice corrosion propagation for 316 Plus. The higher resistance to propagation for 316 Plus may be attributed to the higher N content, which can affect the anodic dissolution kinetics as suggested by Newman and Shahrabi[77]. The weight loss per unit area on the samples subjected to crevice corrosion was higher for A-

316L and B-316L compared to 316 Plus as can be seen from Table 5.7 and Fig. 5.22, which further emphasises a higher corrosion resistance for 316 Plus.

However, the attack significance additionally depends on the propagation time and the propagation time may have been longer for A-316L than 316 Plus. It is not known if crevice corrosion initiated on B-316L or 316 Plus first and if the corrosion attacks repassivated before the test was completed. Additionally, crevice corrosion was only observed on one of each sample. Based on this, the crevice corrosion properties appear not to be significantly different for A-316L and B-316L. 316 Plus may exhibit a slightly higher crevice corrosion resistance while 317L are the most resistant alloy.

Small and insignificant pitting corrosion attacks were observed on the majority of the samples as presented in Table 5.7. This can be related to either the temperature in the salt spray chamber being too low to obtain well developed attacks or too short exposure time. Too low temperature is confirmed by Kopliku and Mendez[2] that needed to increase the salt spray chamber temperature to obtain well developed attacks on AISI 316L and 317LMN. Thus, higher temperatures than 35°C in the chamber are necessary to obtain well developed pitting corrosion attacks on the test materials with 5 wt% NaCl as salt spray solution.

The mineral wool placed on the samples did not notably affect the weight loss per unit area except for B-316L, as can be seen from Fig. 5.22. The higher weight loss per unit area for B-316L is probably not caused only by the mineral wool since corrosion attacks were observed underneath this sample as well. Furthermore, the thick water layer on the samples that were not tilted appear not to have a major effect on the weight loss per unit area when comparing these samples to the samples with mineral wool on the surface. Based on merely the visual observation and the weight loss per unit area, the pitting corrosion resistance appears to be similar for the test materials at a salt spray chamber temperature of 35°C.

The surface roughness does not appear as more important than exposure time in this case since only one of the not grinded samples exhibited a significant corrosion attack compared to the other not grinded samples. However, if the surfaces on the coated samples were rougher crevice corrosion could have developed on a greater number of samples. Rougher surfaces can allow easier penetration of water below the coating, and hence easier crevice corrosion initiation.

E_{pit} and E_{rep} measured for the creviced samples presented in Table 5.8 are similar to the potentials measured for samples without coating presented in Table 5.4, thus crevice corrosion did not occur during the anodic CPP. Therefore, it was not possible to obtain the critical potentials for crevice corrosion. The lack of crevice corrosion is possibly due to a too tight crevice that prevented electrolyte from entering the crevice. A too tight crevice may explain why crevice corrosion was only initiated on one of each sample that appeared to be subjected to crevice corrosion at the test environment in the salt spray chamber. On the contrary, the mineral wool was expected to cause crevice corrosion due to a less tight crevice compared to the coating. Since the attacks on the samples with mineral wool were similar to the attacks on the samples without mineral wool, it implies that the crevice created by the mineral wool was not sufficient to cause oxygen depletion which promotes crevice corrosion initiation.

6.4 The effect of molybdenum content – general discussion

Based on the E_{pit} from the anodic CPP curves, OCP measurements and the salt spray exposure, 317L appears to exhibit the highest corrosion resistance of the test materials, which is in accordance with the calculated PREN presented in Table 4.2. Thus, this indicates that a positive effect on the corrosion resistance is obtained by increasing the Mo content to 3 wt%. Furthermore, based on E_{rep} from the anodic CPP curves the repassivation properties of the test materials are similar. Thus, the difference in alloying content among the test materials are important for pitting and crevice corrosion initiation.

Since 317L has a higher alloying content of the elements that increases the corrosion resistance, the CPT can be higher for 317L than A-316L and B-316L. However, the CPT for 317L is probably below the selected test temperature of 35°C for the OCP measurement and salt spray test since indications of pitting corrosion attacks were observed at the salt spray test as for the other test materials. Probably a higher chloride concentration than 5 wt% is necessary to cause attacks similar to the other test materials on 317L during the OCP measurement due to higher passive film stability.

The corrosion resistance appears to be higher for 316 Plus than A-316L and B-316L from the anodic CPP curves based on E_{pit} , OCP measurements and the salt spray exposure, which implies that low Mo content with high N content results in increased corrosion resistance even though the Ni content is lower. Hence, lower Mo content can be used without decreasing the corrosion

resistance when the alloy contains a sufficient amount of N. However, in general 316 Plus, A-316L and B-316L are not considered to be corrosion resistant at 35°C with a 5% NaCl solution both immersed and at atmospheric conditions based on the experiments performed in this master thesis.

The OCP obtained from the anodic CPP curves presented in Table 5.4 are lower than the obtained OCP from the OCP measurements presented in Fig. 5.9-Fig. 5.12 for each test material at 35°C. This is due to exposure in a more oxidising environment due to the presence of oxygen in the electrolyte at the OCP measurements. Hence, the PSF calculated by using the OCP obtained from the anodic CPP curves does not represent the actual pitting corrosion susceptibility.

From the studies done by Jung et al.[14] and Bastidas et al.[15], the passive film formed on AISI 316L is thicker under wet-dry cycling than immersed conditions. This indicates that the corrosion resistance can be higher under atmospheric conditions than immersed due to a thicker passive film. Furthermore, the approximately similar passive film thickness for AISI 316L and 304 in the study done by Jung et al.[14] indicates that the difference in alloying content among these materials does not affect the passive film thickness. Thus, the passive film composition may be more important than the thickness with respect to differences in corrosion resistance.

According to the anodic CPP curves A-316L exhibits a higher corrosion resistance than B-316L, while B-316L appears to have the highest corrosion resistance from the OCP measurements at 35°C. This implies that evaluating the corrosion resistance based on only anodic CPP curves can give an incorrect evaluation when comparing similar alloys. Furthermore, from the anodic CPP curves obtained in 5 wt% NaCl at 35°C and the OCP measurements, the test materials are ranked equal except for A-316L and B-316L. This difference in ranking can have a correlation with similar corrosion properties of A-316L and B-316L, which was observed with the salt spray test. Thus, the studies regarding the effect of Mo content at immersed conditions can be used to evaluate the effect of Mo at marine atmospheric conditions.

6.5 Artificial pit experiments

This section discusses the potential measurements of the A-316L artificial pit samples presented in Fig. 5.28-Fig. 5.31, which were conducted in 6 wt% FeCl₃. Sample 1 and 2 were connected to a 6Mo sample that served as cathode area and sample 3 was freely exposed. Additionally sample 1 and 3 were exposed in 5 wt% NaCl after 6 wt% FeCl₃, which will be used to discuss the cathodic efficiency and the effect of electrolyte. The galvanic current measurements presented in Fig. 5.32 and Fig. 5.33 for sample 1 and 2 are discussed in this chapter as well. Both the potential and galvanic current measurement are of great importance when evaluating pit propagation, the effect of cathode area and the effect of electrolyte in terms of corrosion rate and repassivation. Increased potential for an active pit and increased cathodic efficiency implies higher corrosion rate, and the pit continues to propagate if a galvanic current is measured.

During the exposure all samples exhibited a corrosion attack according to the surface characterisation presented in chapter 5.4.3. As it can be seen when comparing the potential on sample 1, 2 and 3 in Fig. 5.28, Fig. 5.29 and Fig. 5.31, the pits on sample 1 and 2 which were connected to an external cathode grew at a more positive potential than the pit on sample 3 that was not connected to an external cathode. Thus, the corrosion rate is higher due to connecting the samples to an external cathode area, which should be expected for an active pit.

The potential on sample 1 and 3 drops when the electrolyte was changed from 6 wt% FeCl₃ to 5 wt% NaCl. This arises due to exposure in a less oxidising environment. Since a galvanic current was still measured between the artificial pit and external cathode as can be seen from Fig. 5.32, the pit on sample 1 continued to propagate when immersed in 5 wt% NaCl. For sample 3 it is not possible to determine if the pit repassivated when immersed in 5 wt% NaCl since the polarisation behaviour of A-316L at the potential attained in 5 wt% NaCl is not known.

However, for sample 1 the galvanic current and thus the corrosion rate was significantly lower in 5 wt% NaCl compared to 6 wt% FeCl₃. This can also be seen by comparing the slope of the curve for sample 1 in Fig. 5.34 and Fig. 5.35, which is significantly less in 5 wt% NaCl. This demonstrates that the cathodic efficiency is significantly lower in 5 wt% NaCl. As can be seen from Eq.2.6, the pit can repassivate if the current decreases sufficiently since the depth does not decrease. Hence, the current generated and subsequent metal hydrolysis were still sufficient low to maintain the pit in the active state as the electrolyte was changed.

The effect of changing the electrolyte is probably related to the pit propagation before changing the electrolyte. As the pit propagates the diffusion path increases, hence the pit propagation time affect the minimum current necessary to sustain stable pit propagation. This means that if the electrolyte was changed after a few days, the pit response on changing the electrolyte could be repassivation due to the shorter diffusion path. Another factor that helps maintain the aggressive electrolyte inside the pit is the corrosion products that provide an additional barrier, which the pit stability product does not consider. The artificial pit design constrains diffusion out of the pit since the hole in the coating is constant during propagation of the pit. Hence, the amount of corrosion products may increase with time as the corrosion process proceeds.

From Fig. 5.32 and Fig. 5.33 the galvanic currents are initially in the order of 3.5 and 2 mA for sample 1 and 2, respectively. This correspond to current densities from the pit of approximately 70 mA/cm² for sample 1 and 40 mA/cm² for sample 2 at the initial pit surface area of 0.05 cm². Thus, the corrosion rate is high. Since a galvanic current was measured for both samples throughout the duration of the test period the pit continued to propagate and did not reach a limited size due to repassivation. Furthermore, the galvanic current with time for sample 1 is similar to the current with time evolution observed by Heurtault et al.[78] on AISI 316L as presented in Fig. 3.5. On the contrary, sample 2 exhibits a less stable galvanic current with time evolution compared to sample 1. The deviation for sample 2 can have a correlation with a smaller available cathode area causing the galvanic current to be less stable. Thus, the cathode reaction appears to be more stable on sample 1.

The galvanic current from the pit is higher for sample 1 connected to a cathode area of 36.8 cm² than sample 2 connected to a cathode area of 6.30 cm². A higher galvanic current arises due to the differences in cathode area since the ratio of cathode area to anode area are larger for sample 1 than sample 2. As the cathode area increases, the driving force for the corrosion process increases since the 6Mo plate is less polarised. Hence, the corrosion rate increases and sample 1 should attain a higher coupling potential than sample 2. From the coupling potentials presented in Fig. 5.28 and Fig. 5.29 this is not the case, which can be caused by inaccuracy in the measurements. However, even though sample 1 experienced higher currents, the observed magnitude of the current on both samples demonstrates that at even small cathode areas can cause significant corrosion rates when the cathode is sufficient effective.

The current for sample 3 can be estimated from Faradays second law presented in Eq.2.7 and the measured volume loss presented in Table 5.10. By assuming a constant current throughout the exposure and neglecting the volume loss contribution in 5 wt% NaCl, the current from the pit on sample 3 is 0.04 mA. Compared to sample 1 and 2, this current is significantly lower. The cathode area for sample 3 is inside the pit since sample 3 was not connected to an external cathode. Hence, the smaller current for sample 3 arises due to a smaller cathode area and the lower driving force due to A-316L as cathode area compared to 6Mo as cathode area.

The cathode area affects the accumulated volume loss as can be seen when comparing the slope of the curves for sample 1 and 2 in Fig. 5.34. The accumulated volume loss for sample 1 is higher throughout the experiment than for sample 2. This implies that the available cathode area is important for the propagation rate. To further investigate the cathode area significance the function for accumulated volume loss with time presented in Fig. 5.34 for sample 1 and 2 can be considered. By using the function for accumulated volume loss with time for sample 2, the number of days before sample 2 attains the equal volume loss as sample 1 exhibited the entire exposure time can be estimated. Approximately 40 exposure days are necessary for sample 2 to obtain the similar volume loss as sample 1 exhibited during the 24 days of exposure. Hence, the cathode area size in 6 wt% FeCl₃ significantly affects the corrosion rate.

Volume loss estimations based on the functions for sample 1 and 2 presented in Fig. 5.34 for longer periods of time may not be realistic since the curve probably does not increase linearly infinitely with time. At some point the corrosion products formed inside the pit may constrain diffusion of ions out from the pit and into the pit. The limited ionic path may cause the cathode reactions that balances the anode reactions to occur only inside the pit. Hence, the available cathode area can be reduced and thereby the corrosion rate.

Hydrogen reduction (Eq. 2.4) as cathode reaction inside the pits may occur due to the low pH of 6 wt% FeCl₃ as presented in Table 5.9. Compared to oxygen, hydrogen as cathode reaction consumes fewer electrons per reaction as can be seen from Eq. 2.2 and 2.4, which can decrease the corrosion rate. Additionally, hydrogen bubbles inside the pit due to hydrogen reduction can increase the ohmic resistance of the electrolyte under atmospheric conditions, which in turn limits the cathode area and increases the ohmic potential drop for current from the pit and to the external cathode surface.

Changes in pH during the artificial pit experiment can give an indication if hydrogen reduction occurred. The pH after the experiment decreases slightly for sample 1 and 3, however this small decrease is probably due to a small temperature difference when measuring the pH. On the contrary, the pH decreases for sample 2 which indicates hydrogen consumption during the experiment. This implies that hydrogen as cathode reaction is more significant when the available cathode area is small. Since the pH in the solution is low, hydrogen reduction can occur both inside the pit and on the external cathode. Due to the lower available cathode area for sample 1 compared to sample 2, this may imply that hydrogen as cathode reaction is more important at small cathode areas. Possibly hydrogen reduction may occur more significantly inside the pit for sample 2 since the available external cathode area is too small to balance the anodic current.

6.5.1 Anodic cyclic and cathodic potentiodynamic polarisation curves

Since the cathode area is 6Mo and not AISI 316L in these experiments the potential drop occurring between the anode and cathode presented as in Fig. 2.6 can be affected. The measured OCP for A-316L in 6 wt% FeCl₃ from Fig. 5.36 is 301 mV vs Ag/AgCl, while the OCP on artificial pit sample 3 is approximately -100 mV vs Ag/AgCl as can be seen from Fig. 5.31. This OCP difference arises since the surface was passive when OCP was measured from Fig. 5.36, while the surface of sample 3 was in the active state. Thus, this potential difference indicates that the potential drop between the passive surface (cathode) and the active surface (anode) for A-316L in 6 wt% FeCl₃ can be around 400 mV vs Ag/AgCl. Compared to 6Mo as external cathode, the potential drop for A-316L as cathode and anode is approximately halved. Thus, the obtained volume loss for sample 1 and 2 are expected to be higher due to a higher corrosion rate than under normal circumstances where both anodic and cathodic reactions occurs on A-316L.

The OCP decreases after the anodic CPP curve for A-316L in 6 wt% FeCl₃ is measured as it can be seen from Fig. 5.36. This decrease is caused by the changes in the surface during the scan and implies that the OCP decreases when the surface has been subjected to corrosion. Furthermore, A-316L is in the active state in 6 wt% FeCl₃ since as the potential increases there is no passive current density. Thus, the passive film is present as the sample is immersed, but dissolves shortly after. A weakness with this curve is that the reversed scan should have lasted longer to obtain the cathodic part of the curve as well. The cathodic part of the curve shows at

which potential A-316L is immune to corrosion in this electrolyte, and thus the lowest possible potential where the pit can continue to propagate.

The intersection between the anodic A-316L curve in the forward scan and the cathodic 6Mo curve represents the coupling potential and the corrosion current density. However, the intersection is valid when the cathode and anode area is similar. Since the external cathode area is larger than the artificial pit, the 6Mo curve should move further towards higher current densities as the ratio of cathode to anode area increases. Thus, the obtained galvanic current density is slightly higher under the artificial pit experiments compared to the current density at the intersection of the cathodic and anodic polarisation curves.

The cathodic curve for 6Mo increases towards more positive potentials and current densities in 6 wt% FeCl₃ electrolyte compared to 5 wt% NaCl, which further emphasises that the cathodic efficiency is lowest in 5 wt% NaCl. The cathodic efficiency in 5 wt% NaCl is more representative to what can be expected under atmospheric conditions. However, other factors such as potential drop and electrolyte size affects the cathodic efficiency under atmospheric conditions as well. Since the electrolyte is a thin water film, the cathode area can be smaller compared to the cathode area under immersed conditions. When the cathode is immersed, the whole area acts as cathode, while under atmospheric conditions ohmic drop in the electrolyte can cause the effective cathode to be smaller. Thus, this further emphasises that the corrosion rate is lower under atmospheric conditions than immersed.

6.5.2 Surface characterisation

This section discusses the surface characterisation after the artificial pit experiment where the theoretical volume loss is compared to the actual volume loss and the geometrical pit parameters are discussed.

The pit on sample 1 propagated into a larger and deeper pit than on sample 2 as can be seen from Fig. 5.38-Fig. 5.40. This correlates well with the theoretical volume loss as a function of time calculated according to Faradays second law presented in Fig. 5.34. Furthermore, since the actual volume loss and the calculated volume loss are of similar magnitude as can be seen from Table 5.10, it implies that using Faradays second law to estimate volume loss for this experiment is valid. When using the galvanic current to estimate volume loss by Faradays

second law the cathodic reactions inside the pit is not considered. However, since the actual volume loss is not larger than the calculated volume loss it implies that the current due to cathodic reactions inside the pit is insignificant.

Since the galvanic current the first days for sample 2 was assumed to be the average of the galvanic current the last ten days it causes some uncertainties on the calculated volume loss. If higher current densities than the average occurred the first days, the calculated volume loss can be higher.

The radius is larger than the depth for sample 1 and 2 as can be seen from Table 5.10, which correlates well with the investigation by Heurtault et al.[78] and Aouina et al.[79] for AISI 316L. This indicates that pit propagation in the lateral direction is more pronounced, which probably has a correlation with a shorter diffusion path compared to the pit bottom. In general, larger pit diameter than the depth was observed after at the anodic CPP and OCP measurements conducted in this master thesis as well. Thus, pits on AISI 316L propagates into pits with a larger diameter than depth. However, as presented in Table 5.10, the ratio of pit depth to pit radius is 0.6 and 0.5 for sample 1 and 2, respectively. This is greater than observed by Heurtault et al.[78], which is probably correlated to the different experimental set up and electrolyte used compared to the artificial pit experiments.

Furthermore, the radius appear to be dependent on the potential drop between the anode and cathode from the study done by Heurtault et al.[43] since the radius increased with applied potential as can be seen from Fig. 3.6. This can be explained by the difference in potential drop between the anode and cathode at different applied potentials. At higher applied potentials in the passive domain the potential drop between the anodic dissolving pit and the passive surface increases, which in turn lead to a larger pit radius due to a higher corrosion rate. Hence, the pit radius may increase as the driving force increases.

The artificial pit on sample 3 was not attacked, while the adjacent area below the coating was attacked. This indicates that the artificial pit served as cathode, while the area below the coating served as anode for sample 3. As it can be seen from the attack size on the samples in Fig. 5.39-Fig. 5.41, the attack on sample 3 is insignificant compared to sample 1 and 2. This further emphasises that the cathode area influences the attack significance as was discussed above due to the smaller current from sample 3. Additionally, the less significant attack on sample 3

implies that the corrosion rate was lower compared to sample 1 and 2 due to a smaller potential drop between the anode and cathode as was discussed in chapter 6.5.1.

The pits on A-316L which can be seen from Fig. 5.42 confirms that the surface exhibited corrosion attacks during the anodic CPP measurement in 6 wt% FeCl₃. The average pit diameter on A-316L after anodic CPP in 6 wt% FeCl₃ and 5 wt% NaCl are of similar magnitude as presented in chapter 5.4.3 and Table 5.6, respectively. Since the depth is larger in 6 wt% FeCl₃ it implies that a more aggressive electrolyte affects the pit depth. However, small pits below 5 μm depth were not considered which causes the average depth to be smaller.

6.5.3 Pit propagation – general discussion

This section provides a general discussion of factors affecting propagation of a single pit at atmospheric conditions compared to the artificial pit experiment conducted in the experimental work. The purpose is to discuss the pit propagation in the artificial pit experiments and the effect of cathode area compared to what can be expected at normal operating condition in marine atmosphere.

The experimental parameters used in this thesis represents the worst-case scenario for pit propagation. In summary the artificial pit design, immersed conditions and the common electrolyte for both the anode and cathode causes a higher corrosion rate than what can be expected under normal operating conditions. Additionally, the 6Mo cathode causes a higher corrosion rate than what can be expected. Since the experiment was conducted immersed, factors that affect pit propagation under atmospheric conditions can cause the severity of the attacks to be lower. Probably the most important factor that affects pit propagation at atmospheric conditions compared to immersed conditions is ohmic drop in the electrolyte that constrains the available cathode area.

In terms of pit stability, the artificial pit design promotes the conditions necessary for maintaining the chemistry developing within the pit due to hydrolysis of metal cations. Pit propagation occurs below the coating when the pit radius approaches larger values than the radius of the drilled hole in the coating. Thus, an additional barrier for the diffusion path is provided which maintains the concentrated metal chloride solution inside the pit compared to open growing pits. This causes the measured galvanic current to be higher and thus the

corrosion rate. However, pits formed under operational conditions may attain different shapes such as undercutting or subsurface as presented in Fig. 2.2. In these cases, the artificial pit design may represent the high corrosion rates that can occur as the diffusion path is restricted compared to open propagating pits.

Wet dry cycles under atmospheric conditions compared to immersed conditions may affect the effective cathode area and repassivation of pits. The temperature normally falls at night which causes moisture to condense on the AISI 316L surface. As the temperature rises during the day water evaporation causes the cathode area to decrease and simultaneously increases the electrolyte conductivity. Thus, the cathode area is probably not constant during propagation of a single pit which can affect the corrosion rate. Furthermore, several cycles can cause chlorides to accumulate on the surface which promotes pitting corrosion initiation. On the contrary, if the dry cycle causes all the moisture to evaporate the propagating pit can repassivate.

Another important factor affecting pit propagation in the atmosphere compared to immersed conditions is the formation of corrosion products. Under atmospheric conditions corrosion products may be deposited at the attacked site as the corrosion process continues. This may decrease the electrolyte conductivity and thereby the effective cathode area. On the contrary, corrosion products can increase the electrolyte acidity since Fe is constrained from diffusing to the outer area of the pit. However, the long-term propagation depends on the composition of the corrosion products. The corrosion products may decrease the corrosion rate with time due to the protective ability as suggested by Lv et al[31]. Furthermore, deposits or containments on the surface can either accelerate or constrain the corrosion process. Deposits which adsorb water can cause a more severe attack due to creation of a continuous moist surface, while particles that prevent water from entering between the surface and the deposit can constrain the effective cathode area.

As can be seen from Fig. 2.5, the limited electrolyte during pitting corrosion at atmospheric conditions constrains mass transport to the lateral direction. This may promote pitting corrosion initiation in the adjacent area of the existing pit, which can cause several pits to propagate simultaneously. The density of pits that propagates simultaneously which share the effective cathode area may affect the attack severity regarding the depth. A higher pit density may cause less deep attack since ability of the cathode to consume electrons per pit decreases. In summary,

several factors as mentioned above can affect propagation of a single pit since the effective cathode area is affected.

The pit size and volume loss obtained in the artificial pit experiments are not realistic for AISI 316L under normal operating conditions. As discussed in the previous chapters, 6 wt% FeCl₃ causes the cathodic efficiency to be significantly higher than under normal operating conditions. Even though the low pH electrolyte simulates the chemistry developing within the pit, the cathode area used in the artificial pit experiments causes unrealistic corrosion rates. Furthermore, pits may reach a limited pit size at atmospheric conditions since the pit repassivates if the cathode area is polarised below E_{rep} [42]. However, the results from the artificial pit experiments demonstrates that the limited pit size may depend on the specific conditions the piping and equipment are subjected to due to the effect of cathode area and electrolyte chemistry.

7 Conclusion

In this study the effect of small changes in Mo content on the corrosion properties and propagation of a single pit were investigated.

From the anodic CPP curves at RT and $35 \pm 2^\circ\text{C}$ in both 3 and 5 wt% NaCl it can be concluded that the difference in alloying content affects E_{pit} , while E_{rep} is not significantly affected. The temperature appeared to influence E_{pit} more than the chloride concentration. According to the OCP measurements and salt spray exposure, the corrosion resistance for A-316L, B-316L and 316 Plus are not sufficient in 5 wt% NaCl at $35 \pm 2^\circ\text{C}$ when exposed to immersed conditions and simulated marine atmosphere.

Based on the anodic CPP curves, OCP measurements and salt spray exposure increased corrosion resistance due to Mo is noticeably for 317L. The difference in Mo content for A-316L, B-316L and 316 Plus does not significantly affect the corrosion properties since reduced Mo content is replaced by increased N content. Both Mo and N are important for the corrosion properties, and increased N content allows for the use of reduced Mo content without decreasing the corrosion resistance.

A method to study propagation of a single pit was developed and conducted. The pits connected to an external 6Mo cathode propagated continuously and did not reach a limited size due to repassivation since a galvanic current was measured for the entire test duration. Both the cathode area size and the electrolyte composition were discovered to be important for propagation of a single pit. The pit size increases with cathode area size in 6 wt% FeCl_3 , and the cathodic efficiency decreases significantly in 5 wt% NaCl compared to 6 wt% FeCl_3 . Based on this it may be concluded that further study on propagation of a single pit connected to a cathode with lower cathodic efficiency is necessary to determine the possibility of pits reaching a limiting pit size.

The main finding in this report is that small changes in Mo content for alloys containing below 2.5 wt% Mo does not reduce the corrosion properties when the alloy contains a sufficient amount of N.

8 Further work

To obtain more information on the effect of small changes in Mo content it is recommended to perform an XPS study to investigate if there is a difference in passive film composition among A-316L, B-316L, 317L and 316 Plus after exposure in a salt spray chamber.

To achieve a higher knowledge on propagation of a single pit the following is recommended for further work:

- To obtain information about the significance of variables that affects propagation of a single pit artificial pit experiments can be conducted at higher temperatures up to 35°C.
- Conduct the artificial pit experiment with two samples connected to the similar cathode areas as in this experiment, but with at an equal exposure time and immerse both samples in 5 wt% NaCl after the exposure in 6 wt% FeCl₃.
- Cathodic potentiodynamic polarisation of A-316L in 6 wt% FeCl₃ to obtain information of the cathodic polarisation behaviour of A-316L.
- Investigate propagation of a single pit where the cathodic efficiency is less.

Reference list

1. NORSOK Standard. *Materials selection*. M-001. 2014.
2. Kopluku, A., Mendez, C., *316 stainless steel instrument tubing in marine applications - Localized corrosion problems and solutions*, in *International Corrosion Conference Series* 2010.
3. McGuire, M.F., *Metallurgy*, in *Stainless Steels for Design Engineers*. 2008, ASM International Materials Park, Ohio 44073-0002. p. 1-10.
4. Olsson, C.O.A., Landolt, D., *Passive films on stainless steels—chemistry, structure and growth*. *Electrochimica Acta*, 2003. **48**(9): p. 1093-1104.
5. ASTM Standard. *Standard Specification for Seamless, Welded and Heavily Cold Worked Austenitic Stainless Steel Pipes*. A 312/A 312M. 2018.
6. Loable, C., Viçosa, I.N., Mesquita, T.J., Mantel, M., Nogueira, R.P. Berthomé, G., et al., *Synergy between molybdenum and nitrogen on the pitting corrosion and passive film resistance of austenitic stainless steels as a pH-dependent effect*. *Materials Chemistry and Physics*, 2017. **186**: p. 237-245.
7. Lambert, P., *Sustainability of metals and alloys 6 in construction*, in *Sustainability of Construction Materials*. 2016. p. 105-128.
8. McGuire, M.F., *Austenitic Stainless Steels*, in *Stainless Steels for Design Engineers*. 2008, ASM International Materials Park, Ohio 44073-0002. p. 69-90.
9. Clayton, C.R., Olefjord, I., *Passivity of Austenitic Stainless Steels*, in *Corrosion mechanisms in Theory and Practice*, P. Marcus, Editor. 2011, Taylor and Francis. p. 327-346.
10. McGuire, M.F., *Corrosion Types*, in *Stainless steels for design engineers*. 2008, ASM International Materials Park, Ohio 44073-0002. p. 27-56.
11. Degerbeck, J., *The influence of Mn compared to that of Cr, Mo and S on the resistance to initiation of pitting and crevice corrosion in austenitic stainless steels*. *Materials and Corrosion*, 1978. **29**(3): p. 179-188.
12. Xi, T., . Shahzad, M.B., Xu, D., Sun, Z., Zhao, J., Yang, C., et al. , *Effect of copper addition on mechanical properties, corrosion resistance and antibacterial property of 316L stainless steel*. *Materials Science & Engineering* 2017. **C 71**: p. 1079-1085.
13. Jiang, R., Wang, Y., Wen, X., Chen, C., Zhao, J., *Effect of time on the characteristics of passive film formed on stainless steel*. *Applied Surface Science* 2017. **412**: p. 214-222.
14. Jung, R.H., Tsuchiya, H., Fujimoto, S., *Growth Process of Passive Films on Austenitic Stainless Steels under Wet-dry Cyclic Condition*. *ISIJ International*, 2012. **52**(7): p. 1356-1361.
15. Bastidas, J.M., Torres, C. L., Cano, E., Polo, J. L., *Influence of molybdenum on passivation of polarised stainless steels in a chloride environment*. *Corrosion Science*, 2002. **44**(3): p. 625-633.
16. Frankel, G.S., *Pitting Corrosion, Corrosion: Fundamentals, Testing, and Protection*. *ASM Handbook* 2003. **13A**: p. 236-241.
17. Bhandari, J., Khan, F., Abbassi, R., Garaniya, V., Ojeda, R., *Modelling of pitting corrosion in marine and offshore steel structures – A technical review*. *Journal of Loss Prevention in the Process Industries*, 2015. **37**(C): p. 39-62.
18. Kelly, R.G., *Crevice Corrosion, Corrosion: Fundamentals, Testing, and Protection*. *ASM Handbook*, 2003. **13A**: p. 242-247.
19. Jakobsen, P.T., Maahn, E., *Temperature and potential dependence of crevice corrosion of AISI 316 stainless steel*. *Corrosion Science*, 2001. **43**(9): p. 1693-1709.

20. Laycock, N.J., Stewart, J. , Newman, R.C., *The initiation of crevice corrosion in stainless steels*. Corrosion Science, 1997. **39(10)**: p. 1791-1809.
21. Henderson, J.D., Ebrahimi, N., Dehnavi, V., Guo, M., Shoesmith, D. W., Noël, J. J., *The role of internal cathodic support during the crevice corrosion of Ni-Cr-Mo alloys*. Electrochimica Acta, 2018. **283**: p. 1600-1608.
22. Argarwal, A., Landau, U., Payer, J. H., Kelly, R. G., Cui, F., Presuel - Moreno, F. J., *Considerations of the Role of the Cathodic Region in Localized Corrosion*. International High Level Radioactive Waste Management Conference, Las Vegas, Nevada, 2006.
23. Bardal, E., *Korrosjon og korrosjonsvern*. 1994: Tapir akademiske forlag.
24. Galvele, J.R., *Tafels law in pitting corrosion and crevice corrosion susceptibility*. Corrosion Science, 2005. **47(12)**: p. 3053-3067.
25. Combrade, P., *Crevice Corrosion of Metallic Materials*, in *Corrosion mechanisms in Theory and Practice*, P. Marcus, Editor. 2011, Taylor and Francis. p. 450-495.
26. Kappes, M., Ortiz, M., Iannuzzi, M., Carranza, R., and M. Kappes, *Use of the Critical Acidification Model to Estimate Critical Localized Corrosion Potentials of Duplex Stainless Steels*. Corrosion (Houston), 2017. **73(1)**: p. 31-31.
27. Moayed, M.H., Newman, R. C., *Using pit solution chemistry for evaluation of metastable pitting stability of austenitic stainless steel*. Materials and Corrosion, 2005. **56(3)**: p. 166-173.
28. Schiroky, G., Dam, A., Okeremi, A., Speed, C., *Pitting and crevice corrosion of offshore stainless steel tubing*. Offshore (Tusla), 2013. **73(5)**: p. 122-124.
29. Zheng, S., Li, C., Qi, Y., Chen, L., Chen, C., *Mechanism of (Mg,Al,Ca)-oxide inclusion-induced pitting corrosion in 316L stainless steel exposed to sulphur environments containing chloride ion*. Corrosion Science, 2013. **67(C)**: p. 20-31.
30. Tsutsumi, Y., Nishikata, A., Tsuru, T., *Pitting corrosion mechanism of Type 304 stainless steel under a droplet of chloride solutions*. Corrosion Science, 2007. **49(3)**: p. 1394-1407.
31. Lv, W., Pan, C., Su, W., Wang, Z., Liu, S., Wang, C., *Atmospheric corrosion mechanism of 316 stainless steel in simulated marine atmosphere*. Corrosion Engineering, Science and Technology, 2016. **51(3)**: p. 155-162.
32. Pistorius, P.C., Burstein G.T., *Detailed Investigation of Current Transients from Metastable Pitting Events on Stainless Steel - The Transition to Stability*. Materials Science Forum, 1992. **111-112**: p. 429-452.
33. Vera Cruz, R.P., Nishikata, A., Tsuru, T., *Pitting corrosion mechanism of stainless steels under wet-dry exposure in chloride-containing environments*. Corrosion Science, 1998. **40(1)**: p. 125-139.
34. Ernst, P., Newman, R.C, *Pit growth studies in stainless steel foils. I. Introduction and pit growth kinetics*. Corrosion Science, 2002. **44(5)**: p. 927-941.
35. Alkire, R.C., Wong, K.P, *The corrosion of single pits on stainless steel in acidic chloride solution*. Corrosion Science, 1988. **28(4)**: p. 411-421.
36. Laycock, N.J., Newman, R. C., *Localised dissolution kinetics, salt films and pitting potentials*. Corrosion Science, 1997. **39(10)**: p. 1771-1790.
37. Strehblow, H.H., Marcus, P., *Mechanisms of Pitting Corrosion*, in *Corrosion Mechanisms in Theory and Practice*. 2011. p. 349-390.
38. Baboian, R., *Galvanic corrosion, Corrosion: Fundamentals, Testing, and Protection*. ASM Handbook, 2003. **13A**: p. 210-213.
39. Krouse, D., Laycock, N., Padovani, C., *Modelling pitting corrosion of stainless steel in atmospheric exposures to chloride containing environments*. Corrosion Engineering, Science and Technology, 2014. **49(6)**: p. 521-528.

40. Woldemedhin, M.T., Kelly, M.E., Shedd, R.G., *Evaluation of the maximum pit size model on stainless steels under thin film electrolyte conditions*. Journal of The Electrochemical Society, 2014. **161**(8): p. E3216-E3224.
41. Cui, F., Presuel-Moreno, F. J., Kelly, R. G., *Computational Modeling of the Stability of Crevice Corrosion of Wetted SS316L*. Electrochemical Transactions, 2006. **1**(16): p. 17-36.
42. Chen, Z.Y., Kelly, R.G., *Computational modeling of bounding conditions for Pit size on stainless steel in atmospheric environments*. Journal of the Electrochemical Society, 2010. **157** (2): p. C69-C78.
43. Heurtault, S., Robin, R., Rouillard, F., Vivier, V., *On the propagation of open and covered pit in 316L stainless steel*. Electrochimica Acta, 2016. **203**(C): p. 316-325.
44. Burstein, G.T., Pistorius, P. C., Mattin, S. P., *The nucleation and growth of corrosion pits on stainless steel*. Corrosion Science, 1993. **35**(1): p. 57-62.
45. Mankowski, J., Szklarska-Smialowska, Z., *Studies on accumulation of chloride ions in pits growing during anodic polarization*. Corrosion Science, 1975. **15**(6): p. 493-501.
46. Galvele, J.R., *Transport Processes and the Mechanism of Pitting of Metals*. Journal of the Electrochemical Society 1976. **123**: p. 464-474.
47. Srinivasan, J., Kelly, R. G., *One-dimensional pit experiments and modeling to determine critical factors for pit stability and repassivation*. Journal of the Electrochemical Society, 2016. **163**(13): p. C759-C767.
48. Keitelman, A., Alvarez, M.G., *40 Years of J.R. Galvele's Localized Acidification Pitting Model: Past, Present, and Future*. Corrosion, 2017. **73**(1): p. 8-17.
49. Agarwal, A.S., Landau, U., Payer, J. H., *Modeling the current distribution in thin electrolyte films with applications to crevice corrosion*. Journal of the Electrochemical Society, 2010. **157**(1): p. C9-C17.
50. Okeremi, A., Simon-Thomas, M., *External pitting and crevice corrosion of 316L stainless steel instrument tubing in marine environments and proposed solution*, in *International Corrosion Conference Series* 2008. p. 1-11.
51. Johansen, N.A., Presented by Fauske, T.H., *Korrosjon på AISI 316-rør Utfordringer og tiltak*. 2011, Statoil: NDT-konferansen. Bodø. Presentation.
52. ASTM Standard. *Standard Test Methods for Pitting and Crevice Corrosion Resistance of Stainless Steels and Related Alloys by Use of Ferric Chloride Solution*. G48-11. 2011.
53. ASTM Standard. *Standard Test Method for Electrochemical Critical Pitting Temperature Testing of Stainless Steels*. G150-99. 1999
54. Tomaselli, A.C., Valente, A., Camargo, F.C., *Super duplex SAF 2507 as alternative for standard 316L in hydraulic and instrumentation tubing on topside*, in *Offshore Technology Conference Brasil*. 2011: Rio de Janeiro. p. 1486-1495.
55. Mameng, S.H., R. Pettersson, and J.Y. Jonson, *Limiting conditions for pitting corrosion of stainless steel EN 1.4404 (316L) in terms of temperature, potential and chloride concentration: Limiting conditions for pitting corrosion of stainless steel*. 2017. p. 272-283.
56. Ramana, K.V.S., Anita, T., Mandal, S., Kaliappan, S., Shaikh, H., Sivaprasad, P. V. et al., *Effect of different environmental parameters on pitting behavior of AISI type 316L stainless steel: Experimental studies and neural network modeling*. Materials and Design, 2009. **30**(9): p. 3770-3775.
57. Man, H.C. and D.R. Gabe, *The study of pitting potentials for some austenitic stainless steels using a potentiodynamic technique*. Corrosion Science, 1981. **21**(9): p. 713-721.
58. Esmailzadeh, S., M. Aliofkhazraei, and H. Sarlak, *Interpretation of Cyclic Potentiodynamic Polarization Test Results for Study of Corrosion Behavior of Metals:*

- A Review. Protection of Metals and Physical Chemistry of Surfaces*, 2018. **54**(5): p. 976-989.
59. Malik, A.U., et al., *The influence of pH and chloride concentration on the corrosion behaviour of AISI 316L steel in aqueous solutions*. *Corrosion Science*, 1992. **33**(11): p. 1809-1827.
 60. Flis, J., *Corrosion of Metals and Hydrogen-Related Phenomena: Selected Topics*. Materials Science Monographs, 1991. **59**: p. 1-396.
 61. Park, J., Matsch, S., Bohni, H., *Effects of temperature and chloride concentration on pit initiation and early pit growth of stainless steel*. *J. Electrochem. Soc.*, 2002. **149**(2): p. B34-B39.
 62. ASTM Standard. *Standard Test Method for Conducting Cyclic Potentiodynamic Polarization Measurements for Localized Corrosion Susceptibility of Iron-, Nickel-, or Cobalt-Based Alloys*. G61-86. 1986.
 63. Silverman, D.C., *Tutorial on Cyclic Potentiodynamic Polarization Technique*, in *Corrosion 98*. 1998, NACE International: 22-27 March, San Diego, California. p. 299/1-299/21.
 64. Scully, J.R., Kelly, R.G., , *Methods for Determining Aqueous Corrosion Reaction Rates, Corrosion: Fundamentals, Testing, and Protection*. ASM Handbook, 2003. **13A**: p. 68-86.
 65. Iannuzzi, M., [Online]. *How to determine pitting and repassivation potentials*. 2014 [Accessed 28.02.19]; Available from: <https://www.aboutcorrosion.com/2014/04/13/howto-determine-pitting-and-repassivation-potentials/>.
 66. Klapper, H.S., Rebak, R.B., *Assessing the Pitting Corrosion Resistance of Oilfield Nickel Alloys at Elevated Temperatures by Electrochemical Methods*. *Corrosion*, 2017. **73**(6): p. 666-673.
 67. ISO standard. *BS EN ISO 21457:2010*. 2010.
 68. ASTM Standard. *Standard Guide for Examination and Evaluation of Pitting Corrosion*. G46 - 94. 1994 (Reapproved 2018).
 69. Maurice, V., Peng, H., Klein, L.H., Seyeux, A., Zanna, S., Marcus, P., *Effects of molybdenum on the composition and nanoscale morphology of passivated austenitic stainless steel surfaces*. *Faraday Discussions*, 2015. **180**: p. 151-170.
 70. Upadhyay, N., Pujar, M. G., Singh, S. S., Krishna, N.G., Mallika, C., Mudali, U. K., *Evaluation of the Effect of Molybdenum on the Pitting Corrosion Behavior of Austenitic Stainless Steels Using Electrochemical Noise Technique*. *Corrosion*, 2017. **73**(11): p. 1320-1334.
 71. Sugimoto, K. and Y. Sawada, *The role of molybdenum additions to austenitic stainless steels in the inhibition of pitting in acid chloride solutions*. *Corrosion Science*, 1977. **17**(5): p. 425-445.
 72. Ilevbare, G.O., Burstein, G.T., *The role of alloyed molybdenum in the inhibition of pitting corrosion in stainless steels*. *Corrosion Science*, 2001. **43**(3): p. 485-513.
 73. Newman, R.C., *The dissolution and passivation kinetics of stainless alloys containing molybdenum—I. Coulometric studies of Fe-Cr and Fe-Cr-Mo alloys*. *Corrosion Science*, 1985. **25**(5): p. 331-339.
 74. ASTM Standard. *Standard Practice for Cyclic Salt Fog/UV Exposure of Painted Metal, (Alternating Exposures in a Fog/Dry Cabinet and a UV/Condensation Cabinet)*. D5894-96 1996.
 75. Liptáková, T., Zatkalíková, V., *The variability of chemical composition of the AISI 316 Ti and pitting*. *Trans. FAMENA*, 2009. **33**(1): p. 31-36.

76. Kamachi Mudali, U., Dayal, R., *Influence of nitrogen addition on the crevice corrosion resistance of nitrogen-bearing austenitic stainless steels*. Journal of Materials Science, 2000. **35**(7): p. 1799-1893.
77. Newman, R.C. and T. Shahrabi, *The effect of alloyed nitrogen or dissolved nitrate ions on the anodic behaviour of austenitic stainless steel in hydrochloric acid*. Corrosion Science, 1987. **27**(8): p. 827-838.
78. Heurtault, S., Robin, R., Rouillard, F., Vivier, V., *Initiation and propagation of a single pit on stainless steel using a local probe technique*. Faraday Discussions, 2015. **180**: p. 267-282.
79. Aouina, N., Balbaud-Célérier, F., Huet, F., Joiret, S., Perrot, H., Rouillard, F., et al., *A flow microdevice for studying the initiation and propagation of a single pit*. Corrosion Science, 2012. **62**: p. 1-4.
80. ASTM Standard, *Standard Practice for Operating Salt Spray (Fog) Apparatus*. B117-11, 2011.
81. Jotun. *Technical Data Sheet Jotamastic 87*. [Online] [Accessed 2019-06-03]; Available from: https://www.jotun.com/Datasheets/Download?url=%2fTDS%2fTDS_515_Jotamastic+87_Euk_GB.pdf.
82. Alicona. [Online] [Accessed 2019-04-25]; Available from: <https://www.alicon.com/en/products/infinitefocus/>.
83. Microsoft. *Create a box and whisker chart*. [Online] [Accessed 2019-06.03]; Available from: <https://support.office.com/en-us/article/create-a-box-and-whisker-chart-62f4219f-db4b-4754-aca8-4743f6190f0d>.

Appendix A

The chemical composition (wt%) for selected alloys from chapter 3.2.

Table A1

Steel grade	C	Mn	P	S	Si	Cr	Ni	Mo	Other
316L	0.014	1.57	0.024	0.006	0.35	16.8	12.16	2.00	
317LMN	0.017	1.41	0.013	<0.001	0.072	19.44	13.57	4.25	N:0.13 Cu:0.082

Table A2

AISI designation	C	Mn	P	S	Si	Cr	Ni	Mo	Other
304LN	0.012	1.06	0.012	0.001	0.09	18.07	11.3	0.02	N: 0.13
316LN	0.025	1.1	0.017	0.0041	-	17.5	11.5	2.53	N:0.14
317LN	0.014	1.09	0.032	0.001	0.69	18.41	11.2	3.58	N:0.141

Table A3

AISI designation	C	Mn	P	S	Si	Cr	Ni	Mo	Other
316Ti A1	0.04	1.69	0.026	0.002	0.43	16.5	10.6	2.12	N:0.012 Ti:0.41
316Ti A2	0.07	1.35	0.03	0.029	0.45	16.59	11.8	2.04	N:0.007 Ti:0.51
316Ti A3	0.08	0.662	0.027	0.051	0.671	16.75	11.75	2.23	Ti:0.47
316Ti A4	0.045	0.66	0.027	0.010	0.65	16.5	13.06	2.88	N:0.015 Ti:0.24
316Ti A5	0.05	0.66	0.026	0.052	0.67	16.27	13.18	2.82	Ti:0.27

Table A4

Material Type	C	Mn	P	S	Si	Cr	Ni	Mo	Other
304 SS	0.043	1.68	0.026	0.014	0.31	18.39	9.7	0.03	N:0.086
316 SS	0.049	1.69	0.025	0.006	0.64	16.46	12.4	2.28	N:0.053
316 SS	0.025	1.76	0.026	0.002	0.98	17.90	12.1	2.45	N:0.068
316 SS	0.021	1.60	0.021	0.003	0.84	17.40	13.2	2.57	N:0.160
317 SS	0.022	1.82	0.025	0.002	0.30	18.22	14.2	3.04	N:0.088
317 SS	0.014	1.09	0.032	0.001	0.69	18.47	13.2	3.58	N:0.141

Table A5

Laboratory grade	C	Mn	P	S	Si	Cr	Ni	Mo	Other
18Cr-12Ni	0.025	1.012	-	13	0.594	17.999	12.067	0.004	Al: 0.0033 N: 0.023
18Cr-12Ni-0.1N	0.025	1.074	-	11	0.502	18.06	11.77	0.007	Al:0.001 N:0.115
18Cr-12Ni-3Mo	0.028	1.018	-	15	0.571	18.003	11.995	2.989	Al: 0.0036 N:0.029
18Cr-12Ni-3Mo-0.1N	0.025	1.011	-	17	0.510	17.88	12.09	2.952	Al:0.001 N:0.107

Appendix B

Material certificate UNS S31600/S31603

 ATI Flat Rolled Products 500 Green Street Washington, PA 15301	Certificate of Test		 <small>Version Defunct - No. Message, Quality</small>
	Mill Information Cert Number 0186184-00		Customer Information Name PO PO Date

Sold to:	Ship to:
----------	----------

Material Information

"ATI 316/316L" STAINLESS STEEL PMP HOT ROLLED PLATE ANNEALED PICKLED COMMERCIAL CUT EDGE	
SS SPEC REV 11 - 316/316L DIN EN 10204:2005 3.1 CERTIFICATE AMS 5507G ASTM-A-262-15 PRACTICE E NACE MR0103/ISO 17495-1:2016 ASME-SA-240 ED 2017 UNS S31603 S-400 DTD 06/03/2016	QQ-S-7660 AMS 5524L R2014 NACE MR0175/ISO 15156-3:2015 ASTM-A-480-18 ASTM-A-240-17 UNS S31600 08/30/18 EXCEPTIONS TO SS SPEC

Piece Information

Pcs	Gauge (in)	Width (in)	Length (in)	Heat #	Piece ID	Section Id	Lot #	Total Wt (lbs)
1	.3750	72.0000	303.0000	855303	CE90278	---	480690	2499

Chemistry Testing

Element (wt %)	Requirements		Final Heat Analysis	
	Min	Max	855303	Loc
C	---	.030	.022	BN
MN	---	2.00	1.42	BN
P	---	.040	.031	BN
S	---	.030	< .001	BN
SI	---	.75	.32	BN
CR	16.00	18.00	16.25	BN
NI	10.00	14.00	10.11	BN
MO	2.00	3.00	2.03	BN
CU	---	.75	.40	BN
N	---	.10	.07	BN
CO	---	---	.38	BN

 ATI Flat Rolled Products 500 Green Street Washington, PA 15301	Certificate of Test		 <small>Vicenzo DiTorrain - Sr. Manager, Quality</small>
	Mill Information Cert Number 0186184-00 Sales Order Cert Date		Customer Information Name PO PO Date

Chemistry Testing

Element (wt %)	Requirements		Final Heat Analysis	
	Min	Max	855303	Loc
ATI Flat Rolled Products performs chemical analysis by following techniques for testing locations TC, BM, & LG: C, S by combustion/infrared; N, O, H by inert fusion/thermal conductivity; Mn, P, Si, Cr, Ni, Mo, Cu, Pb, Co, V, by WDCRF; Fe, Bi, Ag by GPAA; B by OES; Al and Ti (>=0.10%) by WDCRF, otherwise by OES. 855303 - Material was produced by EP melting with AOD refining. USA melt and manufacture				

Mechanical Testing

		LOT 480690	
Condition:		ANNEALED	
Direction:		TRANSVERSE	
Temperature:		ROOM TEMP	
Spec:			
Test Limit	Units	Result	Loc
YS 0.2% OFFSET	psi	38700.	TC
TENSILE	psi	83000.	TC
ELONG. IN 2"	%	74.	TC
RED OF AREA	%	81.	TC
HARDNESS	--	144. HBW	TC
When hardness is measured using the Brinell scale, the indentation measuring device is Type A. Bend test passed per periodic test requirement.			

Mechanical Property Requirements

Condition:		ANNEALED	
Direction:		TRANSVERSE	
Temperature:		ROOM TEMP	
Spec:			
Test Limit	Units	Min	Max
YS 0.2% OFFSET	psi	30000.	---
TENSILE	psi	75000.	100000.

	Certificate of Test		 <small>Process Specialist - Sp. Nonspc. Quality</small>
	Mill Information		Customer Information
500 Green Street Washington, PA 15301	Cert Number 0186184-00 Sales Order Cert Date	Name PO PO Date	

Mechanical Property Requirements

Condition:	ANNEALED		
Direction:	TRANSVERSE		
Temperature:	ROOM TEMP		
Spec:			
Test Limit	Units	Min	Max
ELONG. IN 2"	%	45.	---
RED OF AREA	%	---	---
HARDNESS	---	---	217. HRW

Corrosion Testing

Test ID	Result Name	Test Result	Wt Loss	Units	Visual Exam	Pit Depth	Units	Bend	Loc	Requirements
LOT 480690	A-262 E/SCR A	STEP	---	---	---	---	---	---	TC	---

The material was successfully corrosion tested to procedures listed in ASTM A 262 Practice A for the unsensitized condition. Material supplied in the unsensitized condition.

Certification Statements

Grade verification was performed spectroscopically.

Material was solution annealed at 1900F (1038C) minimum for a time commensurate with thickness and rapidly cooled with air or water.

ATI Flat rolled Products does not use mercury in the testing or production of its products.

No welds/weld repairs performed.

DIN EN 10204:2005 - ATI Flat Rolled Products is approved as a manufacturer according to Pressure Equipment Directive PED 2014/68/EU.

ATI Flat Rolled Products has an active radioactive testing program which monitors the incoming raw materials as well as melt samples for evidence of radioactivity. Raw material or melt showing radiation levels above normal background are not permitted to be used.

Quality system certified according to Pressure Equipment Directive 2014/68/EU, Annex I, Paragraph 4.3 by TÜV SÜD, Industrie Service GmbH, (Notified Body 0036)

Material tested at ATI Flat rolled Products GEAE S400 approved facilities (T1225 & T9317): Katrona Heights, PA; Brackenridge, PA and New Bedford, MA.

Material supplied in accordance with ISO 9001:2008 and AS9100C, certificate number 11098.

ATI Flat Rolled Products holds several Quality and Laboratory Certifications that include ISO-9001, AS9100, AD 2000-Merkblatt W0, EU Pressure Equipment Directive 14/68/EU, Nadcap, ISO/IEC 17025, GEAE S400 (T1225 & T9317), GEAE S-1000. Refer to www.ATIMetals.com to access the current ATI-FRP quality certifications

EN 10204:2005 3.1 certificate.

 ATI Flat Rolled Products	Certificate of Test		 <small>V. B. Bortone</small> <small>Process Specialist - St. Joseph, Quality</small>
	Mill Information Cert Number 0186184-00		Customer Information Name PO PO Date
500 Green Street Washington, PA 15301			

General Statements

The Finishing Location for ALL PIECES is ATI-FRP
 The shipping Location is ATI-FRP WASHINGTON, PA

TESTING WAS PERFORMED AT THE FOLLOWING LOCATIONS
 BN = ATI FLAT ROLLED PRODUCTS; 100 River Road; Brackenridge, PA 15014
 TC = ATI FLAT ROLLED PRODUCTS; 1300 Pacific Avenue; Natrona Heights, PA 15065

Knowingly and willfully recording any false, fictitious or fraudulent statement or entry on this document may be punished as a felony under Federal Statutes, including Federal Law, Title 18, Chapter 47.

WARNING: Processing that makes fumes, dust, or solutions may cause lung disease. Please see Safety Data sheet for further information which has been supplied to your Purchasing Department. For an additional copy, please refer to our website at:
www.atimetals.com/Products/ati-sds

For access to online certifications of test, please register at MYATI.ATIMETALS.COM

This Certified Material Test Report is a true representation of the data on file. The reported results conform to the sales contract and specification(s) as set forth in ATI Flat Rolled Products order acknowledgement. This certificate of test may not be reproduced except in full without the written authorization of the company.

ATI Flat Rolled Products website contains listing of material produced, general technical and contact information, and current quality and company accreditations including but not limited to ISO-9001, AS-9100, Nadcap, and ISO/IEC 17025. Please visit us at www.atimetals.com

Material certificate UNS S31700/S31703

	Certificate of Test		 <small>Vincenzo DeFerrari - Sr. Manager, Quality</small>
	Mill Information		Customer Information
500 Green Street Washington, PA 15301	Cert Number: 0185710-00 Sales Order: Cert Date:	Name: PO: PO Date:	

Sold to:	Ship to:
----------	----------

Material Information

"ATI 317/317L" STAINLESS STEEL	
PMP HOT ROLLED PLATE ANNEALED PICKLED COMMERCIAL CUT EDGE	
ASTM-A-240-17	ASME-SA-240 ED 2017
UNS S31700	UNS S31703

Piece Information

Pos	Gauge (in)	Width (in)	Length (in)	Heat #	Piece ID	Section id	Lot #	Total Wt (lbs)
Item: 001	Cust-Id:		Govt-Contract-#:		Govt-DO-Rating:			
	Cust-Job:		ScheduleB:					
1	.5000	96.0000	275.0000	856026	CE90000	---	480761	3972

Chemistry Testing

Element (wt %)	Requirements		Final Heat Analysis	
	Min	Max	856026	Loc
C	---	.030	.016	BN
MN	---	2.00	1.60	BN
P	---	.045	.026	BN
S	---	.030	< .001	BN
SI	---	.75	.32	BN
CR	18.00	20.00	18.39	BN
NI	11.00	15.00	14.11	BN
MO	3.00	4.00	3.06	BN
N	---	.10	.06	BN

ATI Flat Rolled Products performs chemical analysis by following techniques for testing locations TC, BN, & LO:
 C, S by combustion/infrared; N, O, H by inert fusion/thermal conductivity;
 Mn, P, Si, Cr, Ni, Mo, Cu, Cb, Co, V, by WDXRF; Pb, Bi, Ag by GFAAR
 B by OES; Al and Ti (>=0.10%) by WDXRF, otherwise by OES.

856026 - Material was produced by EF melting with AOD refining.
 DSA melt and manufacture

 500 Green Street Washington, PA 15301	Certificate of Test		 <small>Proven Performance - Superior Quality</small>
	Mill Information Cert Number 0185710-00		Customer Information Name PO PO Date

Mechanical Testing

		LOT 480761	
Condition:	ANNEALED		
Direction:	TRANSVERSE		
Temperature:	ROOM TEMP		
Spec:			
Test Limit	Units	Result	Loc
YS 0.2% OFFSET	psi	41500.	TC
TENSILE	psi	81800.	TC
ELONG. IN 2"	%	54.	TC
RED OF AREA	%	72.	TC
HARDNESS	---	154.	HRB TC

When hardness is measured using the Brinell scale, the indentation measuring device is Type A.

Mechanical Property Requirements

Condition:	ANNEALED		
Direction:	TRANSVERSE		
Temperature:	ROOM TEMP		
Spec:			
Test Limit	Units	Min	Max
YS 0.2% OFFSET	psi	30000.	---
TENSILE	psi	75000.	---
ELONG. IN 2"	%	40.	---
RED OF AREA	%	---	---
HARDNESS	---	---	217. HRB

Corrosion Testing

Test ID	Result Name	Test Result	Wt Loss	Units	Visual Exam	Pit Depth	Units	Bend	Loc	Requirements
LOT 480761	A-262 E/SCR A	STEP	---	---	---	---	---	---	TC	---

	Certificate of Test		 <small>Witness Defect-Free - Ex. Superior Quality</small>
	Mill Information		Customer Information
500 Green Street Washington, PA 15301	Cert Number 0185710-00 Sales Order Cert Date	Name PO PO Date	

Certification Statements

Grade verification was performed spectroscopically.

EN 10204:2005 - 3.1 certificate does not imply that material is an approved PED grade. For a complete listing of approved PED grades, visit our website at www.atimetals.com.

Material was solution annealed at 1900F (1038C) minimum for a time commensurate with thickness and rapidly cooled with air or water.

ATI Flat Rolled Products does not use mercury in the testing or production of its products.

No welds/weld repairs performed.

EN 10204:2005 3.1 Certificate.

General Statements

The finishing location for ALL PIECES is ATI-FRP
 the shipping location is ATI-FRP WASHINGTON, PA

TESTING WAS PERFORMED AT THE FOLLOWING LOCATIONS
 BN - ATI FLAT ROLLED PRODUCTS; 100 River Road; Brackenridge, PA 15014
 TC - ATI FLAT ROLLED PRODUCTS; 1300 Pacific Avenue; Natrona Heights, PA 15065

Knowingly and willfully recording any false, fictitious or fraudulent statement or entry on this document may be punished as a felony under Federal Statutes, including Federal Law, Title 18, Chapter 47.

WARNING: Processing that makes fumes, dust, or solutions may cause lung disease. Please see safety data sheet for further information which has been supplied to your Purchasing Department. For an additional copy, please refer to our website at:
www.atimetals.com/Products/at1-sds

For access to online Certifications of Test, please register at MyATI.ATIMetals.com

This Certified Material Test Report is a true representation of the data on file. The reported results conform to the sales contract and specification(s) as set forth in ATI Flat Rolled Products order acknowledgement. This Certificate of Test may not be reproduced except in full without the written authorization of the company.

ATI Flat Rolled Products website contains listing of material produced, general technical and contact information, and current quality and company accreditations including but not limited to ISO-9001, AS-9100, Nadcap, and ISO/IEC 17025. Please visit us at www.atimetals.com

Material certificate UNS S31655



INSPECTION CERTIFICATE 3.1
EN 10204 3.1

Certificate No. / Zeugnis Nr. / N° du certificat / Page 785106/003 1 (01)
Date / Datum / Date 16.08.2017

Delivery address, Empfänger, Lieu de livraison OUTOKUMPU NIROSTA GMBH (BST. TEILBUCHHALTUNG (NIROSTA)) OBERSCHLESSENSTR. 16 47807 KREFELD BR DEUTSCHLAND		OUTOKUMPU NIROSTA GMBH (BST. TEILBUCHHALTUNG (NIROSTA)) OBERSCHLESSENSTR. 16 47807 KREFELD BR DEUTSCHLAND										
Requirements, Anforderungen, Exigences ASTM A240/A240M		Our Order No. Linear Auftrag Nr. N° de commande n° 300443815	Your order, Ihre Bestellung, Votre commande OSW / CHRISTOPHER KASCHUBA									
Product, Erzeugnisform, Produit SHEET, STAINLESS STEEL		Mark of Manufacturer Zeichen des Lieferanten Signe de producteur outokumpu	Process Erzeugnisart Mode de fabrication AOD									
Grade, Werkstoff, Nuance UNS S31655		Tolerances Tolerances, Tolérances ASTM A 480										
Marking, Kennzeichnung, Marquage A240 S31655 2B		Marks, Versandbezeichnungen, Marques										
Line Reihe Ligne	Item Position Poste	Charge-test No. Schweiß-Prübe Nr. Coulée n°	Size, Abmessungen, Dimensions	Quantity Stückzahl Nombre	Weight, Gewicht, Poids	Final Ausführung Fin EN/ASTM						
1	6	42073 4	3,0 X 1250 X 2500 MM	12	894 KG	2B						
2	8	53751 1	4,0 X 1500 X 3000 MM	7	1000 KG	2B						
Charge no. Schweiß Nr. Coulée n°	Chemical composition, Chemische Zusammensetzung, Composition chimique											
	C %	Si %	Mn %	P %	S %	Cr %	Ni %	MO %	N %	CU %		
42073	0,020	0,34	1,78	0,027	0,001	20,4	8,4	0,56	0,176	0,29		
53751	0,025	0,36	1,70	0,026	<.001	20,3	8,5	0,59	0,202	0,33		
Line Reihe Ligne	Mechanical properties, Mechanische Eigenschaften, Caractéristiques mécaniques							Tensile test, Zugversuch, Essai de traction				
	Sample ID Proben ID Échantillon	Rp0.2 MPa	Rp1.0 MPa	Rm MPa	A5 %	A50 %		Hardness Härte-Durometer HBW	ISO 6892-1:2009 A224 SAMPLES PERPENDICULAR TO THE ROLLING DIRECTION			
1	01	400	438	720	44	40		200	TENSILE TEST AT ROOM TEMPERATURE IN DELIVERY CONDITION RP0.2 PROOF STRENGTH RP1.0 PROOF STRENGTH RM TENSILE STRENGTH A50 ELONGATION GL 50 MM A5 ELONGATION PROPORTION HBW BRINELL HARDNESS HV10 VICKERS HARDNESS			
	02	403	434	721	45	41		200				
2	01							207				
	02	386	412	703	46	43		199				
Identify test, Verwechslungsprüfung, Contrôle d'identification Size, Abmessungen, Dimensions Surface, Oberfläche, Surface Test of integrity, corros, Prüfung auf Integrität, Korros, Test de coros, Intégrité. ASTM A262 PRACTICE E : OK												
								We certify that the above mentioned products comply with the terms of the order contract. Wir bestätigen, dass die Lieferung den Vereinbarungen der Bestellung entspricht. Nous certifions que les produits énumérés ci-dessus sont conformes aux prescriptions de la commande.				
								This test certificate is made by controlled ADP-system and is valid without signature. Dieses Zeugnis wurde von einem überprüften Datenverarbeitungssystem erstellt und ist ohne Unterschrift gültig. Ce certificat a été établi par un système informatique contrôlé et est valide sans signature.				
								Outokumpu Stainless Oy Authorized Inspector / Werkstoffverantwortlicher / Inspecteur autorisé LARI NISSINEN FI-66490 Tornio, Finland Tel. +358 16 4521, email certificate.tornio@outokumpu.com, www.outokumpu.com Domsic: Tornio, Finland, Business Identity Code 062315-9				

Chemical composition UNS S31603

Specification	Test number	Min	% C	% Si	% Mn	% Ni	% CR	% MO	% S	%		
38	9LCG	Max	0,0300	1,0000	2,0000	12,5000	17,0000	2,5000	0,0050	0,0450		
39A		coulé/Schmelzen / Heat	0,0210	0,5360	1,5730	12,7440	17,3220	2,5480	0,0085	0,0304		
		Produit / Erzeugnisform / Product										
Vorschrift / Required	50	51	52	53	54	55	70	71	72	73	74	75
	% N	% Ti										
Min												
Max	0,1000											
Schmelzen / Heat	0,0340	0,0050										
Erzeugnisform / Product												

1.4435 ch 506513

Material certificate UNS S31254



CERTIFICATE - ZEUGNIS - CERTIFICAT

EN 10204-3.1
2453701-EN

Invoice No.
Rechnung Nr.
N° de facture
6610/1000556811

Page
Seite
Page
1/1

Business Unit / OOM
Avesta Works / Johan Nordström

Date / Datum / Date
08-Aug-2017

Load, Ladung, Charge No
SE/150727

Acknowledged ID, Bestätigung, Commande ID
6610/300430287

Your ref., Ihre Ref., Voss ref. test samples		Requirements, Anforderungen, Exigences ASTM A 240M-16a ASME BPVC BEC II PART A SA-240/SA-240M 2015 EN 10088-2:2014 EN 10028-7:2016 EN ISO 9444-2 / ASTM A480M	
Buyer, Besteller, Acheteur Outokumpu Nirosta GmbH Oberschliesenstr. 16 DE 47807, Krefeld GERMANY			
Consignee, Empfänger, Lieu de livraison Outokumpu Stainless AB			
Melt of Manufacturer Zeichen des Lieferwerkes Signe de producteur 	Process Erzschmelzungsart Mode de fusion E+AOD	Inspector's stamp Zeichen des Sachverständigen Polcon de l'expert 	Grade, Werkstoff, Nuance Outokumpu Ultra 254 SMO UNS S31254 1.4547

Product, Erzeugnisform, Produit
Stainless Steel Hot Rolled, Coil-Plate
finish 1D, cut edge

Line Reihe Ligne	Item Position Poste	Heat/Lot No Schmelz-Lot Nr Coulée n° - Lot No	Size Abmessungen Dimensions	Pieces Stückzahl Nombre	Quantity / Unit Menge / Einheit Quantité / Unité
1	6	565198-004	6,00 x 1500 x 3000 mm	1	216 kg

Chemical composition — Chemische Zusammensetzung — Composition chimique

	C	Si	Mn	P	S	Cr	Ni	Mo	Nb	Cu	Co	W
Heat	.012	.40	.45	.021	.001	20.17	17.92	6.04	.008	.73	.300	.210

Radioactive contamination check acc. IAEA recommendations: Approved

Test results — Prüfergebnisse — Résultats des essais (1N/mm² = 1 MPa) F = Front — Arête — Début B = Back — Ende — Fin T = Transverse — Quer — Travers

Test Ref	Temp °C	RP 0.2 R/30x2	RP 1.0 R/30x2	RM R/30x2	A5 %	2" %	SB
Min	+20	320	350	655	35	35	SB
Max				850			223
	+20	400	455	754	46	46	192
		400	453	754	47	47	192

Corrosion acc. EN ISO 3651-2C: Approved
Heat treatment / Solution annealed: Material temp minimum 1150 °C / Quenched (forced air + water)
Steel grade verification (PMT-spectroscopic): Approved
Marking, visual insp. and gauge measurement: Approved
Certified acc. Pressure Equipment Directive (2014/68/EU) by TÜV CERT-Certification body
for pressure equipment of the TÜV NORD Systems; notified body, reg-no. 0045.

